LINEAR PERMANENT MAGNET MACHINES FOR OIL PUMPING SYSTEMS

A Dissertation

by

HUSSAIN A. I. A. HUSSAIN

Submitted to the Office of Graduate and Professional Studies of
Texas A&M University
in partial fulfillment of the requirements for the degree of

DOCTOR OF PHILOSOPHY

Chair of Committee,	Hamid A. Toliyat
Committee Members,	Mehrdad Ehsani
	Shankar P. Bhattacharyya
	Alan Palazzolo
Head of Department,	Miroslav M. Begovic

May 2017

Major Subject: Electrical Engineering

ABSTRACT

Sucker rod pumping systems are the dominant technology used currently in oil pumping systems for stripper (marginal) wells. The system consists of a high-speed rotating prime mover, a linear reciprocating pump, a gear reducer and a crank and beam mechanism to translate the high-speed rotating motion into a low-speed linear motion.

A sucker rod pumping system requires a relatively large surface area which limits its use in offshore applications. Moreover, the sucker rod pumping system cannot be used in deviated wells because of the long steel sucker rod.

In this research, the replacement of the sucker rod pumping system with a permanent magnet linear motor which drives the reciprocating pump directly is presented. In this system, the motor drive is placed on the surface and connected to the motor through a long cable. The motor is placed downhole to drive the reciprocating pump. The main challenges of this system result from the high temperature downhole and the long transmission cable and will be discussed in detail.

Another system which replaces the AC cable with a DC cable is proposed. In this system, the inverter is integrated with the motor downhole while the rectifier remains on the surface. A modified integrated motor drive with a speed control algorithm is proposed. Moreover, two sensorless algorithms are developed; one for the AC system and one for the DC system. The DC system algorithm estimates the motor position based on the motor model using the current and voltage measurements. The AC system sensorless algorithm utilizes both the motor and cable models to estimate the motor position and motor current.

Finally, a pump monitoring system is developed to detect the common pump faults. An observer is developed to estimate the load force from the motor current and speed. The load force could be used along the motor position to identify various fault signatures.

DEDICATION

To my family and friends.

ACKNOWLEDGEMENTS

CONTRIBUTORS AND FUNDING SOURCES

NOMENCLATURE

CHP   Combined Heat and Power

PCP   Progressive Cavity Pump

ESP   Electric Submersible Pump

VSC   Variable Speed Controller

PM   Permanent Magnet

DTC   Direct Torque Control

FOC   Field Oriented Control

AC   Alternating Current

DC   Direct Current

POC   Pump-Off Controllers

BPD   Barrels per day

SPM   Strokes per minute

PRL   Polished Rod Load

HP   Horse Power

PRHP   Polish Rod Horse Power

BPDA   Biphenyl-tetracarboxylic acid dianhydride

IGBT   Insulated-Gate Bipolar Transistor

MOSFET   Metal-Oxide Semiconductor Field-Effect Transistor

ADC   Analog to Digital Converter

PLL   Phase Locked Loop

EMF	Electromotive Force
PI	Proportional-Integral
TROMAG	Trans-Rotary Magnetic Gear
IDM	Integrated-Drive Motor
PMSM	Permanent Magnet Synchronous Motor
PFC	Power Factor Correction
PWM	Pulse Width Modulation
FEA	Finite Element Analysis
KVL	Kirchhoff's Voltage Law
KCL	Kirchhoff's Current Law

TABLE OF CONTENTS

LIST OF FIGURES

LIST OF TABLES

CHAPTER I

INTRODUCTION

Despite the rapid developments achieved in renewable energy sources, crude oil (petroleum) remains the dominant source of energy in today's human life. Figure 1 shows the energy consumption by energy source in the United States [1]. This situation is expected to remain unchanged for the next few decades. Despite its environmental impact, crude oil is still the most affordable source of energy in many places worldwide. It is refined to be used as a fuel in transportation, a fuel in the industrial combined heat and power (CHP) generation, and in making of several petrochemical products such as industrial chemicals, plastics, synthetic dyes and many other derivatives.
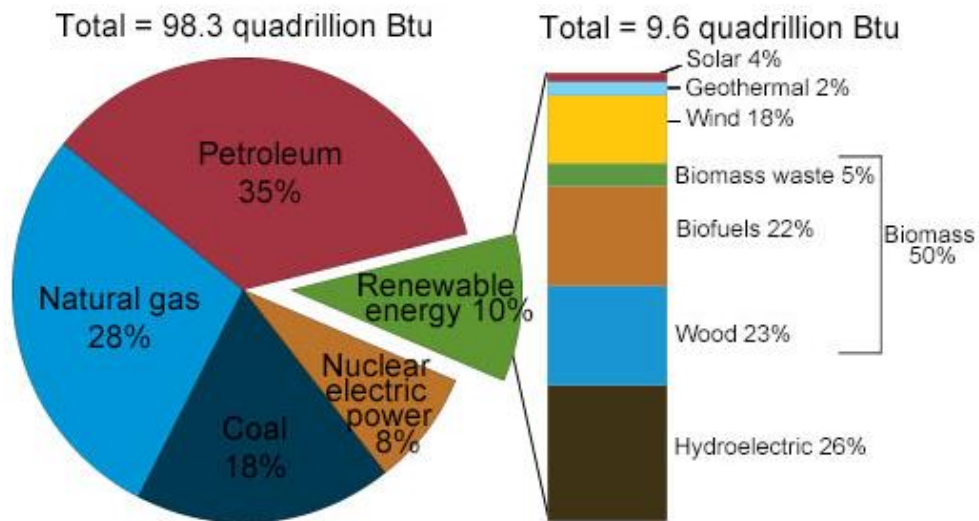
Figure 1 : United States energy consumption by energy source, 2014 [1].

The first step in oil production is to locate the oil reservoir. Geologists usually conduct seismic surveys to explore the areas of potential oil reservoirs. The collected data from these surveys is processed and interpreted to create maps which locate the most efficient and safest drilling locations. The depth of these oil reservoirs could vary from around 1,000 feet to more than 40,000 feet. The average well depth in the United States is around 5,000 feet.

Next, a drill bit which is driven by an oil rig is used to create a small-diameter deep hole known as the wellbore. The hole extended from the earth surface to the oil reservoir. A drilling fluid is used to help removing the cuttings and stabilizing the well. The wellbore is secured by a steel casing to protect the well from outside contamination and to prevent it from caving in. The casing is then cemented to stop fluid movement between formations. Finally, an assembly of valves and gauges known as the Christmas tree is placed on the surface to regulate the flow.

Once the drilling is done and the oil well is secured, the well is ready for the production stage.

1.1 Oil pumping systems

In most oil wells, the oil in the reservoir flows naturally to the surface because of the sufficient formation pressure. Initially, this pressure is high enough to start the production at acceptable rates. As production continues, the oil pressure starts to drop which results in a declined production rate. Secondary recovery methods are eventually used as the pressure declines during production to a point where it no longer economically

feasible to continue the production. The two main secondary recovery methods widely used today are:

A. Gas or water injection (flooding):

Fluid injection into the reservoir can increase the pressure which help the oil flow to the surface. The injection is usually done using CO_2 or water and it may be either continuous or intermittent.

B. Artificial lift:

Various pumping systems could be utilized including:

1) Progressive cavity pump (PCP): Also known as eccentric screw pump. It is driven by a rotating prime mover and usually has a high efficiency.

2) Jet pump: It operates based on Venturi effect. Although, it has no moving parts, it usually results in low efficiency.

3) Electric submersible pump (ESP): Consists of a multistage rotating centrifugal pump. It offers a high production rate at a high initial cost.

4) Sucker rod pump: Also known as pump jack or beam pump. It is commonly used for stripper (marginal) oil wells which require lower production rates. Figure 2 shows a sucker rod pump which consists of: prime mover, gear reducer, crank and beam, sucker rod and a downhole reciprocating pump.

Figure 2 : A sucker rod pumping system.

Electric Submersible Pumps (ESP) and sucker rod pumps are the main technologies in today's artificial lift market. ESP have been used in artificial lift applications for the last few decades [2]. They dominate the market in oil wells that require high production rates. Commonly used ESPs consist of a : variable speed controller (VSC) [3]-[4], long transmission cable, three-phase rotating induction motor, a submersible

centrifugal pump, seal (protector), and gas separator. Figure 3 shows the electrical components of the ESP system. VSC is the power electronics drive which usually consist of a rectifier, a filter capacitor, an inverter and a microcontroller. Although ESP systems generally have good efficiencies in the range of 60%, there is a vast area for improvements especially in the cable, motor and pump [5].
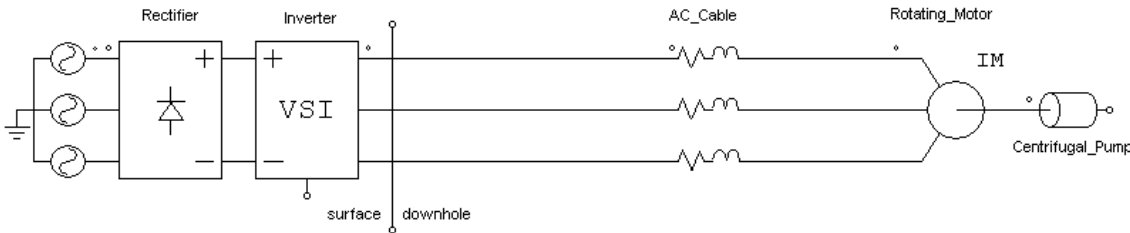
Figure 3 : Main electrical components of ESP system.

The other commonly implemented technology is the sucker rod pump –also known as beam pump. This technology leads the market for stripper (marginal oil) wells. Figure 4 shows the components of a beam pump.
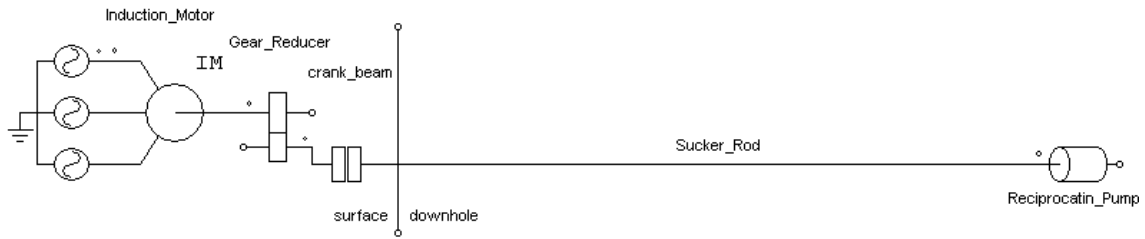
Figure 4 : Components of sucker rod pump system.

A prime mover which is usually a three-phase induction motor is used to generate a high-speed low-torque rotary motion on the motor shaft. Then, a gear reducer which consist of a V-belt and multiple gear stages is used to produce a low-speed high-torque rotary motion. Next, a four-bar linkage system (crank and beam) is used to translate the rotary motion into a linear motion on the polished rod. Finally, the polished rod drives the sucker rod and a reciprocating pump which displace the oil to the surface.

This system is the main focus of this dissertation. The design, efficiency, reliability and limitations of the sucker rod pumping system will be discussed in details in Chapter II. Because of the limitations, a linear motor based system is presented in Chapter III.

1.2   Linear motors

Permanent Magnet (PM) linear motors are being used in various applications which ranges from Maglev trains to factory automation where they started to replace many mechanical linear motion systems including ball-screws and pneumatics [6, 7].

6

Similar to rotating machines, linear machines could be induction, synchronous, PM synchronous, synchronous reluctance, switched reluctance or brushed dc machines. Linear Motors are constructed in different shapes including:

1) Flat: could be either single or double sided.

2) U-shaped.

3) Tubular.
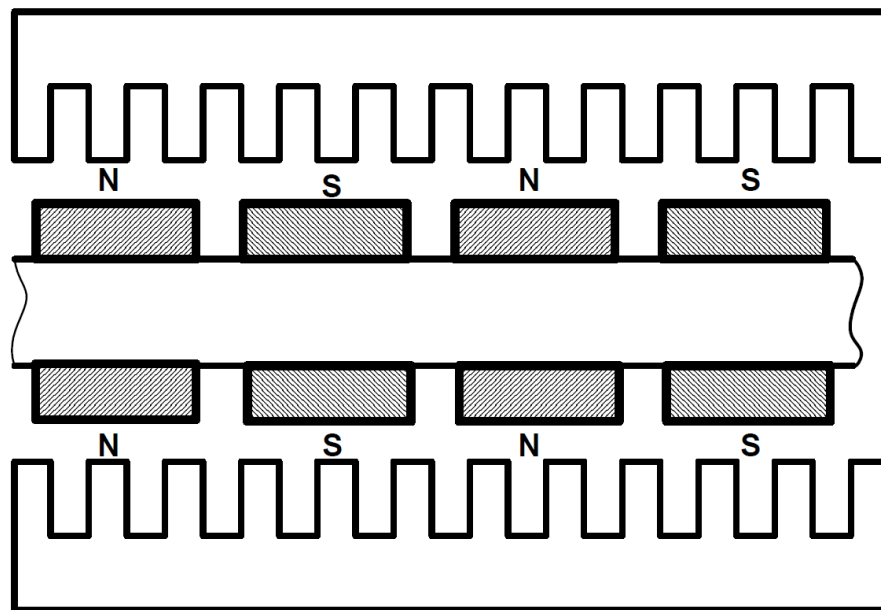
Figure 5 : Double-sided flat PM linear motor [6].

Linear motors could be driven using same control methods developed for rotating motors including [8]:

1) Six-step operation.

2) Conventional Direct Thrust Control (DTC).

3) Modified Direct Thrust Control [9,10].

4) Field Oriented Control (FOC).

The cost of these motors remains a barrier against a broader implementation. Many attempts have been made to reduce the cost or extend the operation of linear motors. In [11], the stroke was increased by running the motor while the PM is partially outside the armature winding. A sensorless control method was proposed for conventional DTC in [12] to eliminate position sensors. DTC uses the speed feedback but does not require an accurate position feedback.

In general there are two ways to drive the reciprocating pump used in sucker rod pumping system. One way is to drive the reciprocating pump directly with a linear motor. The other method to drive the pump is the use of a rotating motor along with rotary-to-linear motion translator.

The current sucker rod systems translate the rotary motion of a rotating motor to linear motion using a four-bar linkage mechanism. Alternatively, it could be driven by a rotating motor through another rotary to linear motion translator such as a ball screw.

It is important to compare the linear motor system to a rotating motor connect to a ball screw in terms of cost and reliability since both systems result in the required linear motion.

In general, the relationship between the resultant force and the input torque of a ball screw is given by:

$$F = \frac{2\pi}{l} T \qquad\qquad (1)$$

where l is the lead of the ball screw defined as the linear distance that the screw travels for one completer rotating cycle. The typical value of the lead in high power ball screw is less than 2 inches.

In general, the linear motor driven pump will be more reliable because of the elimination of the translator stage. On the other hand, it will results in a system with a lower force per unit volume compared a rotating motor and a ball screw. This means that for a given required load force the linear motor will have a larger physical size and thus cost.

Figure 6 shows a cylinder with the three cylindrical coordinates: Axial, radial and tangential. This cylinder could be the rotor of a rotating motor or the slider of a tubular linear motor.
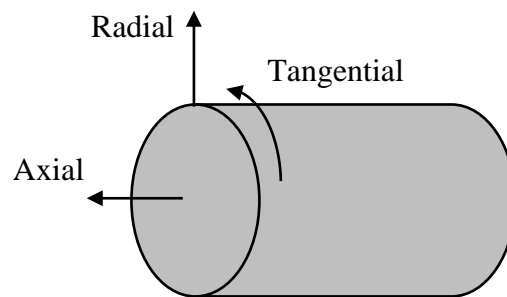
Figure 6 : A cylinder showing the axial, radial and tangential directions.

To compare the linear motor with rotating motor, the magnets flux density is assumed to be in the radial direction. Moreover, the stator current is assumed to flow on the surface of the rotor.

In a rotating PM motor, a current in the axial direction will result in a Lorentz force in the tangential direction. However for a tubular linear motor, a current in the tangential direction will result in a force in the axial direction as shown in Figure 7. This cylinder will be called the rotor in the rotating motor and a slider in the linear motor.

(a)   (b)
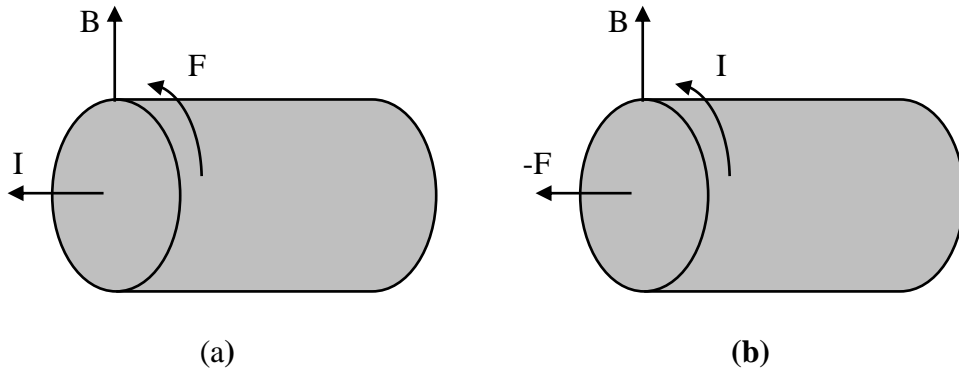
Figure 7 : (a) The rotor of a rotating motor (b) The slider of tubular linear motor.

For a given current density and a flux density, the two systems will result in shear stress of the same magnitude but in different directions. The shear stress is defined as the force per unit area and is represented by σ. For high-performance industrial servo motors, the value of the shear stress σ is around 20 kN/m^2 [13].

Assuming the cylinder has a radius r and length z, the torque of the rotating motor could be derived as the shear stress times the rotor surface area times the rotor radius as follows:

$$T = 2\pi r^2 z\, \sigma \qquad\qquad (2)$$

and the torque per rotor volume is:

$$\frac{T}{V} = 2\,\sigma \qquad\qquad (3)$$

Using equation (1), the force per rotor volume for a rotating motor with a ball screw could be derived as:

$$\frac{F}{V} = \frac{2\,\sigma}{\dfrac{l}{2\pi}} \qquad\qquad (4)$$

On the other hand, for a tubular linear motor the force could be derived as the shear stress times the area as follows:

$$F = 2\pi r z\, \sigma \qquad\qquad (5)$$

and the force per slider volume is:

$$\frac{F}{V} = \frac{2\,\sigma}{r} \qquad\qquad (6)$$

In practice the value of the radius r is usually larger than $l/2\pi$. By comparing equations (4) and (6) it could be concluded that the force per rotor/slider volume is larger for the rotating system.

For example, the required force for an application was 13 kN, the stroke length was 2 meters and the motor shear stress was assumed to be 20 kN/m². If the stator radius

11

was selected to be 35 mm and the slider/rotor radius was 14 mm, then the required motor

length for a linear motor is derived from (5) as:

$$z = \frac{F}{2\pi r \sigma} = 7.390 \; m \qquad (7)$$

This means that the stator length must be 7.390 meters and the slider length must

be 9.390 meters.

On the other hand, for a rotating motor connect to a ball screw with a lead of 20

mm, the required motor length could be derived from (1) and (2) as:

$$z = \frac{T}{2\pi r^2 \; \sigma} = \frac{F \; l}{4\pi^2 r^2 \; \sigma} = 1.680 \; m \qquad (8)$$

The total system length in this case will be 3.680 meters which is less than half of

the length of the linear motor system.

Nevertheless, a linear motor was selected for this application mainly because of

the higher reliability as mentioned previously. In any case, the discussion in the coming

chapters will apply to both systems because the linear motor model is similar to the

rotating motor model.

1.3   Dissertation organization

This dissertation is divided into six chapters the first being the introduction. In

Chapter I, current technologies in oil pumping systems were introduced. In addition, linear

motors applications and challenges were discussed.

In Chapter II, the sucker rod pumping system is analyzed. A system design

approach was discussed. The overall system efficiency and importance of reliability is

presented. Moreover, the limitations of the sucker rod pumping system are discussed. These limitations leads to the alternative system presented in the next chapter.

In Chapter III, the replacement of the sucker rod pumping system with a linear motor which drives the reciprocating pump directly is discussed. In this system, the motor drive is placed on the surface while the motor is placed downhole with the reciprocating pump. This system is named as the conventional AC system because the long cable is transmitting AC power. The use of permanent magnet linear motor along with position sensors is presented.

A new system which replaces the AC cable with DC cable is proposed in Chapter IV. A modified integrated motor drive with the speed control algorithm is suggested. In this system the inverter is integrated with the motor downhole while the rectifier remains on the surface.

In Chapter V, two sensorless algorithm are developed for both the AC and DC systems. The AC system sensorless algorithm utilizes the motor and cable models to estimate the motor position and current.

In Chapter VI, a pump monitoring system is developed to detect the most common pump faults. An observer is developed to estimate the load force which could be used along the motor position to identify various fault signatures.

Finally, the conclusions along with a discussion about the future work is presented in Chapter VII.

CHAPTER II

SUCKER ROD PUMP

Sucker rod pumping system is the most popular artificial lift method. It is being employed in 85% of oil wells which utilize artificial lift. Figure 8 shows the market share of artificial oil wells in the United States [14]. Most of these wells are marginal wells with relatively low production rates.
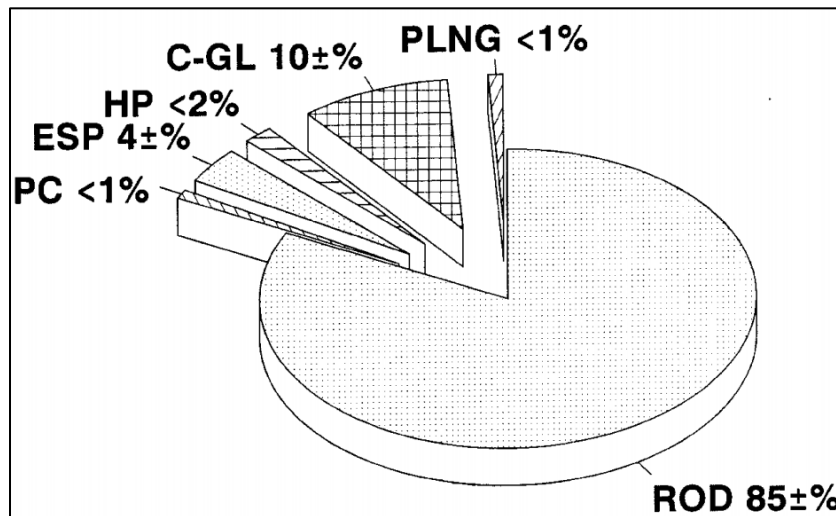
Figure 8 : Percentage of oil wells utilizing artificial lift methods in the US [14]. (ROD: Sucker rod pumps, ESP: Electric Submersible pump, C-GL: continuous gas lift, PLNG: plunger lift, HP: hydraulic reciprocating pumps, PC: progressing cavity pumps).

Sucker rod pumping system utilizes a reciprocating pump which consist of a barrel, plunger, a standing valve and a moving valve. The prime mover is usually a high-speed

three phase rotating induction motor. A V-belt along with one or more stages of gears is used to convert the high-speed rotating motion into a much slower one. For instance, the belt and gears could reduce a motor running close to 1200 rpm to 5 rpm. Then, a crank arm connected to a walking beam translate the slow rotary motion to a vertical linear motion. This linear motion drives the long sucker rod which is connected to the plunger of the pump as shown in Figure 9.

The sucker rod pump is relatively complex system. A 25th order model of this system is derived in [15].
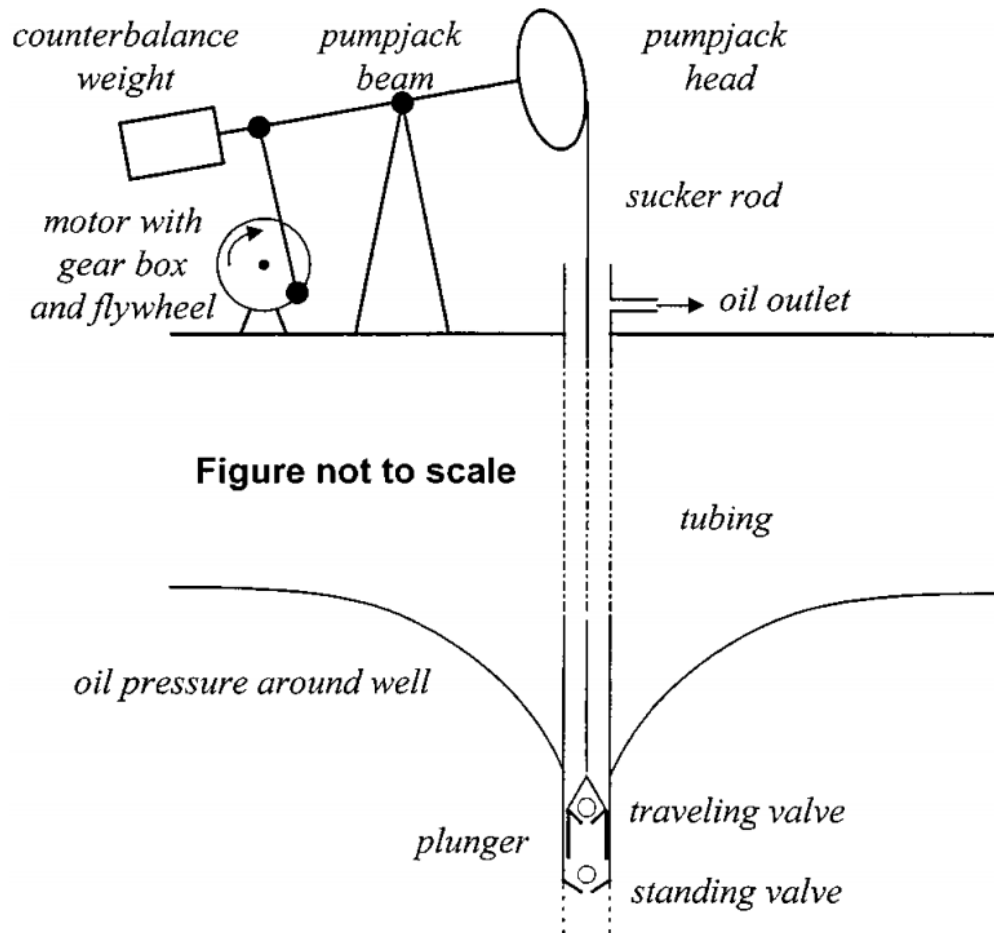
Figure 9 : Main components of sucker rod pumping system [15].

Once a pumping cycle has been completed in a low pressure oil well, the oil will require some period of time to refill the pump cavity again. This time duration varies based on the pressure in the formation and porosity and permeability of the rocks. This characteristic of the oil well is usually called reservoir inflow. Oil wells have limited inflow which could be mathematically estimated based on the rocks and fluid properties.

For this reason, running the pump continuously in low pressure oil wells is not the best practice. In practice, a timer or pump-off controller (POC) must be used. A timer with 15 minutes period is commonly used where the ON/OFF duty ratio is set by trial and error. Alternatively, POC could be used to shut off the pump when the flow is insufficient. POC utilizes a flow meter, motor ampere meter, load cell, or a dynamometer card.

2.1   Sucker rod pump design

The sucker rod pump design depends on the oil well parameters such as the fluid depth, tubing size, and specific gravity (or density) of the fluid. Moreover, it also depends on the required production rate which is governed by the pump diameter, stroke length and speed. Furthermore, the weight of the sucker rod is an important factor to design the surface unit including the counter balance weight.

The differential fluid load on the full plunger area could be calculated as:

$$F_o = A\ H\ g\ \rho_{oil} \quad [N] \tag{9}$$

where A is the plunger area, H if the fluid depth, g is the gravitational constant and ρ_{oil} is the density of the oil. The pump mechanical power could be derived as:

$$P = F_o\ v = A\ H\ g\ \rho_{oil} \times \frac{Q}{A} = H\ g\ \rho_{oil}\ Q \quad [W] \tag{10}$$

where v the fluid speed and Q is the volumetric flow rate. In English units the force could be rewritten as:

$$F_o = 12\ (0.0254)^3 \frac{\pi}{4} \times 1000 \times \frac{1}{0.45359237} G\ D^2\ H \quad [lbf] \tag{11}$$

$$= 0.3405\ G\ D^2\ H \quad [lbf]$$

17

The pump mechanical power could be rewritten as:

$$P_{hydraulic} = \frac{42 \times 231 \times (0.0254)^3}{24 \times 60 \times 60} \times 9.80665 \times \frac{12 \times 0.0254}{0.746}$$

$$\times\ G\ H\ Q \quad [HP]$$

$$= \frac{G\ H\ Q}{135629.61} \quad [HP]$$

(12)

where D is the plunger diameter in inches, Q is the volumetric flow rate in Barrel per day (BPD) and H is the fluid depth in ft. G is the specific gravity defined as:

$$G = \frac{\rho_{oil}}{\rho_{H_2O}}$$

(13)

The specific gravity G could be derived from the API gravity as:

$$G = \frac{141.5}{API\ gravity + 131.5}$$

(14)

The pump displacement could be measured in barrels per day (BPD) as:

$$Q = \frac{24 \times 60}{42 \times 231} \frac{\pi}{4} S_p\ N\ D^2 \quad [BPD]$$

(15)

$$= 0.1166\ S_p\ N\ D^2$$

where S_p is the bottom hole pump stroke in inches and N is the Pumping speed in strokes per minute (SPM). The buoyant rod weight is given by:

$$W_{rf} = W\left(1 - \frac{\rho_{H_2O}}{\rho_{steel}} G\right) = W(1 - 0.128\ G)$$

(16)

Because of the elastic nature of the sucker rod, the polished rod load (PRL) is not equivalent to the differential fluid load on plunger F_o and the polished rod stroke S is not equivalent to the bottom hole pump stroke S_p. The elastic nature of the sucker rod makes

18

the design process complex. Dynamometer cards utilizes measurement of the polish rod force and position on the surface to estimate the downhole pump position and force using a mathematical solution of the rod wave equation. Alternatively, API TR 11L standard procedure uses the collected data from many dynamometer cards to present a design calculations and procedure. The design process utilizes formulas, tables and figures derived from many experimental measurements.

A counter balance weight is added to balance the weight of the upstroke and down stroke cycles. Without this weight, the system will be highly unbalanced. During the upstroke the unit is lifting both the fluid and the rod string which exerts a heavy load on the gear and motor. While during the down stroke, the motor is not doing any work. The gravity will pull the rod string down. To balance the upstroke and down stroke forces are balanced, the counter balance weigh is designed as:

$$CBE = W_{rf} + \frac{F_o}{2} \qquad (\,17\,)$$

For a well which its parameter are given in Table 1,

Table 1 : Well and pump parameters.

Parameter	Symbol	Value	Unit
Fluid level depth	H	4500	feet
Plunger diameter	D	1.5	Inch
Pumping speed	N	16	SPM
Stroke length	S	54	Inch
Total rod weight in air	W	9165	Lbs
Specific gravity	G	0.9	

the required hydraulic pump power could be calculated from equation (12) as:

$$P_{hydraulic} = \frac{1}{135629.61} \times 0.9 \times 4500 \times 175 \qquad (18)$$

$$= 5.22 \ [HP]$$

The surface end side of the rod is connected to a polished rod. The polish rod horse power (PRHP) calculated from API TR 11L standard is:

$$PRHP = 8.5 \ [HP] \qquad (19)$$

Because of the cyclic nature of the pump, the elasticity of the rod and the mechanical losses in surface unit, the common practice is to choose a motor with power rating twice the PRHP even for a counterbalanced system.

$$P_{name\ plate} = 2 \times 8.5 \ = 17 \quad [HP] \qquad (20)$$

Another method to calculate the motor power is given by:

$$P_{name\ plate} = \frac{H\,Q}{PMF} \quad [HP] \qquad\qquad (21)$$

where H is the depth in feet and Q is the flow in BPD. PMF is the prime mover factor which is 45000 for NEMA C motors and 56000 for NEMA D motors. This will result in HP rating from 14 to 17.5.

2.2   System efficiency

Sucker rod pumps has an overall system efficiencies in the range of 50 to 60%. This is considered as a relatively high efficiency compared to other acritical lift methods as shown in Figure 10 [14].
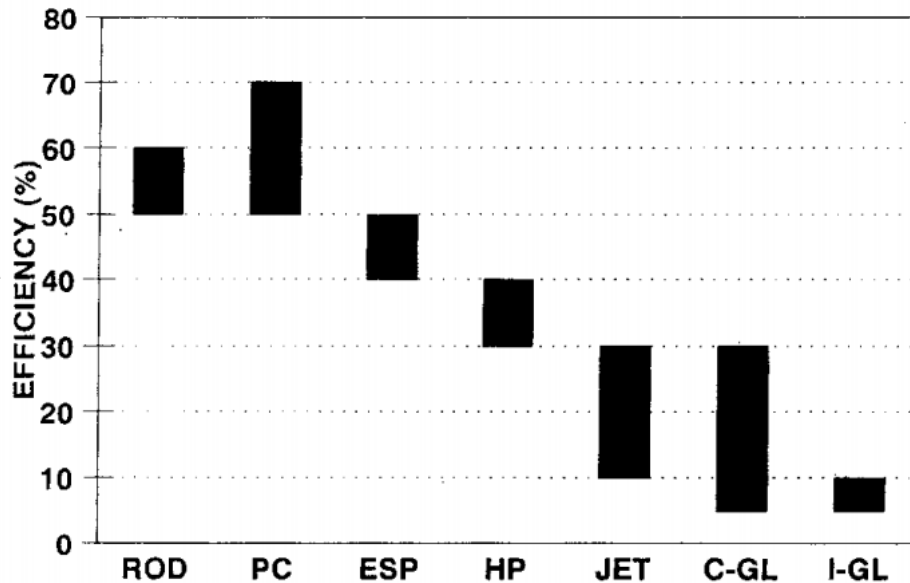
Figure 10 : Artificial lift methods efficiencies [14].
(ROD: Sucker rod pumps, PC: progressing cavity pumps, ESP: Electric Submersible pump, HP: hydraulic reciprocating pumps, C-GL: continuous gas lift, I-GL: intermittent gas lift.

The system overall efficiency is defined as follows:

$$\eta_{system} = \frac{P_{hydraulic}}{P_{motor\_in}} \qquad (22)$$

The overall efficiency could be divided into the following components [16]:

2.2.1 Lifting efficiency

Lifting efficiency include the hydraulic and friction losses. Hydraulic losses account for the fluid leakage in the pump by comparing the actual produced flow to the full pump displacement. Friction losses are a result from the rod rubbing against the tubing and stuffing box friction.

22

$$\eta_{lift} = \frac{P_{hydraulic}}{PRHP} \tag{23}$$

If the pumping mode is well designed, a lifting efficiency above 90% could be achieved.

2.2.2   *Surface unit efficiency*

This account for losses in the V-belt, gear reducer and bearings.

$$\eta_{surface} = \frac{PRHP}{P_{motor\_out}} \tag{24}$$

As shown in Figure 11, efficiencies could reach 90% for well-maintained units operating near the rated torque [17].
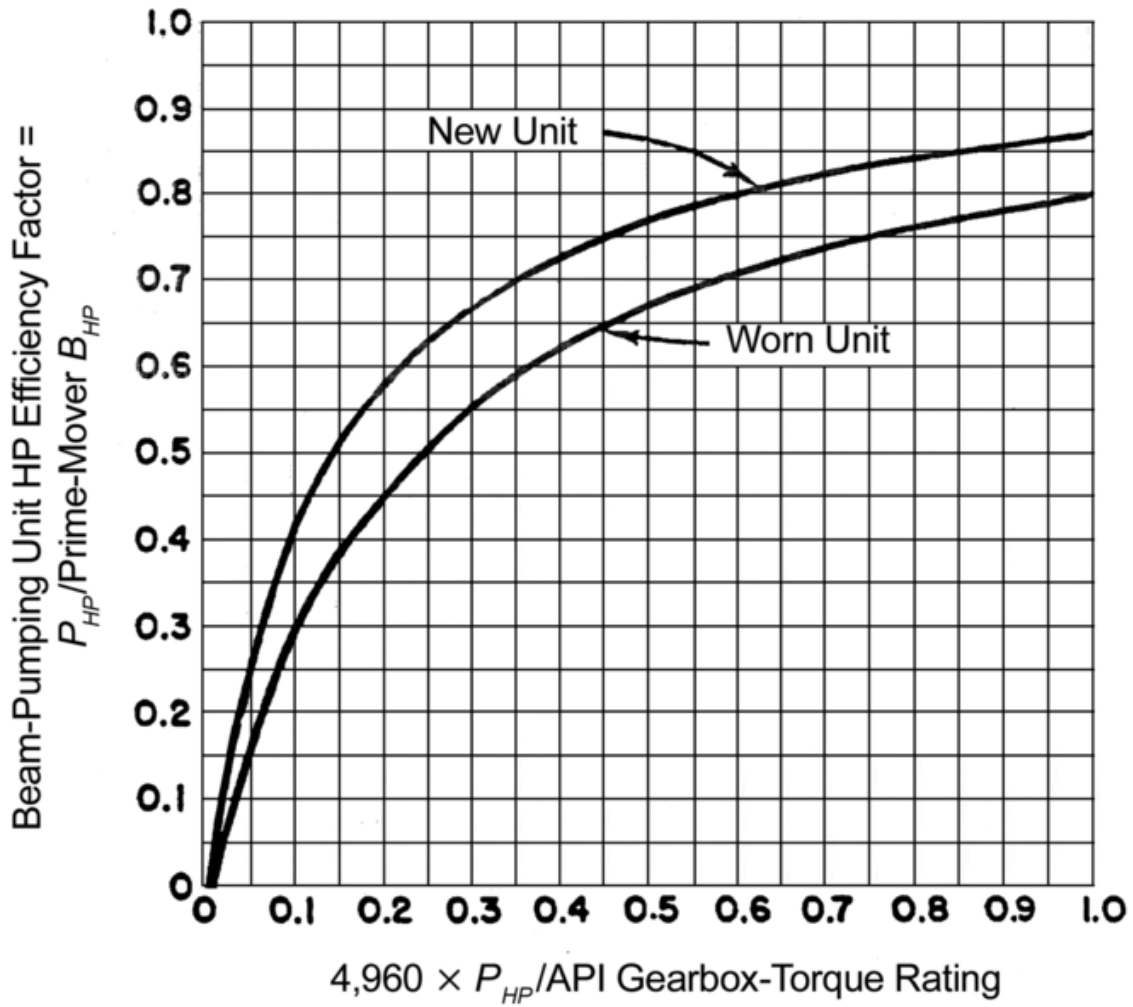
Figure 11 : Surface unit efficiency [17].

2.2.3 Motor efficiency

NEMA D motors which are commonly used in this application can have efficiencies around 85% if operated at rated conditions. Because the motor is usually overdesigned, the efficiency can drop to around 75%.

$$\eta_{motor} = \frac{P_{motor\_out}}{P_{motor\_in}} \qquad (25)$$

2.3   System reliability

Although some cost saving could be achieved by optimizing efficiency as shown in [18], the efficiency of the system itself is not an important issue in practical situations. This could be shown by the following example. For instance, an oil well parameters given in Table 1, the cost of electricity assuming a 0.11 \$/Kwh and 60% system efficiency could be calculated as:

$$electricity\ cost\ per\ year = \frac{P_{hydraulic}}{\eta_{system}} \times 0.11 \times 24 \times 365 \qquad (26)$$

$$= 6260\ \$/year$$

Assuming 40\$ price per barrel, the total annual income could be calculated as:

$$annual\ income = 175 \times 365 \times 40 = 2,555,000\ \$/year \qquad (27)$$

This means that the cost of electricity is less than 0.25% of income which makes it insignificant in cost analysis. The main cost components are the royalties paid to the land owner, operating and maintenance costs and any shutdowns which results in loss of production.

In practice, small reduction in efficiency is not an important parameter by itself unless it causes the production barrels per day to decline. Moreover, monitoring these efficiencies is critical for failure analysis. Any increase in these loses may lead to failure which means a total production shut down. An average shut down time of 5 days will cost 1.37% of the annual income plus repair costs. It is critical that the sucker rod pumping unit operate without any failure. Figure 12 shows the number of failures in pump, rod, tubing per well per year [19].
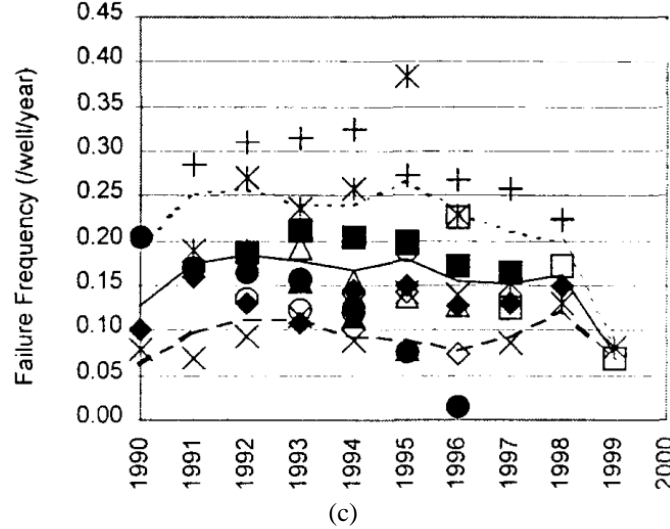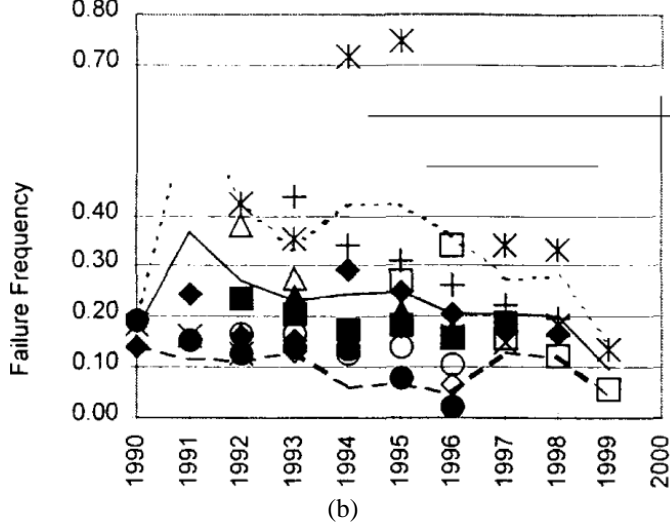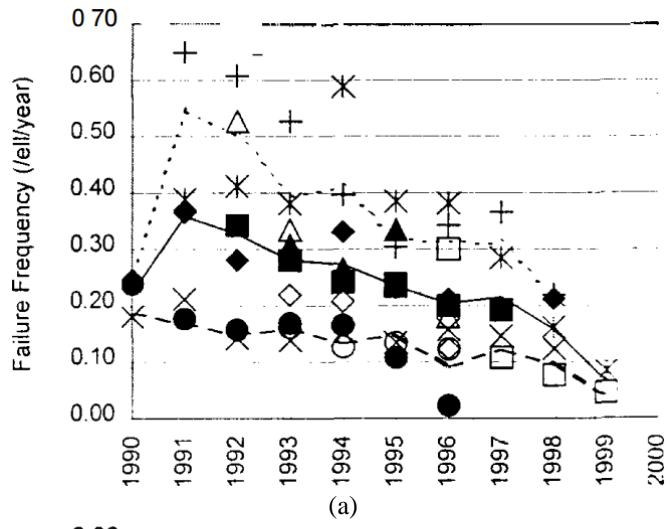
Figure 12 : Failure frequency per well in (a) Pump (b) Rod (c) Tubing [19].

2.4   Sucker rod pump limitations

Although sucker rod pumping is proven to be a great technology for the past several decades, it has four main limitation:

1) First, it cannot be used in horizontal wells and should not be used in deviated wells. Using sucker rod pump in deviated wells will result in very poor efficiency. More importantly, the continuous friction will cause the rod and tubing to wear. This will increase the chances of failure and thus a reduced production rate or even a complete system shutdown.

2) Second is the limitation of being used in off-shore oil wells because of the limited space on the platform which cannot accommodate the large footprint of the surface unit.

3) Third, the strength and weight of the sucker rod is the limiting factor for the well depth and is the main barrier against implementation in deeper wells.

4) Finally, even in non-deviated wells, the rod is one of the two main failure points as shown previously in Figure 12. Eliminating the sucker rod will results in a system with higher reliability.

For these reasons, some alternatives to the sucker rod beam pump has been proposed. The aim of these alternatives is to replace the slider crank (Four-bar linkage) surface unit with other rotary motion to linear motion translators. These include using a scotch yoke (slotted link), ball screw, rack and pinion systems or even using linear motor on the surface to drive the sucker rod.

In this work, a downhole linear motor was proposed as an alternative method to drive the reciprocating pump directly without a sucker rod as will be discussed in the next chapter. This will address the limitations in the sucker rod pumping system which means that this system has a higher reliability and could be used for deviated wells, off shore wells and deeper wells.

CHAPTER III

THE CONVENTIONAL AC SYSTEM

This chapter discusses the application of linear motors to directly drive the reciprocating pump in sucker rod pumping systems. The main goal is to replace all the components of the sucker rod pumping system with only a linear motor and a reciprocating pump. These systems are already developed and commercially available. In existing systems, a surface controller consists of a rectifier and inverter is connect through a long AC cable to a linear induction motor placed downhole which is used to drive the reciprocating pump.

This relatively recent technology which combines the ESP and sucker rod pump has been introduced for stripper wells. The rotating ESP configuration is modified to have a linear ESP system. In this case, a linear motor is used instead of a rotating motor and the centrifugal pump is replaced with a reciprocation pump as shown in Figure 13. This system results in higher efficiency.
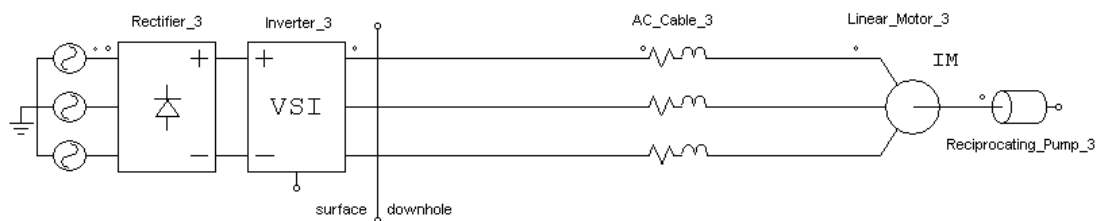
Figure 13 : Main components of Linear ESP systems.

In this project, the induction motor in the existing system shown in Figure 13 is replaced by permanent magnet (PM) motor.

3.1   Effects of high temperature

Since the motor is placed downhole where the ambient temperature is around 400^oF ($\sim200^o$C), the effects of this high temperature on the main motor components must be taken into consideration.

3.1.1   Motor winding

The high temperature will increase the resistance of the motor. This high temperature resistance could be calculate as:

$$R_{@T} = R_{@25^o}\big(1 + \alpha\,(T - 25^o)\big) \qquad\qquad (\,28\,)$$

where α is the temperature coefficient which is equal to 0.00393 for copper. For example if the motor winding resistance was 3.1Ω at 25° C, the resistance at 400° F which is 204° C will be 5.28 Ω. This will increase the copper losses. Moreover, the resistance rise must be taken into account when any model based control is applied.

Moreover, conventional winding insulation cannot be used at high temperature. The rated temperature of the insulation must not be exceeded. Any 10° C increase above the insulation rated temperature will reduce the insulation life time by half.

For this application, a polyimide film which is rated at 240° C must be used. Some types of polyimide films that may be used include poly (4,4′-oxydiphenylene-

pyromellitimide) and biphenyl-tetracarboxylic acid dianhydride (BPDA) type polyimide films.

3.1.2 Electric steel

As temperature T increases, the magnetization M of a magnetic material decrease until it reaches a point where it loses all the magnetization. This temperature is known as the Curie temperature Tc which is 1043° K for steel.

For an applied magnetic field H, the magnetization M is defined as

$$M = \chi_v\, H \qquad\qquad (29)$$

where χ_v is the magnetic susceptibility. The total flux density B will be:

$$B = \mu_o(H + M)$$

$$= \mu_o(H + \chi_v\, H) = \mu_o(1 + \chi_v)H = \mu_o\mu_r H \qquad (30)$$

where μ_o is the permeability of free space and μ_r is the relative permeability of electric steel defined as $(1 + \chi_v)$. The temperature dependence of magnetization is given by [20]:

$$\frac{M(T)}{M(0)} = tanh\left(\frac{M(T)}{M(0)}\cdot\frac{T_c}{T}\right) \qquad (31)$$

where M(T) is the magnetization at a given temperature T and M(0) is the magnetization at an absolute zero temperature. Figure 14 shows a plot of equation (31). For steel at 400° F ~ 477° K, the magnetization is reduced by less than 3% which might be negligible. This effect may be taken into account by redefining the relative permeability of the steel as follows:

$$\mu_{\mathrm{r}} = \left(1 + \frac{M(T)}{M(0)} \cdot \chi_v \right) \qquad\qquad (\,32\,)$$

Effectively, the increase in temperature will cause relative permeability of the electric steel to drop. This drop which is less than 3% at 400° F can be neglected.
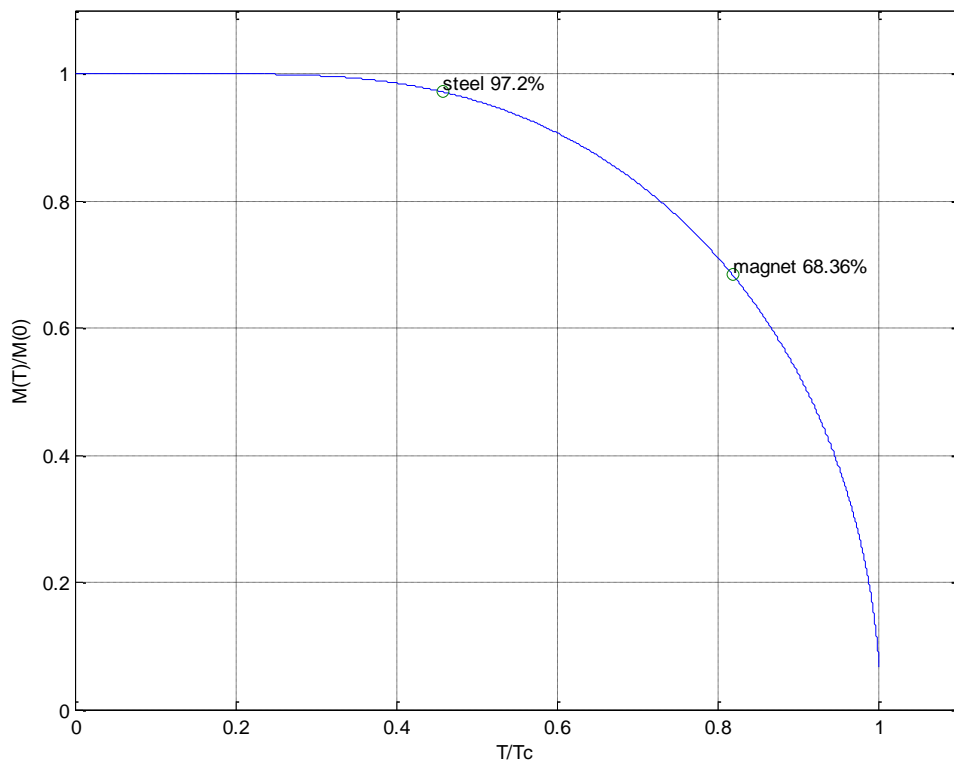
Figure 14 : Temperature effects on magnetization.

3.1.3 Permanent magnet

Figure 14 could be used to analyze the temperature on the permanent magnet too. In this case, $Nd_2Fe_{14}B$ magnet was used which had a Curie temperature of 583° K. Since the system temperature of 477° K is close to the Curie temperature, the effect of temperature rise on the permanent magnet is significant. At this temperature, the magnet has 68.36% of the magnetization at absolute zero temperature. For instance, a magnet with a flux density of 1.2T will have a flux density of 0.82T at this temperature.

Furthermore, the high temperature will reduce the magnetic coercivity which makes the permanent magnet vulnerable to demagnetization due to the stator field.

Figure 15 shows an example of thermal behavior of a Nd2Fe14B magnet. It is clear how the high temperature is reducing both the remanence flux and the coercivity.
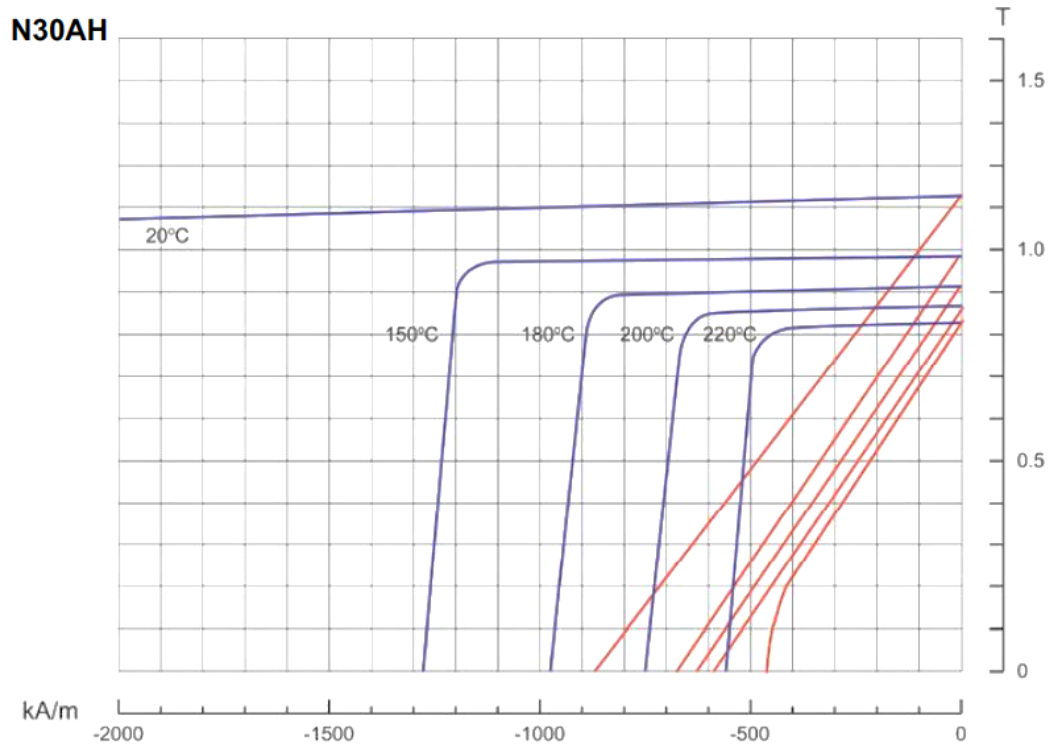
Figure 15 : Normal and intrinsic BH curves showing the thermal behavior of N30AH neodymium magnet.

In some cases, Dysprosium (Dy) may be added to the $Nd_2Fe_{14}B$ magnet in order to improve the coercivity. Dysprosium is a heavy rare earth elements and is quite scarce and expensive. Alternatively new materials are being developed to enhance the Curie temperature of the permanent magnet without sacrificing the magnetization. For instance, introducing nitrogen to $R(Fe, M)_{12}N$ (R = rare earth element, and M = Mo, Ti, and V) increased the Curie temperature by more than 200° K [21].

The Alnico magnetic alloy is one of the first material used to produce strong magnets. It has been commercially available for the last several decades. It has a Curie

temperature of ~1500° F which makes it suitable for high temperature applications. On the other hand, it has a relatively low coercivity which makes it vulnerable to demagnetization.

3.1.4   Bearing

Most motor bearing are designed to operate around 150° F. At 400° F, special bearing must be used. High temperature bearing are usually deep groove ball bearings with graphite-based lubricant.

3.1.5   Motor drive

In the topology presented in this chapter, the rectifier and inverter are placed on the earth surface and not downhole at the 400 °F temperature. In this case, power diodes along with IGBT switch could be used. Based on the ambient temperature, a microcontroller and current sensor could be selected. The current sensor measures the inverter output current which is not equivalent to the motor input current because of the cable capacitive charging and discharging. The estimation of the motor current from the inverter current will be discussed in Chapter V.

In the other topology which will be presented in Chapter IV, the inverter is placed downhole. In this case, the commonly used IGBT or power MOSEFT cannot operate at high temperature. For this reason, a wide bang gap device such as Silicon Carbide (SiC) or Gallium Nitride (GaN) must be used as will be discussed in the next chapter. To measure the current, a high temperature shunt resistance with high temperature operational

amplifier may be used. Moreover, the soldering rated at high temperature such as indium

lead solder (95.5Pb/2Sn/2.5Ag) must be used.

3.2   Field Oriented Control of PM linear motor

The $Nd_2Fe_{14}B$ permanent magnet are more vulnerable to demagnetization at higher

temperature as shown in the previous section. In order to protect the magnets, Field

Oriented Control (FOC) was selected for this application. FOC requires a precise and

accurate position feedback which is usually achieved by an incremental optical or

magnetic encoder which include al long strip scale.

In this dissertation, a tubular PM linear motor was employed although the same

model could be derived for flat and U-shaped linear motors. The motor model in the

synchronous reference frame is given by [8],

$$\begin{bmatrix} v_d \\ v_q \end{bmatrix} = \begin{bmatrix} R + sL_d & -\omega L_q \\ \omega L_d & R + sL_q \end{bmatrix} \begin{bmatrix} i_d \\ i_q \end{bmatrix} + \begin{bmatrix} 0 \\ \omega \lambda_{pm} \end{bmatrix} \tag{33}$$

The relationship between the angular and linear frames is given by,

$$\omega = \frac{\pi}{\tau_p} u \tag{34}$$

and,

$$\theta = \frac{\pi}{\tau_p} x \tag{35}$$

Where x and u are the linear shaft position and speed respectively and τ_p is the

pole pitch. The force could be derived as,

36

$$F_{em} = \frac{3}{2} \frac{\pi}{\tau_p} (\lambda_{pm} \, i_q + (L_d - L_q) \, i_d \, i_q)$$
(36)

To control the shaft position of the linear motor using Field Oriented Control, three closed loop control loops are required. The most inner loop is the current loop where two PI controllers are used to force the motor current to track the reference currents. Because there is no variation in the inductance of this motor as the position changes ($L_q = L_d$), a control scheme similar to surface mounted PM motor could be implemented. The current I_d^* was commanded to be zero while the current I_q^* which represents the force command was set to be the output of the speed loop. Another PI controller is designed to close the speed loop. Finally, a position loop is formed where the output of the controller is employed as the command speed as shown in Figure 16.
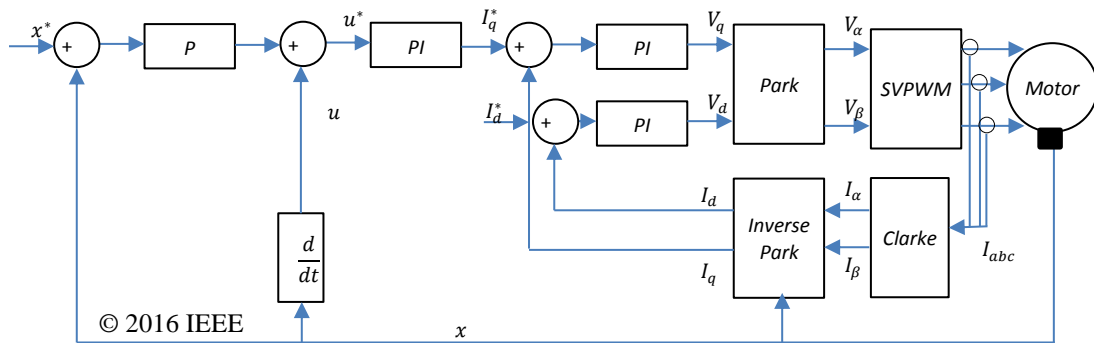

Figure 16 : Block diagram of Field Oriented Control of the PM linear motor.

3.3 Position and current sensors

Operation and control of PM motor described in the previous section requires the position of the motor to be measured and fed back to the controller. Although using an incremental linear encoder to control the motor is an effective and reliable solution, it has many disadvantages such as the high cost, difficulty of installation, trailing sensor cable, the need for offset calibration and the unknown position at start-up may create challenges for implementation in real life applications.

An alternative solution is to use the less expensive linear Hall sensors [8]. In this case, two Hall elements are required where the first is placed in phase with one winding and the second is shifted by 90° electrical degrees. If the motor windings are designed to be stationary with a moving magnet, then the sensor will be stationary too. Since the air gap flux is sinusoidally distributed, the output of two sensors will be a sine and cosine functions of the position. Using an Analog to Digital Converter (ADC), these two signals could be supplied to a microcontroller where they can be directly used for Park and inverse Park transformations.

This solution may not be practical in some real life applications due to the inevitable noise in the measurements. A Phase Locked Loop (PLL) may be used to extract the position information from these signals. Linear Hall sensors were implemented to drive a rotating PM motor directly in [22] and using PLL in [23]. The implementation of Hall effect sensors to provide the position feedback will be discussed in section 4 of this chapter.

However, if the inverter is on the surface and the motor and pump are several thousands of feet downhole, it is not practical to place even a Hall Effect position sensor downhole. This is mainly because of the high temperatures downhole and the long signal cables required carrying the signals back to the surface controller. Delivering the signal through this long distance is a huge challenge using digital signals, analog signals or even 4-20 mA current loops.

Moreover, in order to efficiently controller the PM motor, the motor current must be measured and fed back to the controller too. Since the motor and pump are several thousands of feet downhole, it is not practical to place a current sensor downhole. This is mainly because of the high temperatures downhole and the long signal cables required carrying the signals back to the surface controller as discussed previously.

Alternatively, an observer may be used to estimate the motor position and current. A position sensorless control algorithm may be used to estimate the motor position. Many position sensorless algorithms have been developed for rotating motors. Since the model of a linear PM motor is similar to the rotating one, algorithms developed for rotating motors could be adopted for linear motors. However, it should be noted that in linear motion the ability to start from standstill under load and speed reversal are essential.

For motor with inductance saliency, high frequency injection methods could be used to extract the motor position. If the motor has no saliency, Back-EMF based models could be used.

To solve the current measurement problem, an observer which utilizes the measured voltage and current on the inverter output is developed to estimate the current

on the motor terminal. The model-based observer is constructed based on the motor and cable models.

First, the cables per length parameters are measured using a sample of the cable or estimated using finite element analysis (FEA). Although these parameters are distributed along the cable length, a lumped parameter model was developed in order to test the system in lab environment.

The Luenberger observer shown in Figure 17 estimates the motor current and the motor back EMF which will be used to estimate the motor position. This will eliminate the need for a current or position sensor on the motor side. The details of the control algorithm are presented in chapter V.
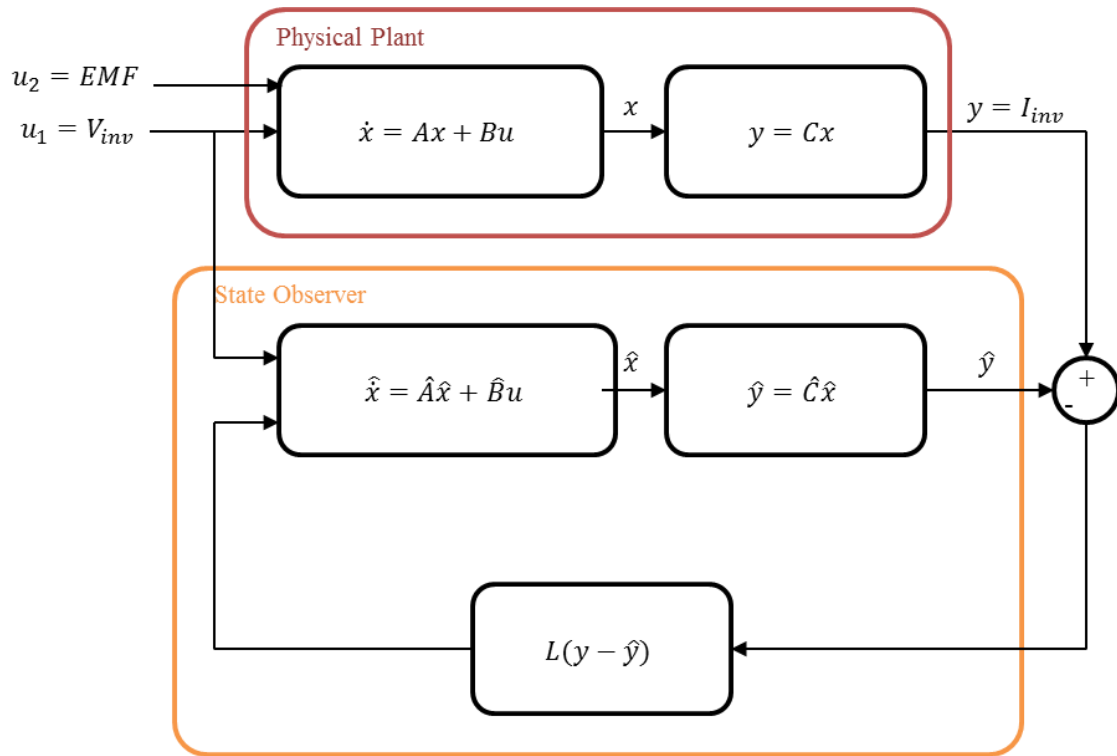
Figure 17 : Luenberger observer.

Utilizing this observer will allow a FOC of the motor without any position sensor and without any downhole current sensor. Only a surface current sensor will be used to measure the inverter output current.

3.4 Linear Hall effect position sensors

In this section, the method of measuring the shaft position using two linear Hall sensors with PLL is discussed. These sensors will be used to provide the benchmark which the estimated position from the sensorless algorithm will be compared to. This

configuration is not intended to be employed in the real life application because these sensor usually have a temperature rating of 150º C.

First, the two Hall elements were placed in a position where the stator magnetic field is negligible. This results in reduced stroke. Figure 18 shows the sensor placement where the first linear hall sensor was placed in phase with winding 'A' and the second sensor is placed after 90 electrical degrees so that they can provide the perfect sine and cosine signals with the same gain and no offset or saturation [8].
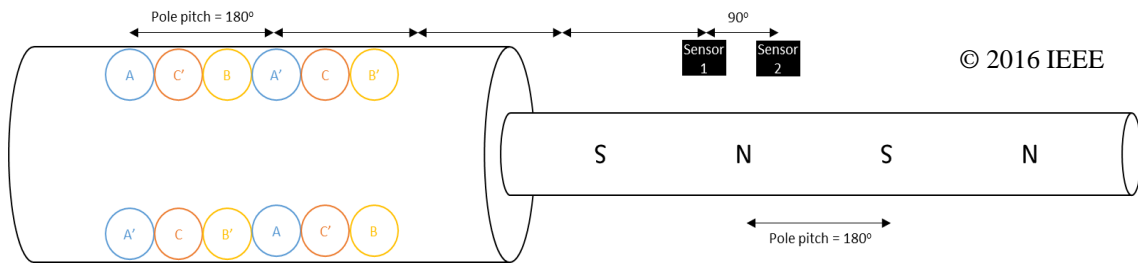
Figure 18 : Linear Hall sensor placement.

However, the sine and cosine signals were too noisy to be employed directly in the closed loop system. Moreover, the speed calculation requires the derivative of these noisy signals which will amplify the noise.

As an alternative, the error in position was calculated and a PLL was formed to compensate for this error. The sine and cosine signals are basically the flux in the two axes of the stationary reference frame given in per unit. Transforming these signals to the

natural reference frame will result in λd = λpm and λq=0 as expected. The estimation process starts from an estimated frame with a position $\hat{\theta}(t)$ as shown in Figure 19.
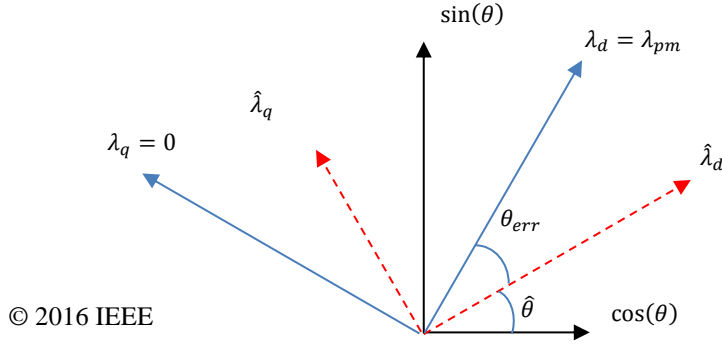
Figure 19 : Estimating the position error from sine and cosine signals.

The error in shaft position is defined as,

$$\theta_{err}(t) = \theta(t) - \hat{\theta}(t) \qquad (37)$$

Transforming the sine and cosine signals to the estimated reference frame will result in,

$$
\begin{bmatrix} \hat{\lambda}_d \\ \hat{\lambda}_q \end{bmatrix} =
\begin{bmatrix} \cos(\hat{\theta}) & \sin(\hat{\theta}) \\ -\sin(\hat{\theta}) & \cos(\hat{\theta}) \end{bmatrix}
\begin{bmatrix} \cos(\theta) \\ \sin(\theta) \end{bmatrix} \lambda_{pm} \qquad (38)
$$

$$
= \begin{bmatrix} \cos(\theta_{err}) \\ \sin(\theta_{err}) \end{bmatrix} \lambda_{pm}
$$

Then, the error between the real and estimated position could be derived as,

43

$$\theta_{err}(t) = \tan^{-1}\left(\frac{\hat{\lambda}_q}{\hat{\lambda}_d}\right) \qquad (39)$$

Finally, a PI controller is designed to compensate for this error and get the position and speed information. The same structure has been proposed for position sensorless drives [24]. The output of this controller is the speed which could be integrated to get the position as shown in Figure 20.
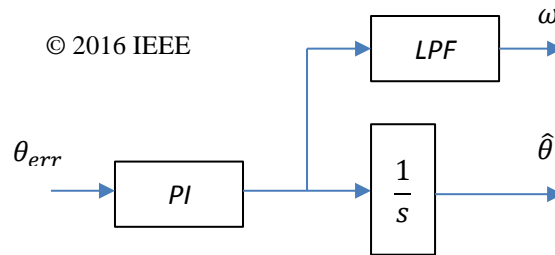
**Figure 20 : Phase Locked Loop consists of a PI controller, an integrator and a low pass filter.**

Compared to an incremental encoder, this approach will result in a less expensive and smaller size absolute motor shaft position sensor with a stationary cable.

In theory, three types of sensor placement errors are possible:

1) If the two sensors are still 90o apart but both are shifted with respect to winding 'A' with a small offset.

44

2) The first sensor is placed perfectly in phase with winding 'A' but the second sensor is not exactly 90° apart.

3) One of the two sensors has a different gain.

In practice, any of these scenarios are possible. The worst case scenario will be a combination of these three. However, in this section each case is discussed individually. To show the effect of the first case, the motor was assumed to run at 1 Hz and a 5° offset was introduced to both sensors. Since the error in position is constant, the force was reduced but no ripple was introduced as shown in Figure 21 [8].
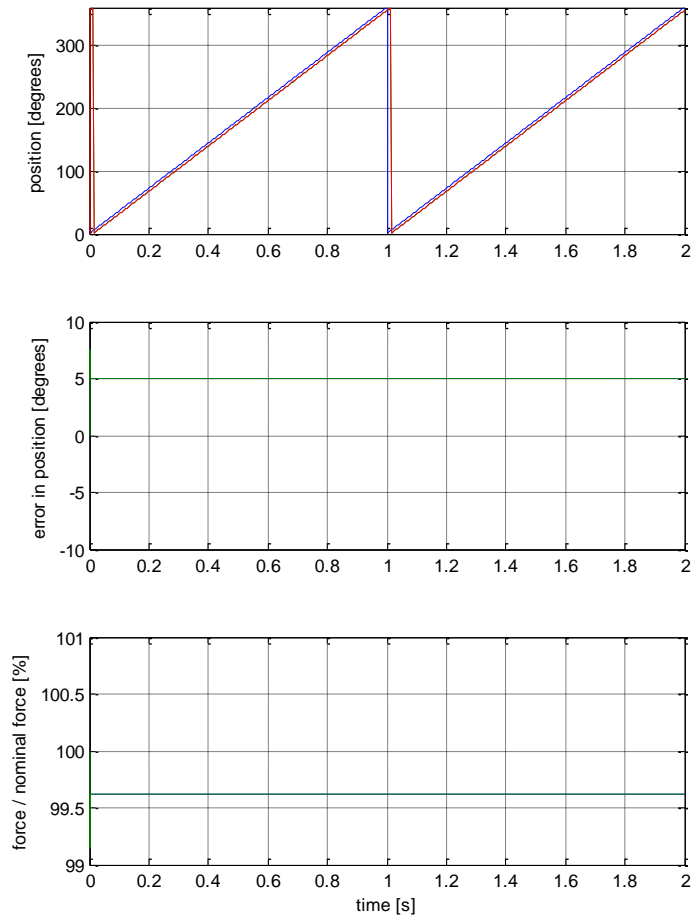
Figure 21 : (a) Real and measured motor electrical position, (b) Error in the position, (c) Percentage of resultant force compared to nominal force for the first case.

Figure 22 shows the results of the second case where the motor is running at 1 Hz and a 5° offset was introduced only to the second sensor. In this case, a force ripple was resulted.
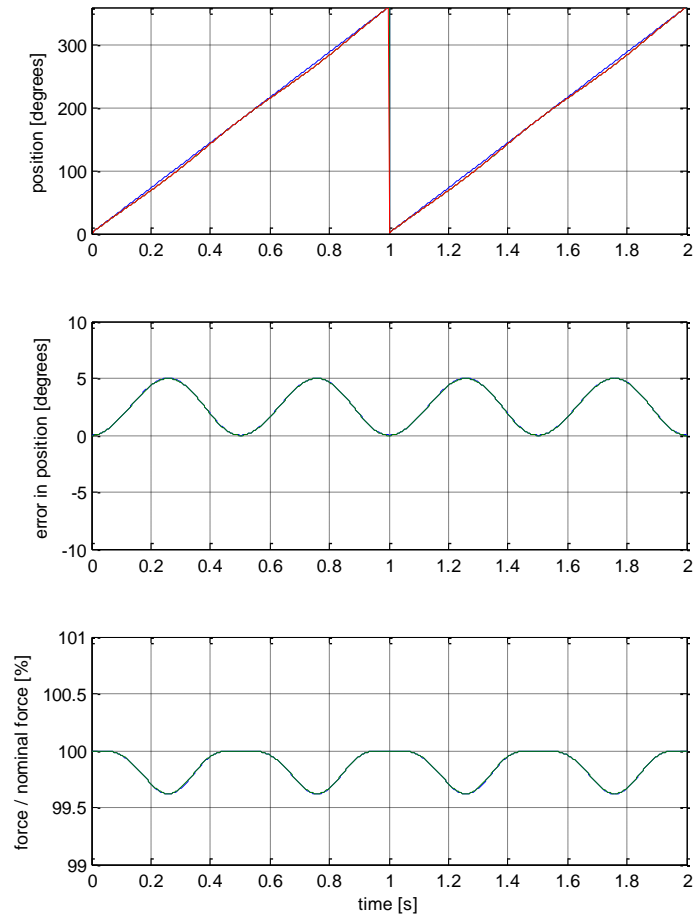
© 2016 IEEE

Figure 22 : (a) Real and measured motor electrical position, (b) Error in the position, (c) Percentage of resultant force compared to nominal force for the second case.

For the third case, a 10% gain was added to the second sensor. Again a force ripple was observed as shown in Figure 23. In general, the ripple will be less because the error in position in this case happens in both directions where in the second case the error was only positive.

Figure 23 : (a) Real and measured motor electrical position, (b) Error in the position, (c) Percentage of resultant force compared to nominal force for the third case.
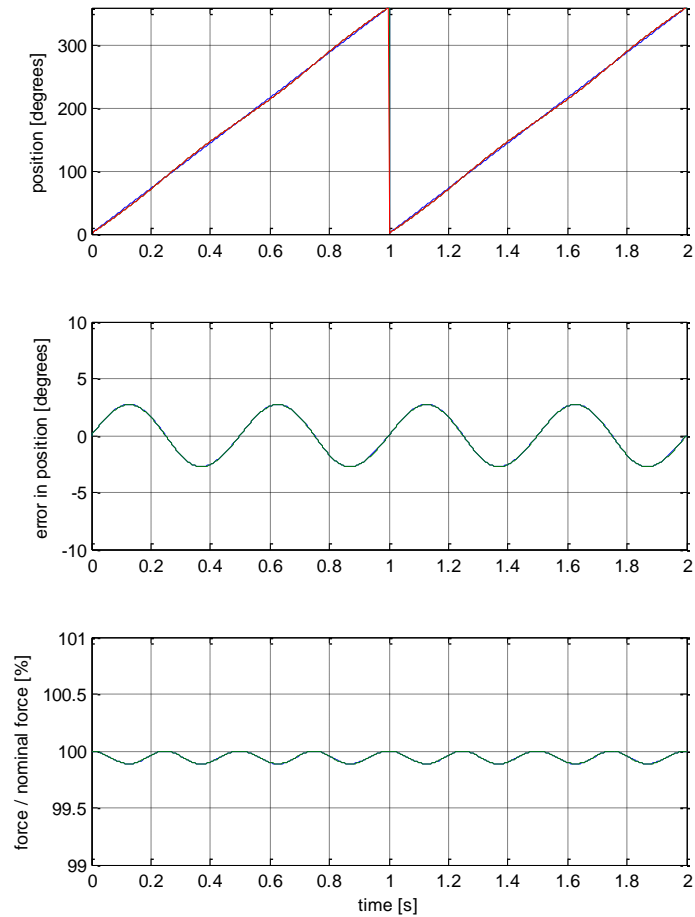
In the experimental test presented in the next section, misplacement error was still present despite the fact that great care was taken to place the sensors accurately. A combination of both the second and third case was detected. The two sensors where 89° degrees apart instead of 90° and the 3.5% difference in the gain of the two sensors was present. The Analog to Digital Converter (ADC) gain was adjusted to compensate for the

48

sensors gain difference. Based on the results of this section, the effects of 1º offset misplacement was assumed to be negligible.

Position FOC was implemented [8] using two different position sensors. An incremental magnetic encoder with a resolution of 5 μm was used to detect the correct position for the purpose of comparison and evaluation only and was not used to control the motor. Two DRV5053 analog bipolar Hall Effect sensors connected to a 12-bit ADC were used to provide the motor shaft position feedback to the control loop.

A dc bus voltage of 60 V along with a three phase IGBT inverter switching at 10 kHz were used to drive the three-phase Tubular PM linear motor. The winding assembly was mounted to the base while the magnetic rod was allowed to slide freely and drive the load.

The motor was loaded using a Trans-Rotary Magnetic Gear (TROMAG) [25]. The load force was selected to be half of the rated continuous motor force. In Figure 24, the Hall sensors and their output signals are shown.
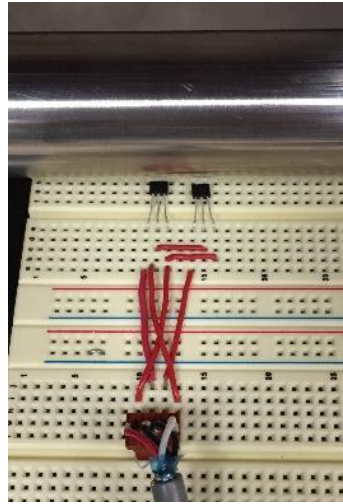
© 2016 IEEE

(a)
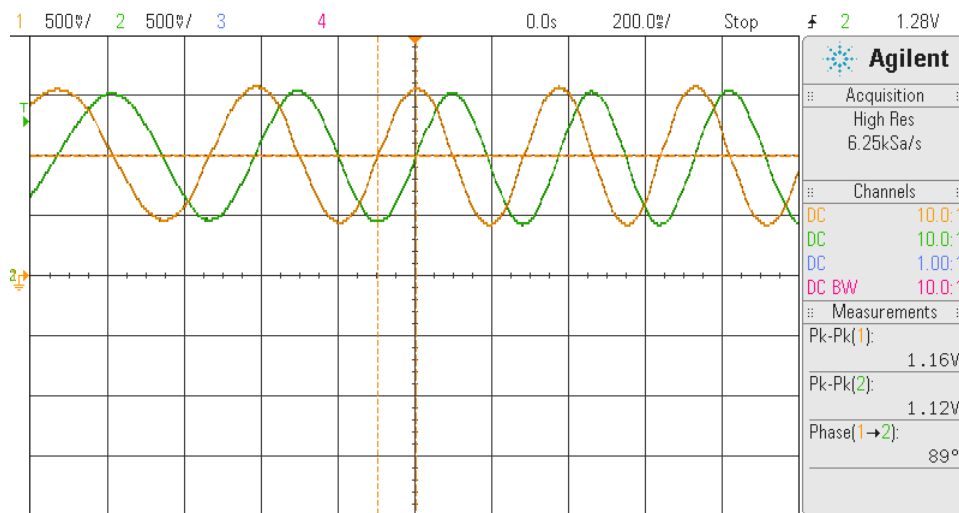
(b)

Figure 24 : (a) Prototype showing two DRV5053 Hall sensors placed 90 degrees apart under the magnetic shaft, (b) The PM flux distribution measured by the two Hall sensors as the shaft moves.

The position and speed derived from the linear encoder were used to monitor the

real values but were not utilized in the control. Figure 25 compares the position derived

from the two sensors while the position and speed derived from Hall sensor is used to close the three loops.

Figure 26 shows the speed derived from both methods. From Figure 25 and Figure 26, it is clear that there is a good agreement between the results obtained from the two methods. In Figure 25, there is an offset in the position derived from the Hall sensors. The maximum error was around 4 electrical degrees. In Figure 26, the speed derived from the Hall sensor had more ripple.
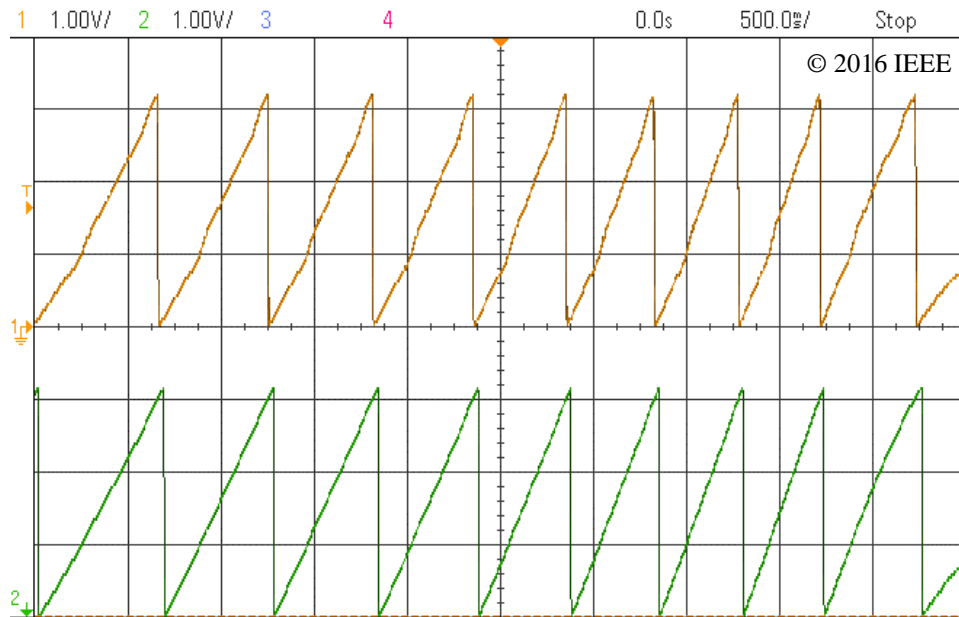
Figure 25 : Position [2 rad/div] measured using: Hall sensors and PLL (top), incremental encoder (bottom).

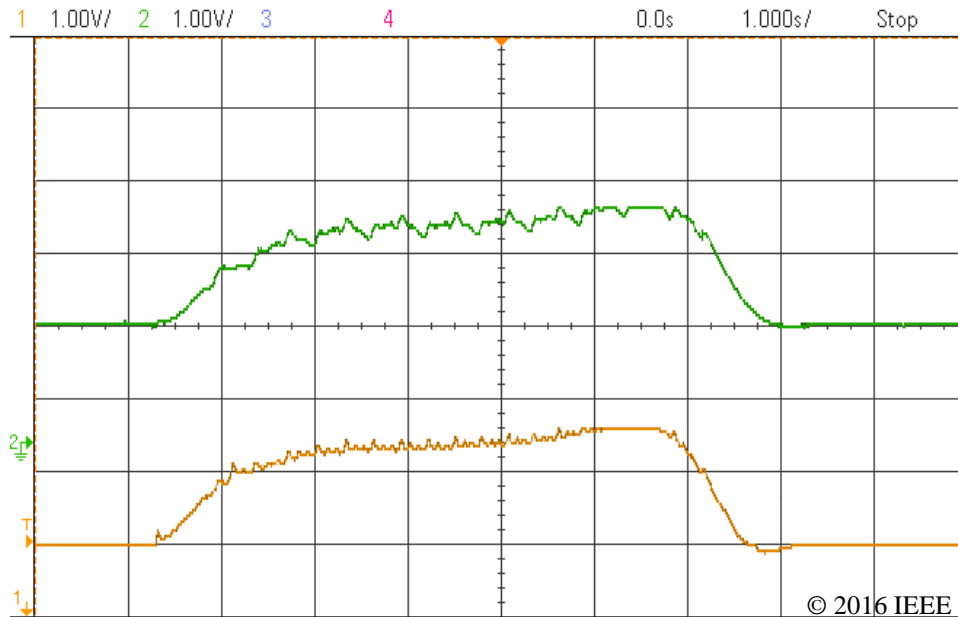**Figure 26 : Speed [50 (mm/s)/div] measured using: Hall sensors and PLL (top), incremental encoder (bottom).**

The motor was commanded to move a stroke of 400 mm. When the incremental encoder was used to close the loops, the motor took 5.8 seconds to arrive at the commanded position. Due to the small error in the estimation, the motor took 6.3 seconds when the Hall sensors were employed.

52

CHAPTER IV

THE DC SYSTEM

Conventionally, the motor and pump are placed downhole while the controller is on surface. Alternatively, an Integrated Drive-Motor (IDM) system could be used. In IDM systems, an electric motor is combined with a power electronic drive in a single enclosure.

Integrated Drive-Motor (IDM) shows promising advantages [26]-[27]. In IDM systems, an electric motor is combined with the VSC in a single enclosure downhole as shown in Figure 27.

Figure 27 : Conventional Integrated Drive-Motor system.
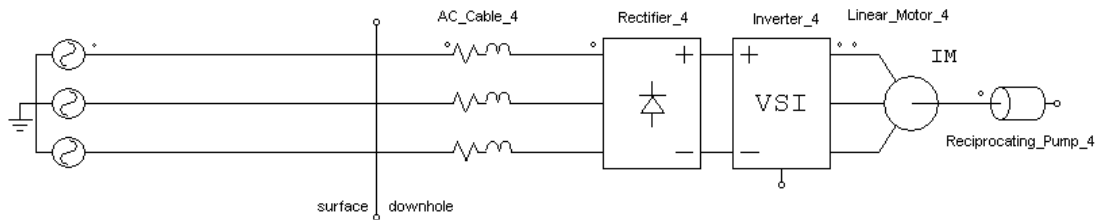

This chapter presents a modified IDM system which shows some advantages compared to the conventional IDM and discusses the variable speed control of the modified IDM. The experimental results are shown in Section IV.

This paper discuss the control system for the linear motor which drives the reciprocating pump. In this study, a permanent magnet synchronous motor (PMSM) is

used because of its higher efficiency and smaller physical size compared to induction motors [28]. The motor is desired to have variable speed and it is controlled in a vector control manner. The discussion is focused on the variable speed control system implementation.

4.1   Modified integrated drive-motor

In the conventional IDM, both the rectifier and inverter are placed with motor in the same package. The main advantage of this system is eliminating the problems associated with a long high frequency cable. In this configuration, the long cable has a line frequency of 60 Hz which will eliminate the effects of the controller high switching frequency on the cable [29]. However, the application of IDM in ESP requires special consideration because of the extreme depth at which they operate. The high temperature at these depths (200˚C or 400˚F) is a big challenge for implementation of conventional IGBT or MOSEFT motor drives. Nevertheless, wide bang gap devices such as SiC are perfect candidates because of their high temperature rating of ~300˚C [30]. The main challenge in this IDM system is the difficulty of communication between the surface and the drive. It requires a long separate signal cable or power-line communication system which adds to the system cost.

Figure 28 shows the modified IDM system where the rectifier is placed on the surface while the inverter is still integrated with the motor. This system has two main advantages compared to conventional IDM. First, the long power cable is DC instead of three phase AC. This will reduce the losses and the amount of the required copper and

eliminate the cable capacitance and cable impedance unbalance problems [31]. Second, the DC bus voltage could be used directly to control the speed of the pump as shown in the next section. Obviously, this will require a controlled rectifier such as PFC boost converter. Additionally, a multi-phase fault-tolerant system may be used without additional cables.
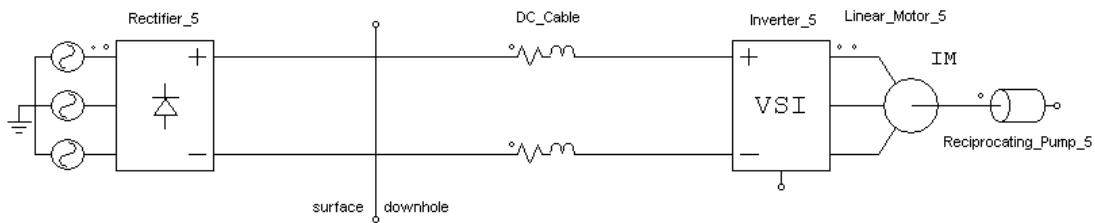

Figure 28 : Modified IDM system.

The speed control of this system may not be straight forward or cost efficient. Again, a long signal cable or power-line communication system is required to command speeds from the surface to the downhole motor. In the next section, a control method is presented which avoids the use of long signal cable or power-line communication system. The proposed control method only utilizes the DC bus voltage to control the motor speed.

4.2   Speed control of the downhole linear motor from the surface

If the motor is controlled using six-step method, the control system of the modified IDM system will be simple under variable DC bus voltage. However, the high

performance vector control was selected for this application. The DC bus voltage could be efficiently used to control the speed since lower voltage is required at lower speeds.

The first step which is performed by the surface controller is to select the appropriate DC bus voltage based on some desired reference speed ω*. Assuming the rated current Irated is required to be always available, the required phase voltage at the motor terminals Vp for a given reference speed is given by:

$$V_p = \sqrt{(R\,I_{rated} + \lambda_{pm}\,\omega^*)^2 + (\omega^*\,L\,I_{rated})^2} \qquad (\,40\,)$$

where R and L are the motor resistance and synchronous inductances respectively. λpm is the permanent magnet flux linkage. If the inverter utilizes Space Vector PWM, the minimum DC bus voltage Vdc required at the output of the rectifier to run the motor at this speed is,

$$V_{dc} = \sqrt{3}\,V_p + I_{dc}R_{cable} \qquad (\,41\,)$$

where $I_{dc}R_{cable}$ is the voltage drop across the DC cable.

The next step is done downhole where a voltage sensor is used to measure the DC bus voltage at the inverter input downhole. The sensor must be rated at the high downhole temperature. Then, the desired reference speed could be reverse calculated by solving equations (40) and (41) without the DC cable voltage drop term. Finally, the calculated reference speed is used as the maximum value of the output of the position controller in the vector control shown previously in Figure 16.

4.3 Experimental results

In order to perform an experimental test of the modified IDM system in lab environment, a DC regulated power supply was used to emulate the controlled rectifier. Since the transmission cable is DC, a distributed model or even a π model is not required and a resistor was used to model the cable. An encoder was used to provide the position of the linear motor. In order to load the linear motor, it was coupled to a generator.

The DC bus voltage was varied between 30V to 150V. The linear motor was commanded to travel a stroke of 65 cm back and forth. Because of this short stroke and limited motor force and thus acceleration, the maximum achievable speed was 25 cm/s. Figure 29 shows the motor operating at 150V, the maximum speed reference was 25 cm/s. For 90V operation, the speed reference was 15 cm/s as shown in Figure 30. Figure 31 shows the speed response when the DC bus voltage was set at 30V with reference speed of 5 cm/s.

In all three cases, the reference speed changes as the DC bus voltage changes and the actual speed follows the reference speed. However, the measured speed didn't match the command speed during acceleration. This is due to the mechanical time constant (mass and friction) of the motor despite the fact that the maximum available force was applied during acceleration. Moreover, Because of the short stroke length and limited motor current/force, the motor reaches its final position before the speed is able to settle down to the final value.
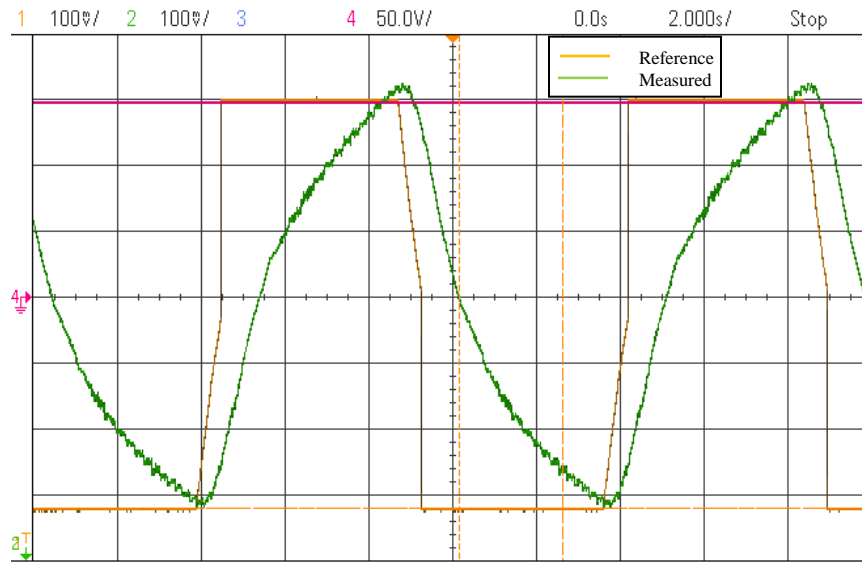
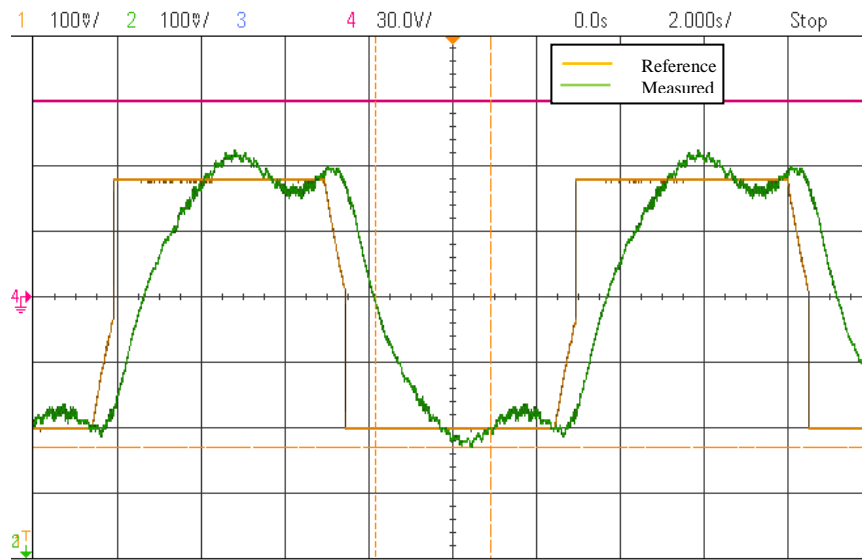**Figure 29 : Reference and measured speeds (8 cm/s /div) at 150V.**

Figure 30 : Reference and measured speeds (8 cm/s /div) at 90V.
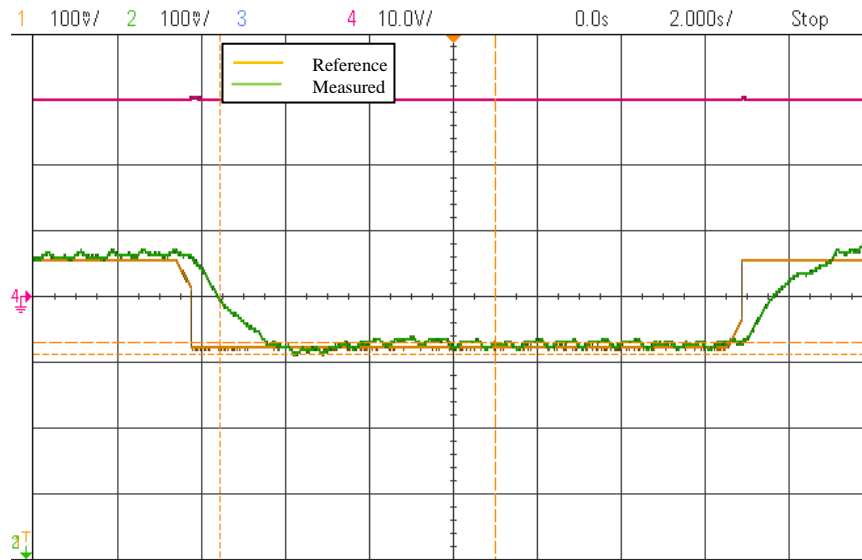
Figure 31 : Reference and measured speeds (8 cm/s /div) at 30V.

In this chapter, a control method for linear motor driving a reciprocating pump in a modified Integrated Drive-Motor (IDM) system was proposed. In this system, the rectifier was placed on the surface while the inverter was placed downhole with the motor. The DC bus voltage was used to control the speed of the pump without any additional signal cables. Experimental result showed that the proposed control method could be implemented for high performance applications.

CHAPTER V

SENSORLESS CONTROL

5.1   Sensorless control with short cable (DC system)

In this section, a complete position sensorless algorithm is presented. Since the model of a linear PM motor is similar to the rotating one, algorithms developed for rotating motors could be adopted for linear motors. However, it should be noted that in linear motion the ability to start from standstill under load and speed reversal are essential.

A sensorless control method was proposed for conventional Direct Torque Control (DTC) in [10], [12] to eliminate position sensors. DTC uses the speed feedback but does not require an accurate position feedback. The high-performance vector control requires a more precise and accurate position information.

The back-EMF could be considered as a disturbance to a linear system and estimated in an open loop manner as [24],

$$\hat{E}_{\alpha\beta} = V_{\alpha\beta} - (R + sL)I_{\alpha\beta} \qquad (42)$$

However, in this case the estimated back-EMF will be sensitive to the noise in the measurements and to parameter variations.

For this reason, a closed loop disturbance observer could be formed as shown in Figure 32 [32]. In this case, a current observer is used to estimate the line currents in the stationery reference frame. Then, the error between the estimated and measured current is fed back to a compensator K(s) where the output of this compensator is the estimated back-EMF $\hat{E}_{\alpha\beta}$ which is used again to estimate the current.
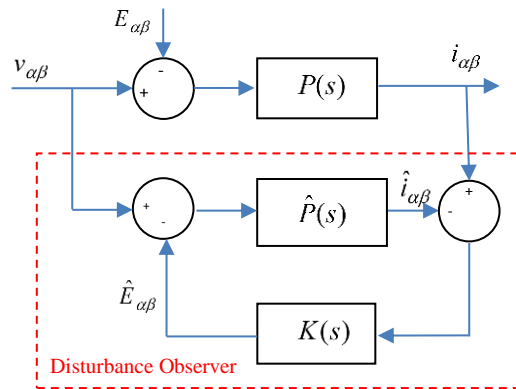
60

Figure 32 : Closed loop back-EMF estimation which utilizes a current observer.

Assuming the motor electrical parameters are accurately known, the system could be reduced to the system shown in Figure 33 and the transfer function between the estimated and actual back-EMF is,

$$\frac{\hat{E}_{\alpha\beta}}{E_{\alpha\beta}} = \frac{K(s)\,P(s)}{1 + K(s)\,P(s)} \qquad\qquad (\ 43 \ )$$
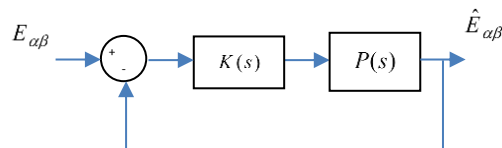

Figure 33 : Equivalent block diagram of the observer.

61

If a proportional compensator is used [33] to design the compensator K(s), it will result in a Luenberger observer and the transfer function is given by,

$$\frac{\hat{E}_{\alpha\beta}}{E_{\alpha\beta}} = \frac{K_p}{sL + (K_p + R)} \qquad (44)$$

Although this compensator is commonly used to estimate the back-EMF, clearly a proportional compensator is not enough to design for an acceptable response. Therefore, a PI compensator is used to form a PI Observer [34], [35]. A PI compensator results in the following transfer function,

$$\frac{\hat{E}_{\alpha\beta}}{E_{\alpha\beta}} = \frac{K_p s + K_i}{s^2 L + (K_p + R)s + K_i} \qquad (45)$$

Using (8), the observer gains were designed such that the observer bandwidth is the same as the current control loop.

The position of the flux is lagging 90° degrees behind the back-EMF vector. Therefore, it is important to know the direction of the EMF vector movement to identify the magnet polarity. This could be done by monitoring the rate of change of the back-EMF vector.

Using the back-EMF information derived from the observer, a PLL tracking observer is used to extract the position information from the back-EMF. From the estimated back-EMF and its direction, it is easy to drive the motor position using inverse tangent function.

However, the position derived from this method is usually too noisy to be employed in the closed loop system. Moreover, the speed calculation requires the derivative of this noisy signal to be computed which will amplify the noise.

62

Alternatively, the error in position is calculated and a PLL tracking observer is formed to compensate for this error. The algorithm starts from an arbitrary reference position and transforming the back-EMF to this reference frame. Assuming an estimated reference frame with a position $\hat{\theta}(t)$ as shown in Figure 34,
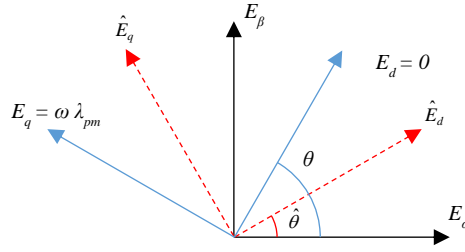

Figure 34 : Estimating the position error from the back EMF vector.

the error in position is defined as,

$$\theta_{err}(t) = \theta(t) - \hat{\theta}(t) \qquad (46)$$

Transforming the sine and cosine signals to the estimated reference frame will result in,

$$\begin{bmatrix} \hat{E}_d \\ \hat{E}_q \end{bmatrix} = \begin{bmatrix} \cos(\hat{\theta}) & \sin(\hat{\theta}) \\ -\sin(\hat{\theta}) & \cos(\hat{\theta}) \end{bmatrix} \begin{bmatrix} -\sin(\theta) \\ \cos(\theta) \end{bmatrix} \omega\,\lambda_{pm} = \begin{bmatrix} -\sin(\theta_{err}) \\ \cos(\theta_{err}) \end{bmatrix} \omega\,\lambda_{pm} \qquad (47)$$

63

Based on the values of the Back-EMF in the estimated reference frame, the error between the real and estimated position could be found. The error between the real and estimated position could be derived as,

$$\theta_{err}(t) \approx direction \times \sin^{-1}\left(\frac{-\hat{E}_d}{|\hat{E}|}\right) \qquad (48)$$

Or it could be approximated as:

$$\theta_{err}(t) \approx direction \times \frac{-\hat{E}_d}{|\hat{E}|} \qquad (49)$$

The direction of motion could be detected by taking the derivative of the inverse tangent function. It could be easily shown that,

$$\omega |E|^2 = E_\alpha \frac{d}{dt} E_\beta - E_\beta \frac{d}{dt} E_\alpha \qquad (50)$$

Based on the polarity of this term, the direction could be identified. High pass filters could be used in equation (50) to implement the derivatives to reduce the noise associated with pure derivatives.

Finally, a PI controller is designed to compensate for this error and obtain the position and speed information [24]. The output of this controller is the speed which could be integrated to get the position as shown in Figure 35.
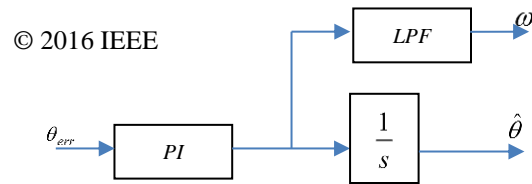
Figure 35 : Phase Locked Loop consists of a PI controller, an integrator and a low pass filter.

A dc bus along with a three phase IGBT inverter switching at 10 kHz were used to drive the three-phase tubular PM linear motor. The winding assembly was mounted to the base while the magnetic rod was allowed to slide and drive the load. The motor was loaded using a Trans-Rotary Magnetic Gear [25]. The load force was selected to be half of the rated continuous motor force. The voltage was compensated to correct the error caused by dead-time and voltage drop of the inverter [36]. The experimental setup used in this paper is shown in Figure 36.
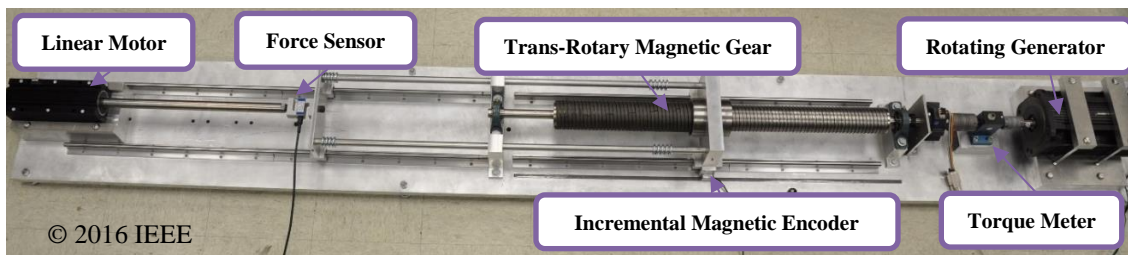

Figure 36 : Experimental setup including the linear motor, Trans-Rotary Magnetic Gear and rotating generator.

Four experiments were performed to evaluate the performance of the sensorless algorithm. First, the ability of the motor to start from zero speed was tested. Then, a speed reversal test was performed. Next, the minimum operation speed was evaluated. Finally, the operation under variable load force was examined.

In all experiments, the position and speed derived from the encoder were used to monitor the real values but were not utilized in the control. Only the sensorless derived speed and position are used to close the three control loops.

Figure 37 compares the position and speed derived from the encoder with the sensorless algorithm when starting from standstill. Since the position is unknown at standstill, the sensorless algorithm starts from some initial assumed position before it estimate and compensate for the error to get to the actual position.

At speed reversal, the sensorless algorithm fails to perfectly track the position however it was able to recover after a short delay. In Figure 38, the position and speed derived from encoder is compared to the sensorless.
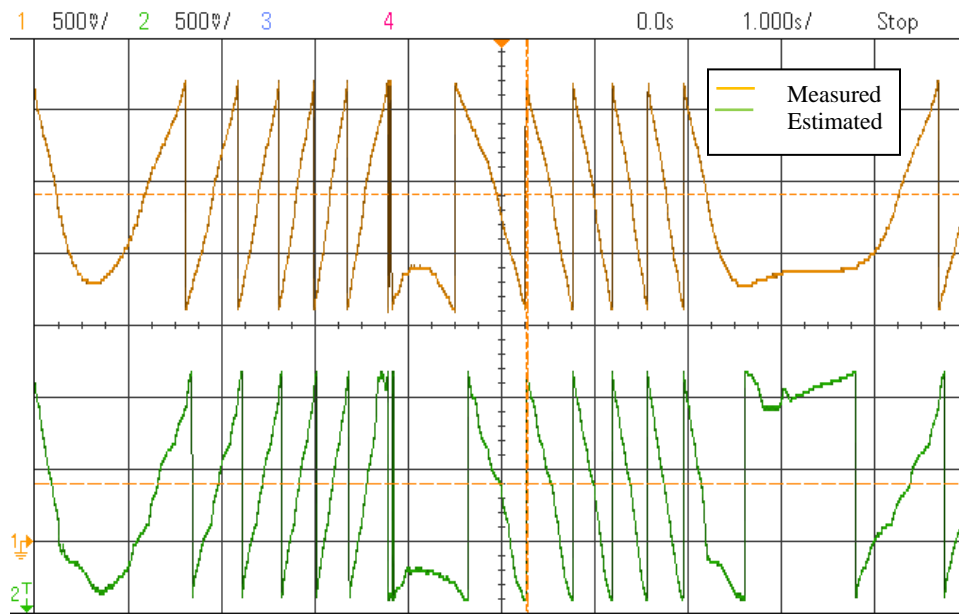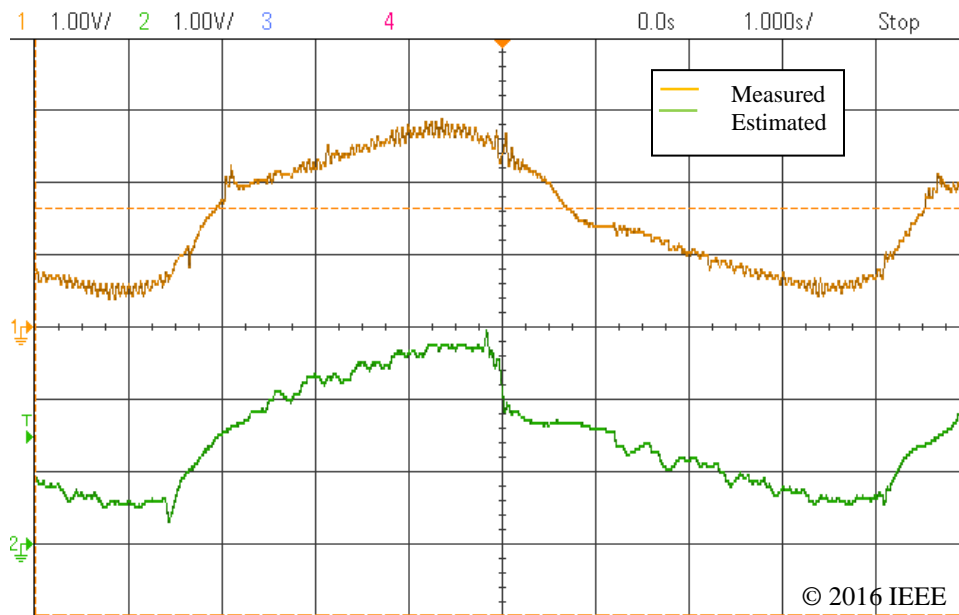
(a)

© 2016 IEEE
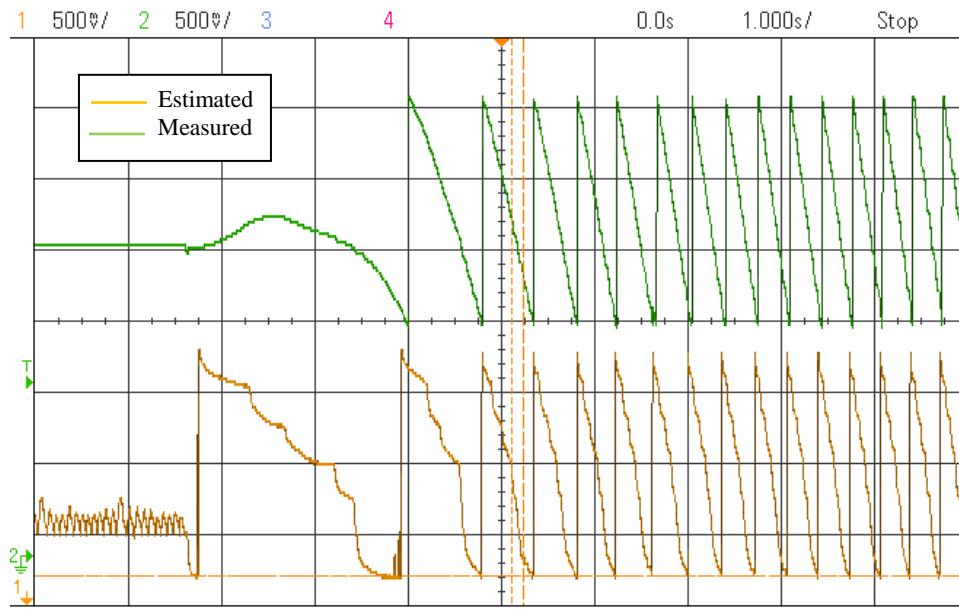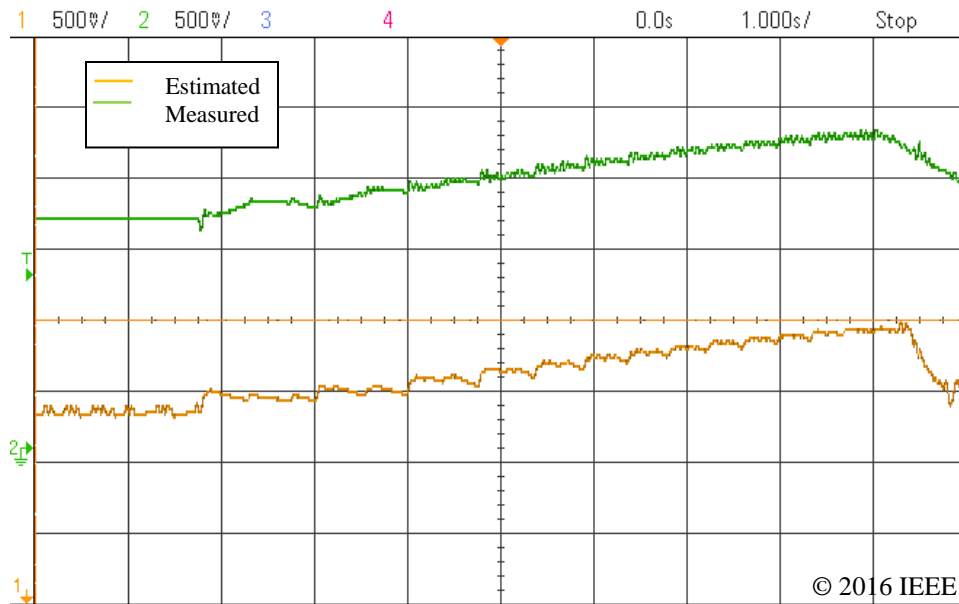
(b)

Figure 37 : Starting from zero speed test. (a) Position [2 rad/div] measured using encoder (top), sensorless (bottom). (b) Speed [50 (mm/s)/div] measured using encoder (top), sensorless (bottom).

Figure 38 : Speed reversal test. Position [2 rad/div] measured using encoder (top), sensorless (bottom). Speed [100 (mm/s)/div] measured using encoder (top), sensorless (bottom).

The motor was commanded to move a stroke of 250 mm. When the encoder was used to close the loops, the motor took 6.7 seconds to travel a full stroke back and forth. Due to the small error in the estimation, the motor took 7.5 seconds when the sensorless algorithm was employed.

Next, the minimum speed that the sensorless algorithm can operate was evaluated. As shown in Figure 39, the sensorless algorithm can operate at 1 Hz which is less than 1% of the rated speed.

Finally, the algorithm was tested under variable load force. A change in the load force was introduced and the estimated position is compared to the actual position of the linear motor in Figure 40. The sensorless algorithm was capable of keeping the linear motor in an acceptable operating condition.
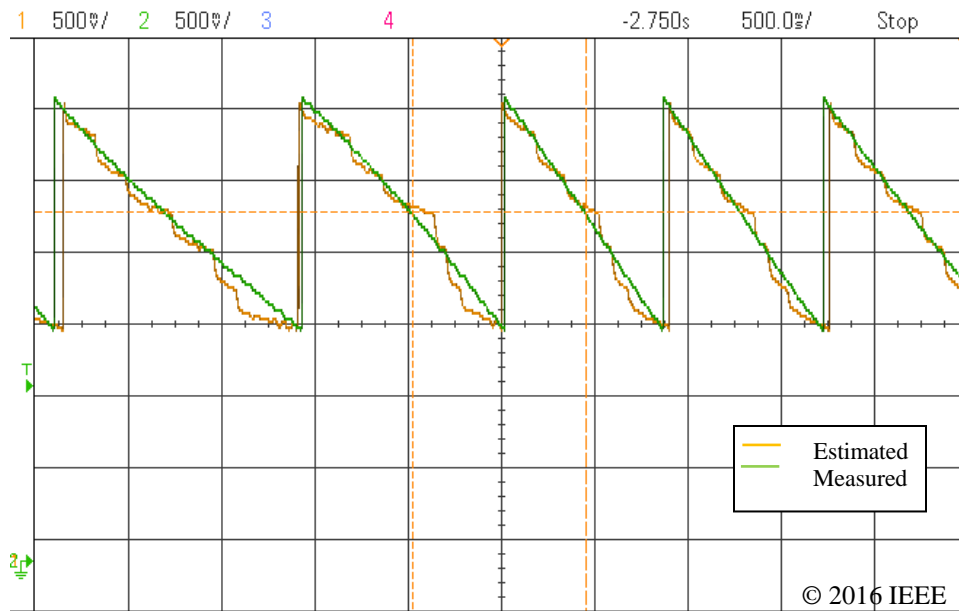
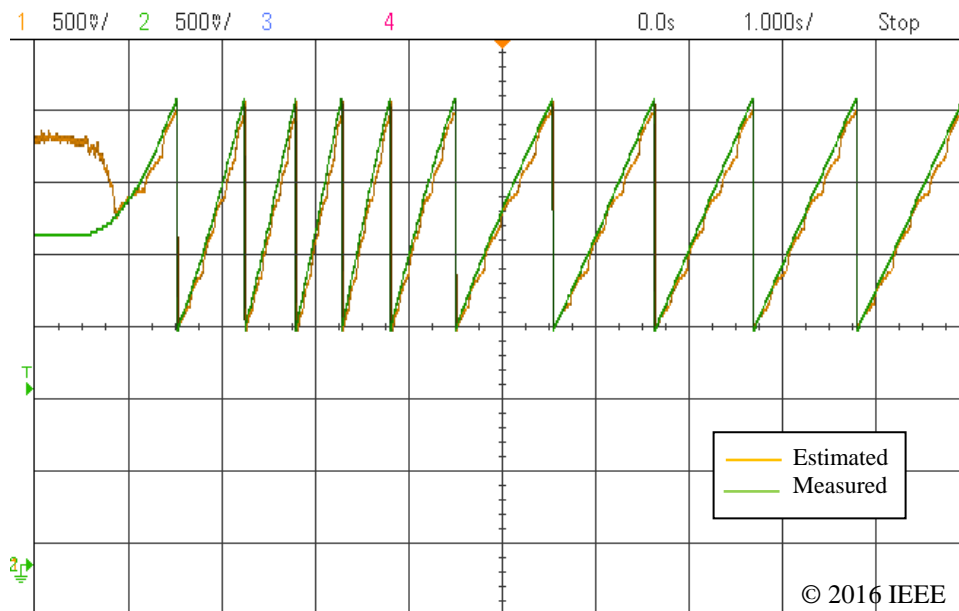**Figure 39 : Position [2 rad/div] comparison when the speed is limited to 1 Hz.**

Figure 40 : Position [2 rad/div] when load force changes.

70

In all these tests, the error between the actual position and estimated position was within 5 electrical degrees when the linear motor was operated at speeds above 4 Hz. When operated at extremely low speed of 1 Hz the error was within 30 electrical degrees. With this huge error the motor was still capable to drive the load but the force ripple was high.

5.2   Long cable modeling

5.2.1   Long cable parameters

To model a long cable properly the following effects can be taken into account

1) Self-resistance: accounts for the copper resistivity for a given cable geometry at a given temperature. Moreover, it includes the skin effect which is a result of the eddy currents induced by the magnetic field of the conductor current itself. The skin effect will reduces the effective cable cross section which increases the resistance.

2) Mutual-resistance: accounts for the skin effect resulted from the eddy currents induced by the magnetic field of the current of the other conductors.

3) Self-inductance: a measure of the voltage induced from the magnetic field produced by the conductor current itself.

4) Mutual-inductance: a measure of the induced voltage from the magnetic field produced by the other conductors.

5) Self-capacitance: a measure of the amount of electric charge on a conductor when it is at one volt while other conductors are grounded.

6) Mutual-capacitance: a measure of the amount of electric charge on a conductor when the other conductor is at one volt while other conductors are grounded.

7) Insulation resistance: a measure of the current leakeage through the insulation material.

In this study all the previous parameters were included except for the mutual resistance and the insulation resistance which were neglected.

5.2.2 Long cable parameters calculation

The cable resistance per unit length is calculated from the cable geometry as:

$$R_{ac} = \frac{\rho}{A}\left(1 + 0.00393(\text{T} - 20)\right) \tag{51}$$

where ρ is the copper resistivity at 20° C, T is the average operating Temperature and A is the conductor skin depth area given by:

$$A = \pi\delta(d - \delta) \tag{52}$$

where δ is the skin depth and d is the conductor diameter. The cable capacitance and inductance per unit length are derived from electrostatic and magneto-static finite element analysis (FEA) respectively. Figure 41 shows a cross section of the cable which consist of three copper conductors, conductor insulation, cable jacket and a steel armor. The inductance and capacitance matrices are defined as follows:

$$L = \begin{bmatrix} l_s & l_m & l_m \\ l_m & l_s & l_m \\ l_m & l_m & l_s \end{bmatrix} \tag{53}$$

$$C = \begin{bmatrix} c_s & c_m & c_m \\ c_m & c_s & c_m \\ c_m & c_m & c_s \end{bmatrix} \tag{54}$$

The self and mutual values of the inductances and capacitances were obtained from

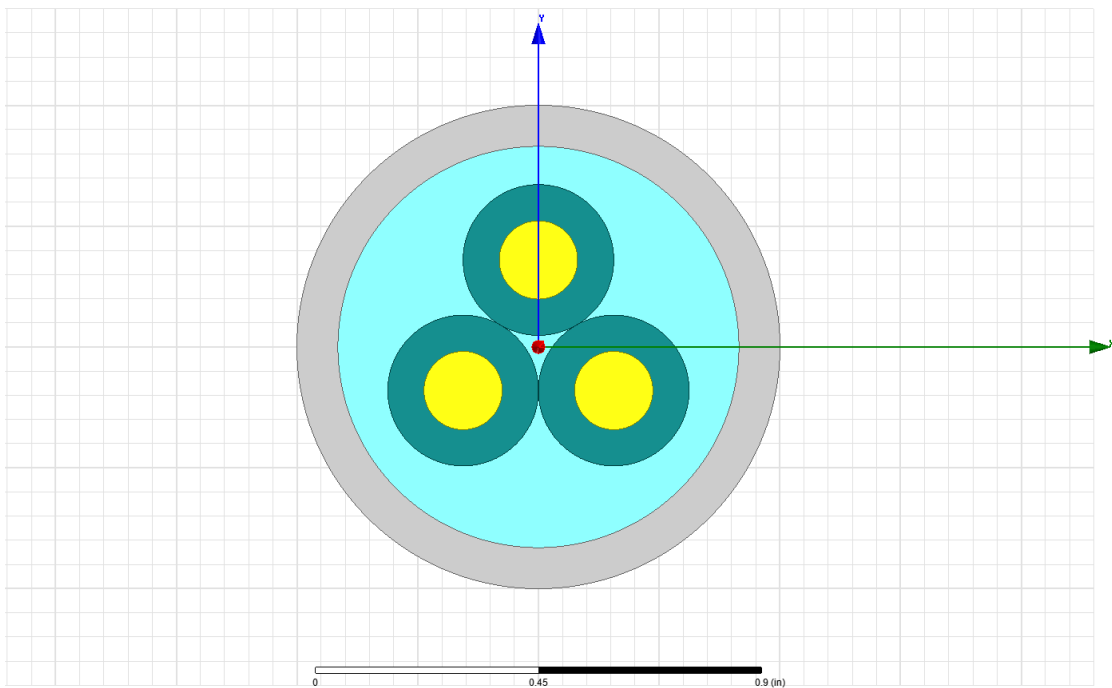the FEA as listed in Table 2. The mutual capacitance have a negative value as expected.

Figure 41 : Cable cross section.

Table 2 : Parameters of the 6km long AWG#6 cable.

Parameter	Symbol	Value	Units
Resistance	r	1.6531	Ohm/km
Self-Inductance	l_s	36.1	mH/km
Mutual Inductance	l_m	35.7	mH/km
Self-Capacitance	c_s	137.76	nF/km
Mutual Capacitance	c_m	-27.39	nF/km

The FEA calculate the self-capacitance c_s for a phase by applying a voltage potential at that phase while keeping the other two phases and the armor at zero potential. The mutual capacitance c_m is the capacitance between two conductors without considering other conductors.

Figure 42 shows the line to line capacitance c_l and line to ground capacitance c_g.
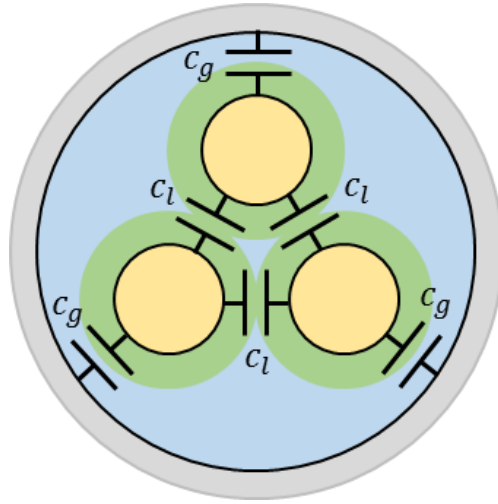
Figure 42 : Cable cross section showing the capacitances.

The self c_s and mutual c_m capacitances could be represented as the line to line capacitance c_l and line to ground capacitance c_g using:

$$c_l = -c_m \qquad (55)$$

$$c_g = c_s + 2\,c_m \qquad (56)$$

Another representation using the positive sequence c_1 and zero sequence c_0 capacitances could be written as:

$$c_1 = c_s - c_m = c_g + 3\,c_l = c \qquad (57)$$

$$c_0 = c_s + 2\,c_m = c_g \qquad (58)$$

One way to look at these capacitances is to transform the delta line to line capacitance c_l to a Y connected capacitance of three time the capacitance as shown in Figure 43 (a). Since the transformed capacitances are balanced and the ground

capacitances c_g are balanced too, the summation of the voltage differences between the phases and the armor is equal to the summation of the voltage differences between the phases and the center of the Y. This means that the two capacitances are in parallel and could be simply added as shown in Figure 43 (b).
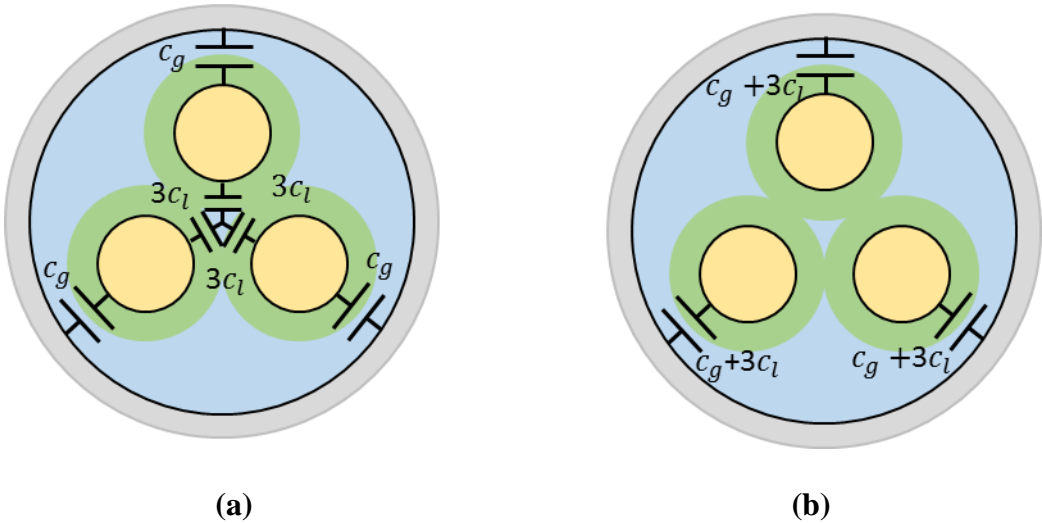

(a)   (b)

Figure 43 : Cable equivalent capacitance.

Moreover, since the summation of the three phase current is zero, the self and mutual inductances could be combined in one term as $l_s - l_m$. This could be shown by looking at the voltage induced by the magnetic fields of the current which could be written as:

$$\begin{bmatrix} V_a \\ V_b \\ V_c \end{bmatrix} = \begin{bmatrix} l_s & l_m & l_m \\ l_m & l_s & l_m \\ l_m & l_m & l_s \end{bmatrix} \frac{d}{dt} \begin{bmatrix} I_a \\ I_b \\ I_c \end{bmatrix} = (l_s - l_m) \frac{d}{dt} \begin{bmatrix} I_a \\ I_b \\ I_c \end{bmatrix} + \begin{bmatrix} l_m & l_m & l_m \\ l_m & l_m & l_m \\ l_m & l_m & l_m \end{bmatrix} \frac{d}{dt} \begin{bmatrix} I_a \\ I_b \\ I_c \end{bmatrix} \quad (59)$$

If the summation of the three currents is zero, the second term in equation (59) will be zero. The equivalent inductance per unit length is only the first term in equation (59) and could be defined as:

$$l = l_s - l_m \qquad (60)$$

Table 3 lists the equivalent parameters of the cable.

Table 3 : Equivalent parameters of the cable.

Parameter	Symbol	Value	Unit
Resistance	r	1.6531	Ohm/km
Inductance	$l = l_s - l_m$	0.381	mH/km
Capacitance	$c = c_s - c_m$	165.1	nF/km
Length	L	6	km

5.2.3 Cable distributed model

The distributed per phase model of the cable shown in Figure 44, could be written in the ABCD matrix form as:
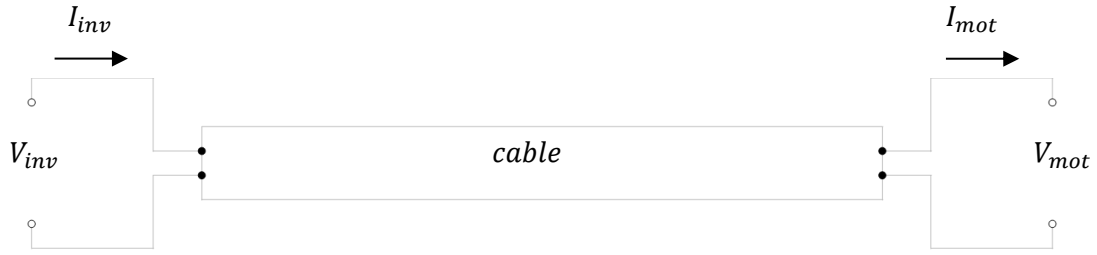
Figure 44 : Long cable connecting the inverter to the motor.

$$\begin{bmatrix} V_{inv} \\ I_{inv} \end{bmatrix} = \begin{bmatrix} \cosh(\gamma L) & Z_c \sinh(\gamma L) \\ \dfrac{1}{Z_c} \sinh(\gamma L) & \cosh(\gamma L) \end{bmatrix} \begin{bmatrix} V_{mot} \\ I_{mot} \end{bmatrix}$$ (61)

where V_{inv}, I_{inv}, V_{mot} and I_{mot} are the inverter and motor side voltages and currents respectively. γ is the propagation constant defined as:

$$\gamma = \sqrt{(r + j\omega l)\,(j\omega c)}$$ (62)

Z_c is the characteristic impedance defined as:

$$Z_c = \sqrt{\dfrac{r + j\omega l}{j\omega c}}$$ (63)

The propagation constant γ could be written as:

$$\gamma = \alpha + j\beta$$ (64)

where α is the attenuation constant given by:

$$\alpha = \sqrt{\dfrac{(\omega c)}{2} (|z| - \omega l)}$$ (65)

and β is the phase constant given by

78

$$\beta = \sqrt{\frac{(\omega c)}{2}(|z| + \omega l)}$$

where $|z|$ is the magnitude of the impedance per unit length given by:

$$|z| = \sqrt{r^2 + (\omega l)^2}$$

Then the characteristic impedance Z_c could be written as:

$$Z_c = \frac{1}{\omega c}(\beta - j\alpha)$$

(67)

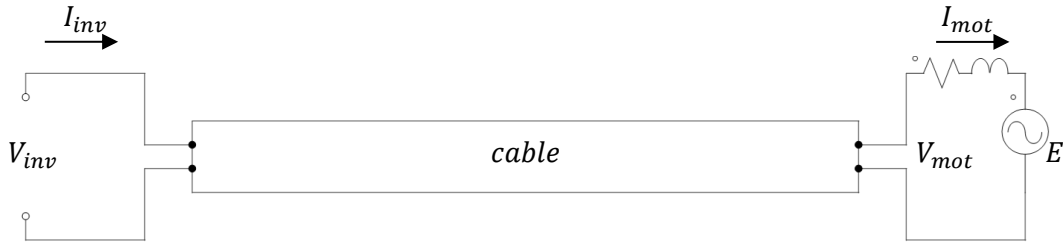If the motor is modeled as lumped resistance, inductance and back EMF terms as shown in Figure 45.

Figure 45 : Cable and motor model.

Then the ABCD matric for the motor could be written as:

$$\begin{bmatrix} V_{mot} \\ I_{mot} \end{bmatrix} = \begin{bmatrix} 1 & Z_l \\ 0 & 1 \end{bmatrix} \begin{bmatrix} E \\ I_{mot} \end{bmatrix}$$

(68)

where Z_l is the motor impedance given by,

$$Z_l = R_m + j\omega L_m \qquad\qquad (69)$$

Equations (61) and (68) could be used to combine the cable and motor model

as:

$$\begin{bmatrix} V_{inv} \\ I_{inv} \end{bmatrix} = \begin{bmatrix} \cosh(\gamma L) & Z_c \sinh(\gamma L) + Z_l \cosh(\gamma L) \\ \dfrac{1}{Z_c} \sinh(\gamma L) & \cosh(\gamma L) + \dfrac{Z_l}{Z_c} \sinh(\gamma L) \end{bmatrix} \begin{bmatrix} V_{mot} \\ I_{mot} \end{bmatrix} \qquad (70)$$

Then the input admittance which is the inverse of the input impedance could be

written as:

$$Y_{in} = \frac{1}{Z_{in}} = \frac{I_{inv}}{V_{inv}} = \frac{1}{Z_c}\frac{Z_c \cosh(\gamma L) + Z_l \sinh(\gamma L)}{Z_c \sinh(\gamma L) + Z_l \cosh(\gamma L)} \qquad (71)$$

Or it could be rewritten as:

$$Y_{in} = \frac{1}{Z_{in}} = \frac{I_{inv}}{V_{inv}} = \frac{1}{Z_c}\frac{1 - \Gamma e^{-2\gamma L}}{1 + \Gamma e^{-2\gamma L}} \qquad (72)$$

where Γ is the reflection coefficient defined as:

$$\Gamma = \frac{Z_l - Z_c}{Z_l + Z_c} \qquad\qquad (73)$$

5.2.4   Three phase cable T-model

Although these parameters are distributed along the cable length, a lumped

parameter model can be developed in order to test the system in lab environment. The

cable length is divided into two equal parts. Each half is modeled as having half the cable

resistance and inductances. All the cable capacitances are placed at the middle point. V_{mid}

is defined as the voltage of the middle point. The cable is modeled as a single section T-

model as shown in Figure 46.
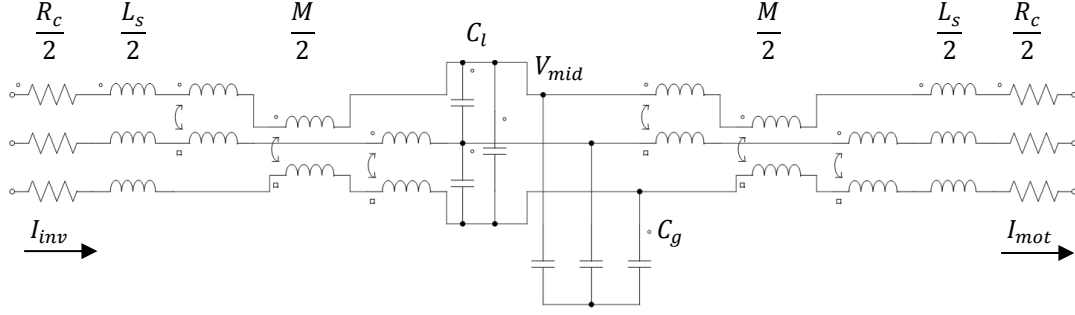
Figure 46 : Three phase T section cable model.

where R_c is the total cable resistance in Ω, L_s is the cable self-inductance in H, M is the cable mutual-inductance in H, C_l is the line-to-line capacitance in F and C_g is the line-to-armor capacitance in F.

In Figure 46, the neutral points at the motor and inverter sides are floating. This means that the summation of the three phase current is zero:

$$I_{a,inv} + I_{b,inv} + I_{c,inv} = 0 \qquad (74)$$

$$I_{a,mot} + I_{b,mot} + I_{c,mot} = 0 \qquad (75)$$

The voltage drop from the inverter side to the motor side for the three phases could be written as:

$$\frac{R_c}{2}\begin{bmatrix} I_{a,inv} \\ I_{b,inv} \\ I_{c,inv} \end{bmatrix} + \frac{1}{2}\begin{bmatrix} L_s & M & M \\ M & L_s & M \\ M & M & L_s \end{bmatrix}\frac{d}{dt}\begin{bmatrix} I_{a,inv} \\ I_{b,inv} \\ I_{c,inv} \end{bmatrix} + \frac{R_c}{2}\begin{bmatrix} I_{a,mot} \\ I_{b,mot} \\ I_{c,mot} \end{bmatrix} + \frac{1}{2}\begin{bmatrix} L_s & M & M \\ M & L_s & M \\ M & M & L_s \end{bmatrix}\frac{d}{dt}\begin{bmatrix} I_{a,mot} \\ I_{b,mot} \\ I_{c,mot} \end{bmatrix} \qquad (76)$$

Since the summation of currents on both sides is zero, equation (76) could be written as:

$$\frac{R_c}{2}\begin{bmatrix}I_{a,inv}\\I_{b,inv}\\I_{c,inv}\end{bmatrix}+\frac{1}{2}L_c\frac{d}{dt}\begin{bmatrix}I_{a,inv}\\I_{b,inv}\\I_{c,inv}\end{bmatrix}+\frac{R_c}{2}\begin{bmatrix}I_{a,mot}\\I_{b,mot}\\I_{c,mot}\end{bmatrix}+\frac{1}{2}L_c\frac{d}{dt}\begin{bmatrix}I_{a,mot}\\I_{b,mot}\\I_{c,mot}\end{bmatrix} \qquad (77)$$

where L_c is the cable synchronous inductance defined as:

$$L_c = L_s - M \qquad (78)$$

Moreover, the capacitance could be combined in one term as discussed previously

as:

$$C = C_g + 3\,C_l \qquad (79)$$

Figure 47 shows the reduced model.
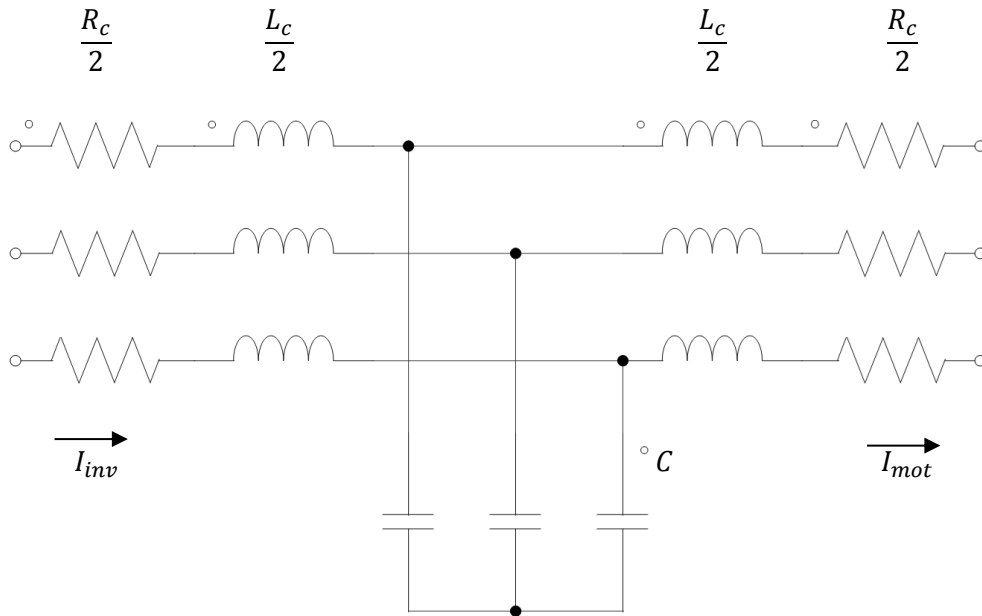
Figure 47 : Reduced three phase T section cable model.

For a given system frequency ω_1, the exact T-model parameters could be derived.

First, the characteristic impedance and propagation constant are defined as:

$$\gamma_1 = \sqrt{(r + j\omega_1 l)\,(j\omega_1 c)} = \alpha + j\beta \qquad (\,80\,)$$

$$Z_{c1} = \sqrt{\frac{r + j\omega_1 l}{j\omega_1 c}} \qquad (\,81\,)$$

Then, the system impedance and admittance are defined as:

$$Z \;=\; 2\,Z_{c1}\,tanh\left(\gamma_1 \frac{L}{2}\right) = R + jX \qquad (\,82\,)$$

$$Y \;=\; \frac{1}{Z_{c1}}\,sinh(\gamma_1\,L) = G + jB \qquad (\,83\,)$$

Or it could be expanded as:

$$R = \frac{2}{\omega c}\,\frac{\beta\,sinh(\alpha L) + \alpha\,sin(\beta L)}{cosh(\alpha L) + cos(\beta L)} \qquad (\,84\,)$$

$$X = \frac{2}{\omega c}\,\frac{\beta\,sin(\beta L) - \alpha\,sinh(\alpha L)}{cosh(\alpha L) + cos(\beta L)} \qquad (\,85\,)$$

$$G = \frac{\beta\,sinh(\alpha L)\,cos(\beta L) - \alpha\,cosh(\alpha L)\,sin(\beta L)}{\sqrt{r^2 + (\omega l)^2}} \qquad (\,86\,)$$

$$B = \frac{\alpha\,sinh(\alpha L)\,cos(\beta L) + \beta\,cosh(\alpha L)\,sin(\beta L)}{\sqrt{r^2 + (\omega l)^2}} \qquad (\,87\,)$$

Finally, the exact T-model parameters are derived as:

$$\begin{aligned} R_c &= R \\ L_c &= \frac{X}{\omega_1} \\ C &= \frac{B}{\omega_1} \end{aligned} \qquad (\,88\,)$$

From equations (84) to (87) it is clear that these parameters are frequency dependent. In the T model, these parameters are evaluated at a single frequency only. This

83

is why this model is exact at a single frequency only. Figure 48 shows the calculated resistance, inductance and capacitance for various cable gauges.
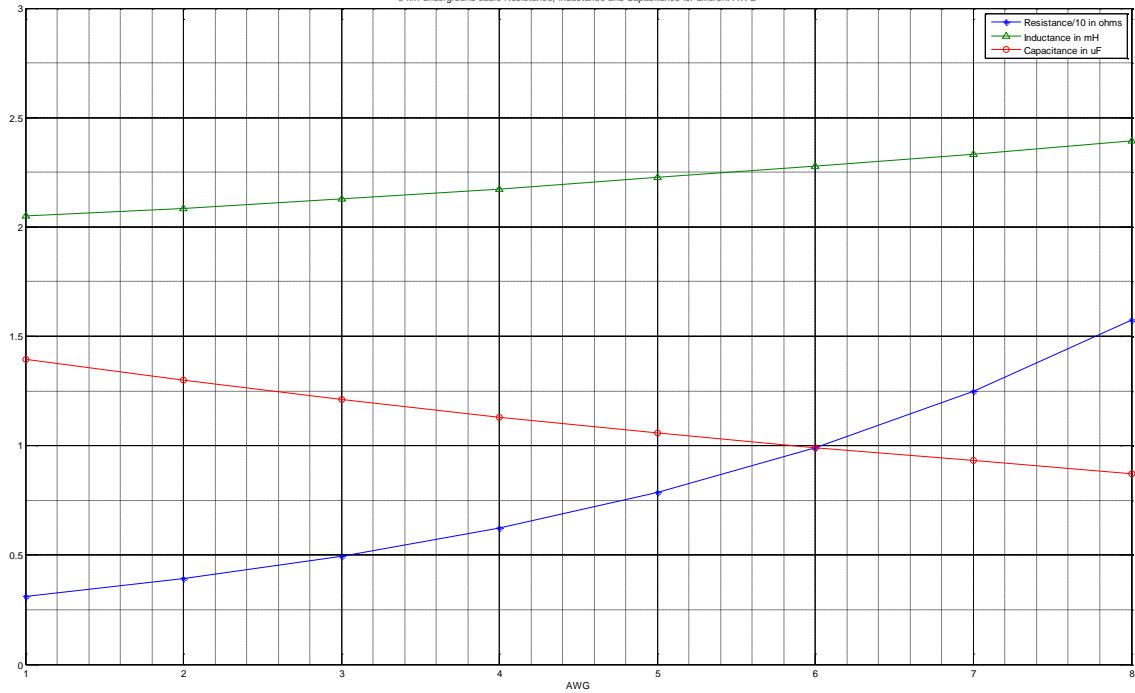
Figure 48 : 6 km underground cable Resistance, Inductance and Capacitance for different AWG.

5.2.5   *Per phase T-model*

The complete three phase system model including the motor and the inverter is shown in Figure 49.
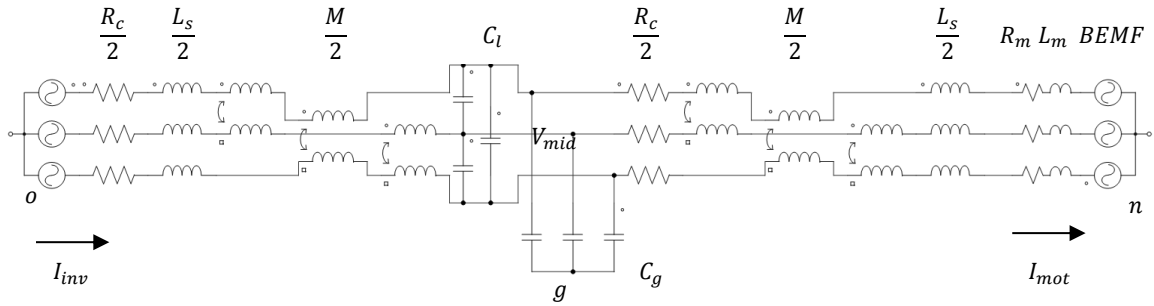
Figure 49 : Three phase T section system model.

where R_m is the motor resistance, L_m is the motor synchronous inductance and $BEMF$ is the motor back EMF. From the figure and using Kirchhoff's Voltage Law (KVL), the equations could be written as:

$$\begin{bmatrix} V_{ao} \\ V_{bo} \\ V_{co} \end{bmatrix} = \frac{R_c}{2}\begin{bmatrix} I_{a,inv} \\ I_{b,inv} \\ I_{c,inv} \end{bmatrix} + \frac{1}{2}\begin{bmatrix} L_s & M & M \\ M & L_s & M \\ M & M & L_s \end{bmatrix}\frac{d}{dt}\begin{bmatrix} I_{a,inv} \\ I_{b,inv} \\ I_{c,inv} \end{bmatrix} + \begin{bmatrix} V_{a,mid} \\ V_{b,mid} \\ V_{c,mid} \end{bmatrix} + \begin{bmatrix} V_{go} \\ V_{go} \\ V_{go} \end{bmatrix} \qquad (89)$$

$$\begin{bmatrix} E_a \\ E_b \\ E_c \end{bmatrix} = -\left(R_m + \frac{R_c}{2}\right)\begin{bmatrix} I_{a,mot} \\ I_{b,mot} \\ I_{c,mot} \end{bmatrix} - \left(L_m + \frac{1}{2}\begin{bmatrix} L_s & M & M \\ M & L_s & M \\ M & M & L_s \end{bmatrix}\right)\frac{d}{dt}\begin{bmatrix} I_{a,mot} \\ I_{b,mot} \\ I_{c,mot} \end{bmatrix} + \begin{bmatrix} V_{a,mid} \\ V_{b,mid} \\ V_{c,mid} \end{bmatrix} + \begin{bmatrix} V_{gn} \\ V_{gn} \\ V_{gn} \end{bmatrix} \qquad (90)$$

Using Kirchhoff's Current Law (KCL),

$$\begin{bmatrix} C_g + 2C_l & -C_l & -C_l \\ -C_l & C_g + 2C_l & -C_l \\ -C_l & -C_l & C_g + 2C_l \end{bmatrix}\frac{d}{dt}\begin{bmatrix} V_{a,mid} \\ V_{b,mid} \\ V_{c,mid} \end{bmatrix} = \begin{bmatrix} I_{a,inv} \\ I_{b,inv} \\ I_{c,inv} \end{bmatrix} - \begin{bmatrix} I_{a,mot} \\ I_{b,mot} \\ I_{c,mot} \end{bmatrix} \qquad (91)$$

Equation (91) could be rewritten as:

$$\begin{bmatrix} C_s & C_m & C_m \\ C_m & C_s & C_m \\ C_m & C_m & C_s \end{bmatrix}\frac{d}{dt}\begin{bmatrix} V_{a,mid} \\ V_{b,mid} \\ V_{c,mid} \end{bmatrix} = \begin{bmatrix} I_{a,inv} \\ I_{b,inv} \\ I_{c,inv} \end{bmatrix} - \begin{bmatrix} I_{a,mot} \\ I_{b,mot} \\ I_{c,mot} \end{bmatrix} \qquad (92)$$

A transformation from abc frame to $\alpha\beta0$ frame is defined using the following transformation matrix:

$$T = \frac{2}{3}\begin{bmatrix} 1 & -\frac{1}{2} & -\frac{1}{2} \\ 0 & \frac{\sqrt{3}}{2} & -\frac{\sqrt{3}}{2} \\ \frac{1}{2} & \frac{1}{2} & \frac{1}{2} \end{bmatrix} \quad\quad (93)$$

where

$$\begin{bmatrix} V_{\alpha o} \\ V_{\beta o} \\ V_{0o} \end{bmatrix} = T \begin{bmatrix} V_{ao} \\ V_{bo} \\ V_{co} \end{bmatrix} \quad\quad (94)$$

By adding the rows in equation (89) and (90) and noting that the summation of the current is zero results in:

$$V_{go} = \frac{V_{ao} + V_{bo} + V_{co}}{3} = V_{0o} \quad and \quad V_{gn} = 0 \quad\quad (95)$$

Applying the transformation to equations (89), (90) and (92) results in:

$$\begin{bmatrix} V_{\alpha o} \\ V_{\beta o} \\ V_{0o} \end{bmatrix} = \frac{R_C}{2}\begin{bmatrix} I_{\alpha,inv} \\ I_{\beta,inv} \\ I_{0,inv} \end{bmatrix} + \frac{1}{2}\begin{bmatrix} L_s - M & 0 & 0 \\ 0 & L_s - M & 0 \\ 0 & 0 & L_s + 2M \end{bmatrix}\frac{d}{dt}\begin{bmatrix} I_{\alpha,inv} \\ I_{\beta,inv} \\ I_{0,inv} \end{bmatrix} + \begin{bmatrix} V_{\alpha,mid} \\ V_{\beta,mid} \\ V_{0,mid} \end{bmatrix} + \begin{bmatrix} 0 \\ 0 \\ V_{0o} \end{bmatrix}$$

$$\begin{bmatrix} E_{\alpha} \\ E_{\beta} \\ E_0 \end{bmatrix} = -\left(R_m + \frac{R_c}{2}\right)\begin{bmatrix} I_{\alpha,mot} \\ I_{\beta,mot} \\ I_{0,mot} \end{bmatrix} - \left(L_m + \frac{1}{2}\begin{bmatrix} L_s - M & 0 & 0 \\ 0 & L_s - M & 0 \\ 0 & 0 & L_s + 2M \end{bmatrix}\right)\frac{d}{dt}\begin{bmatrix} I_{\alpha,mot} \\ I_{\beta,mot} \\ I_{0,mot} \end{bmatrix} + \begin{bmatrix} V_{\alpha,mid} \\ V_{\beta,mid} \\ V_{0,mid} \end{bmatrix}$$

$$\begin{bmatrix} C_s - C_m & 0 & 0 \\ 0 & C_s - C_m & 0 \\ 0 & 0 & C_s + 2C_m \end{bmatrix}\frac{d}{dt}\begin{bmatrix} V_{\alpha,mid} \\ V_{\beta,mid} \\ V_{0,mid} \end{bmatrix} = \begin{bmatrix} I_{\alpha,inv} \\ I_{\beta,inv} \\ I_{0,inv} \end{bmatrix} - \begin{bmatrix} I_{\alpha,mot} \\ I_{\beta,mot} \\ I_{0,mot} \end{bmatrix} \quad\quad (96)$$

These are three decoupled equations from which a per-phase model could be derived. For example, the equations for α phase in the previous equation could be rewritten as:

$$\frac{d}{dt}\begin{bmatrix} I_{\alpha,inv} \\ I_{\alpha,mot} \\ V_{\alpha,mid} \end{bmatrix} = \begin{bmatrix} -\frac{R_c}{L_c} & 0 & \frac{2}{L_c} \\ 0 & -\frac{R_m + \frac{R_c}{2}}{L_m + \frac{L_c}{2}} & \frac{1}{L_m + \frac{L_c}{2}} \\ \frac{1}{C} & -\frac{1}{C} & 0 \end{bmatrix}\begin{bmatrix} I_{\alpha,inv} \\ I_{\alpha,mot} \\ V_{\alpha,mid} \end{bmatrix} + \begin{bmatrix} \frac{2}{L_c} & 0 \\ 0 & -\frac{1}{L_m + \frac{L_c}{2}} \\ 0 & 0 \end{bmatrix}\begin{bmatrix} V_{\alpha o} \\ E_\alpha \end{bmatrix} \quad (\,97\,)$$

where L_c is:

$$L_c = L_s - M \quad (\,98\,)$$

and the capacitance C is:

$$C = C_g + 3\,C_l = C_s - C_m \quad (\,99\,)$$

The equations for β phase could be written in the same manner. Phase 0 could be neglected since $I_{0,inv}, I_{0,mot}$ and E_0 are all zero. Figure 50 shows a per phase model:
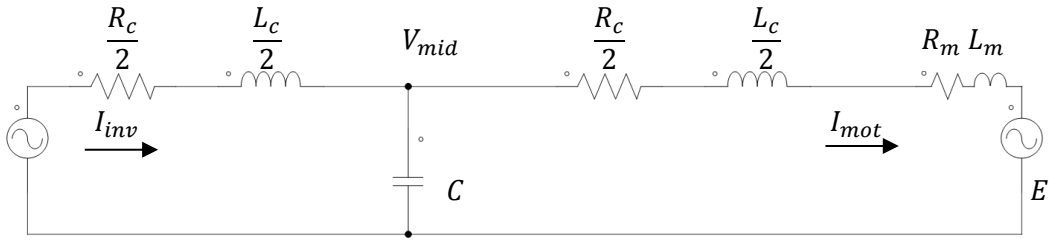
Figure 50 : Per phase T section cable model.

At a given frequency ω_1, the parameters R_c, L_c and C could be calculate from equations (80) to (88). The RLC parameters where calculated at two different frequencies of 10 and 20 k rad/s. The input admittance transfer function of the T-model in both cases was plotted and compared with the distributed model as shown in Figure 51. It is clear that these models give in the exact result only at the design frequency and deviate at other frequencies.
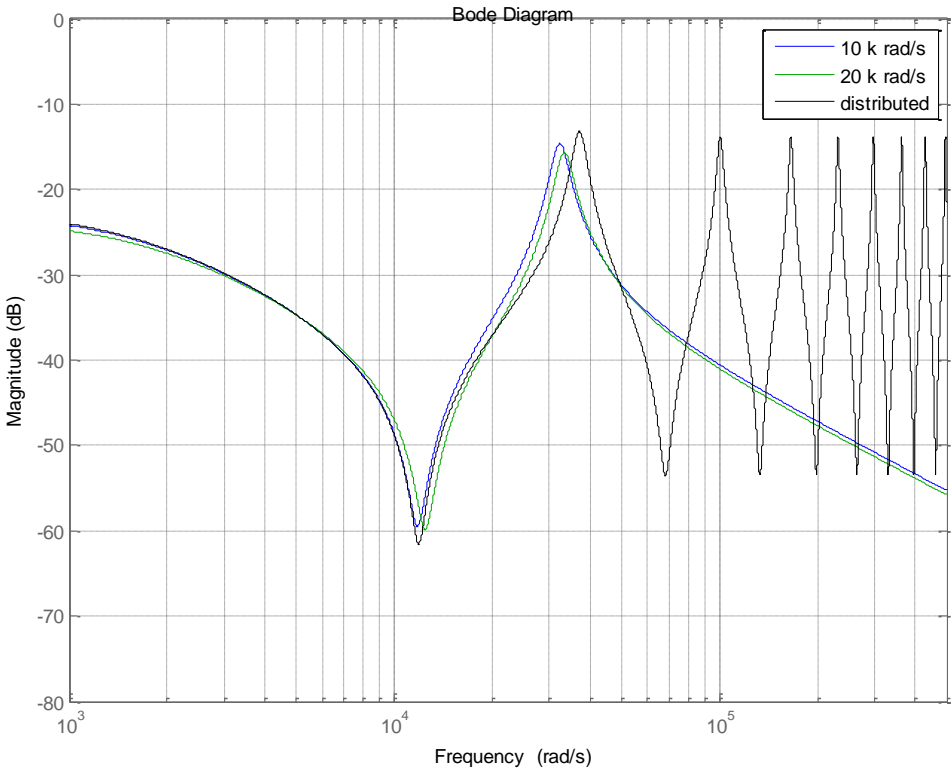
Figure 51 : T-model at 10 and 20 k rad/s compared with the distributed model.

5.2.6   *Multiple segment T-model*

Compared to distributed model, the accuracy of the lumped parameter T-model will degrade at higher frequencies. One way to improve the accuracy is to divide the cable into more than one T-model section [37].

For example, the cable was divided into 20 segments and compared to the single segment case discussed previously. The frequency response of this 20-segment model which is a 41st order model is shown in Figure 52 along with the 1-segment 3rd order model. In the figure, the input to the system is the inverter voltage and the output is the inverter current. It is clear from the figure that the 1-segment model matches the 20-segment model at low frequencies but not at high frequencies.
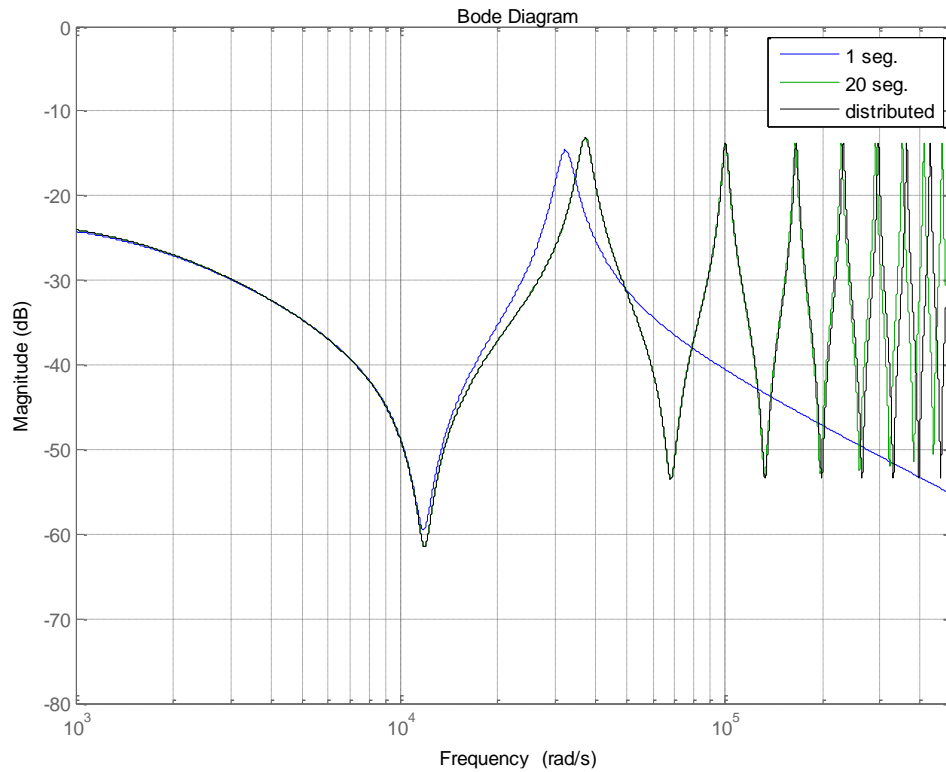
Figure 52 : Bode plot of the 1-segment and 20-segment models.

Although the 20 segment model will result in an accurate representation of the cable, it is difficult to implement a high order model in a real time system. The increase of the number of segments will improve the model accuracy but will increase the system complexity. For instance, A 1-Segment model is a third order model while a 2-segment model will result in a fifth order model. In general the model order n is related to the number of segments as:

$$n = 2 \times Segments + 1$$

(100)

Figure 53 adds the frequency response of the 2, 5 and 10-segment models to the previous figure.
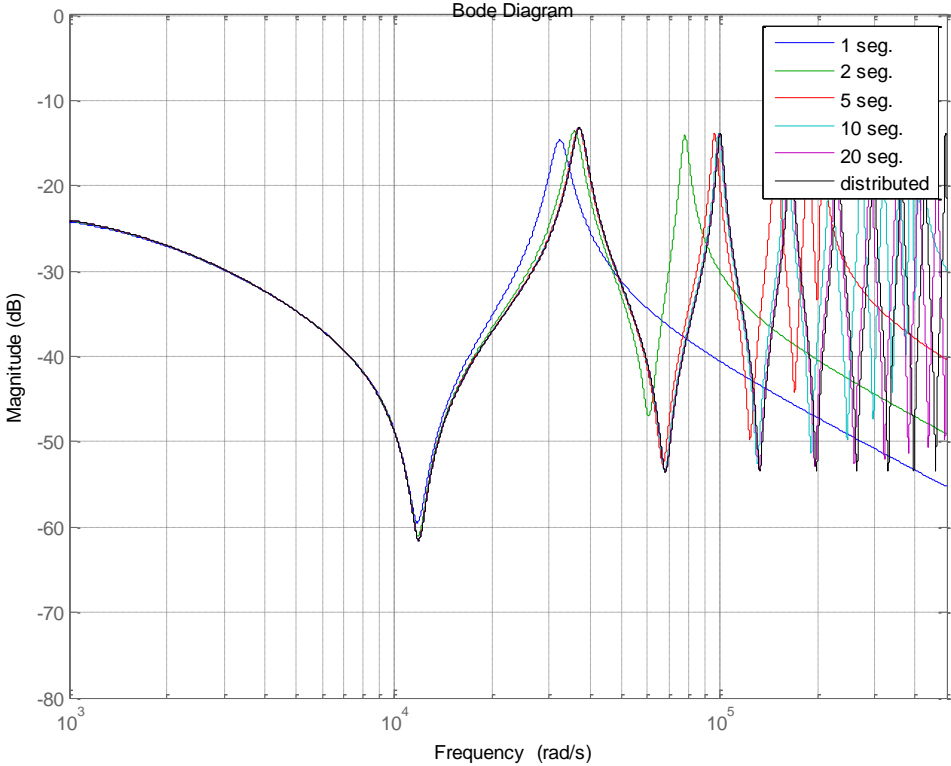
Figure 53 : System transfer function Iinv/Vinv when cable is divided into different number of segments.

To model the cable with enough accuracy without complexity, it is important evaluate the minimum number of segments required to accurately model the cable at and below a given frequency.

The lumped parameter model is considered accurate for electrically short cable. Electrically short means that the cable length is short enough compared to the wavelength. The wavelength is defined as:

$$\lambda = \frac{v}{f} = \frac{2\pi}{\beta} \qquad (101)$$

where β is the phase constant given by:

$$\beta = \sqrt{\frac{(\omega c)}{2}\left(\sqrt{r^2 + (\omega l)^2} + \omega l\right)} \qquad (102)$$

For higher frequencies, since $r \ll \omega l$ the phase constant could be reduced to:

$$\beta = \omega\sqrt{l\,c} \qquad (103)$$

and the wavelength:

$$\lambda = \frac{1}{f\sqrt{l\,c}} \qquad (104)$$

Defining electrically short cable to have a wavelength of at least eight times its length:

$$\lambda_{min} = 8 \times Length \qquad (105)$$

Then, the maximum frequency to keep a given cable electrically short could be written as:

$$f_{max} = \frac{1}{8 \times Length \times \sqrt{l\,c}} \qquad (106)$$

Generally, the number of segments N required at a given frequency f is:

$$N = \frac{cable\ length}{section\ length} = \frac{Length}{\lambda/8} = \frac{8}{2\pi} \times Length \times \beta(\omega) \qquad (107)$$

Or it could be approximated for high frequencies as:

$$N = 8 \times f \times \sqrt{L_c C} \qquad (108)$$

where L_c is the cable equivalent inductance and C is the cable equivalent capacitance. In this application, the inverter switching frequency was selected to be 10 kHz. Any frequencies above the switching frequency could be neglect.

For the cable parameter of Table 2, the required number of sections given from equation (107) is N = 3.8 for a maximum frequency of 10 kHz. This means that 4 section are required to present the cable accurately up to the switching frequency as shown in Figure 54.

Since in the output of this system is inverter current, the main frequency of interest is the current frequency its harmonics. If the main frequency of the current was 60 Hz and up to the 13th harmonic was considered, the maximum frequency of interest would be 780 Hz. From equation (107), 1 section will be enough to model the cable at 780 Hz and below. In fact, 1 section model will represent the cable with good accuracy up to 2600 Hz.
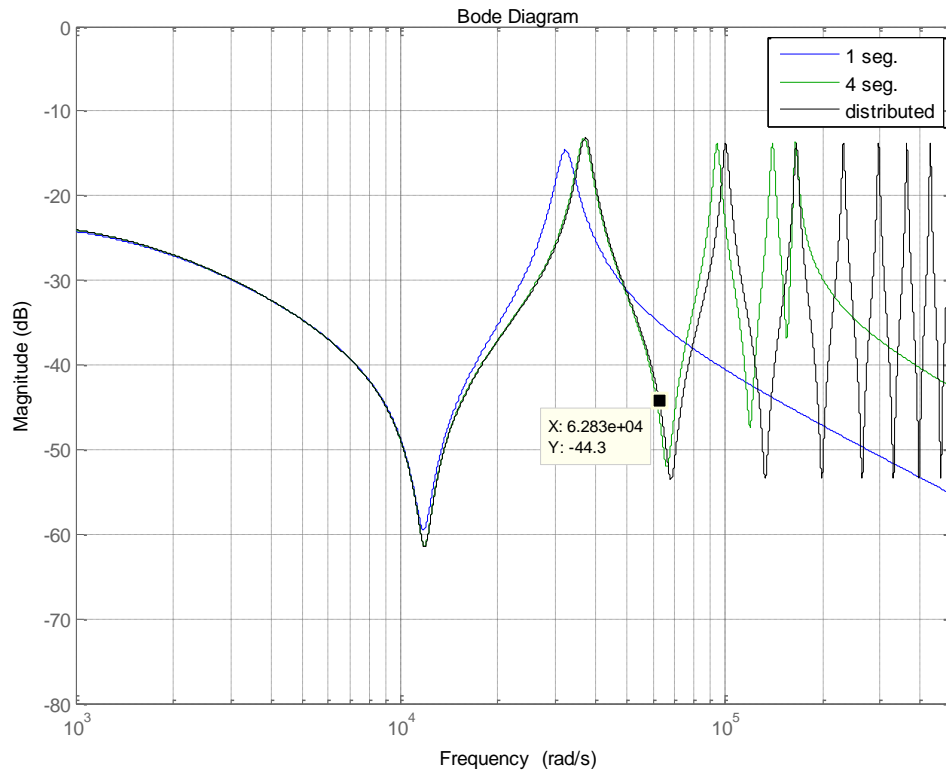
Figure 54 : Four Segments T-model.

Although, it is possible to implement the 3th order 1 section model in real time system to represent the cable up to the 13th harmonic, it always a good idea to increase the represented frequency range. In general, the sectioning method is not efficient in improving accuracy. In the next section, a modified 1-segment T model is presented which is more accurate than the original T model.

94

5.2.7 Modified T-model

The 41st order 20-segment model was reduced to a 3rd order model by eliminating the high frequency poles and zeros and adjusting the gain to account for the eliminated poles and zeros.

Figure 55 shows the responses of the distributed model, 1 and 20 segment model along with the reduced model. The reduced model is accurate enough at low frequencies. It shows an improved accuracy compared to the original 1 segment model.
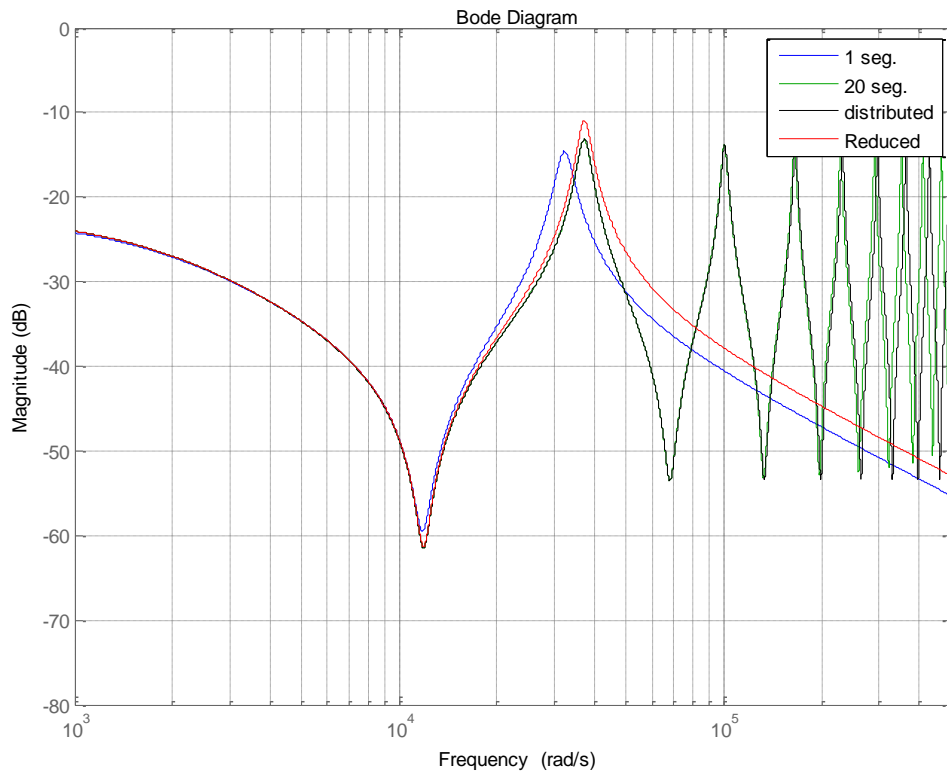
Figure 55 : Bode plot of the 1 segment, 20 segments, distributed and reduced models.

This reduced third order model cannot be presented with a T-model because there is no solution for R, L and C to represent the reduced model in T model form. For this reason, a modified T-model is proposed in order to emulate the cable in the lab environment.

A modified T model was developed. This model uses the same lumped values of cable resistance, inductance and capacitance. The only difference compared to the original T model is that the lumped capacitance is not placed in the middle. Instead, part of the lumped resistance and inductance is placed on the inverter side and the rest of the motor side as shown in Figure 56.
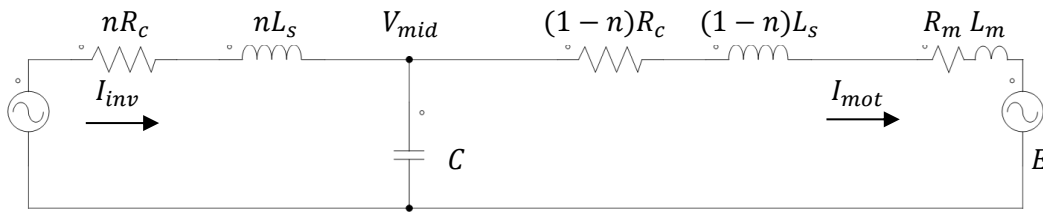
Figure 56 : Motor and cable per phase combined model of the modified T model.

Where n has a value from 0 to 1. If n = 0.5, this will result in the original T model presented previously. By comparing the poles and zeros from this model with the reduced model, a solution for n was derived to make the modified model as close as possible to the reduced model. A value of n = 0.37 was chosen to make the modified T model close enough to the original model. The Bode plot for the obtained model is shown in Figure 57.

5.2.8   *Simulation results*

The distributed model, 20 segment model, original and modified T models where simulated. The terminal load was the motor. An ideal inverter was used to apply a sinusoidal voltage with 0.8 modulation index using a 150V dc bus voltage. Figure 58 shows the resultant motor current, capacitor current and inverter current for these models. Figure 59 shows the simulation results for all models for a shorter time scale. Both the original and modified T models resulted in acceptable response compared to the distributed model at the frequency range of interest. Both models failed to show the extremely high frequency component in the currents. Since these high frequencies are not of interest in this study, the 1 segment T-model was considered acceptable representation of the cable.
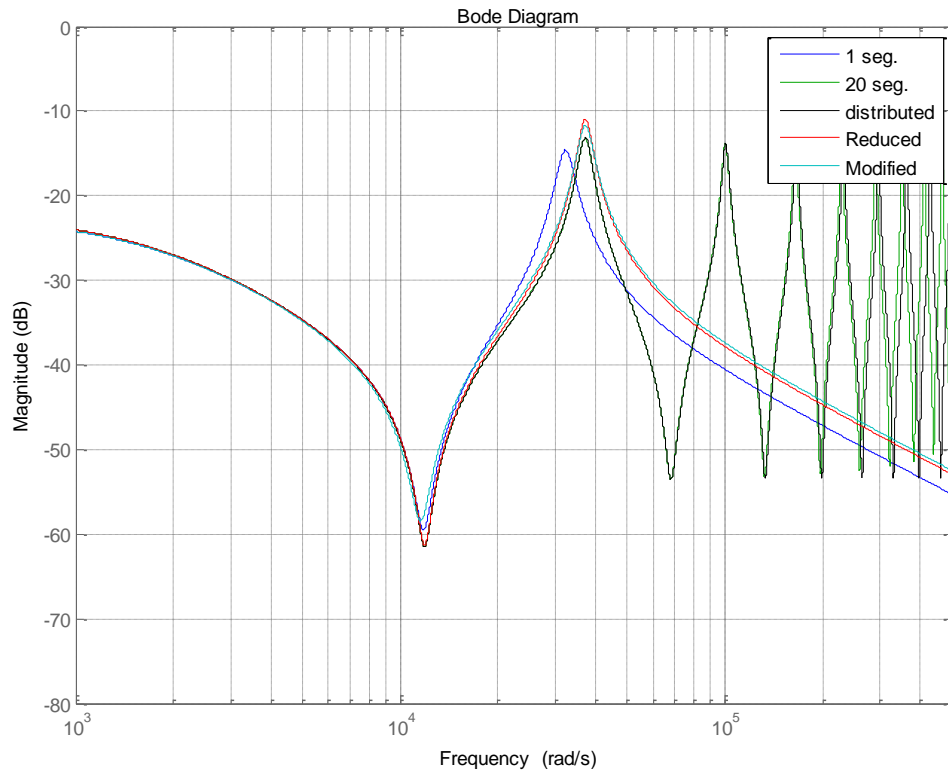
Figure 57 : Bode plot of previous models along with the modified T model.
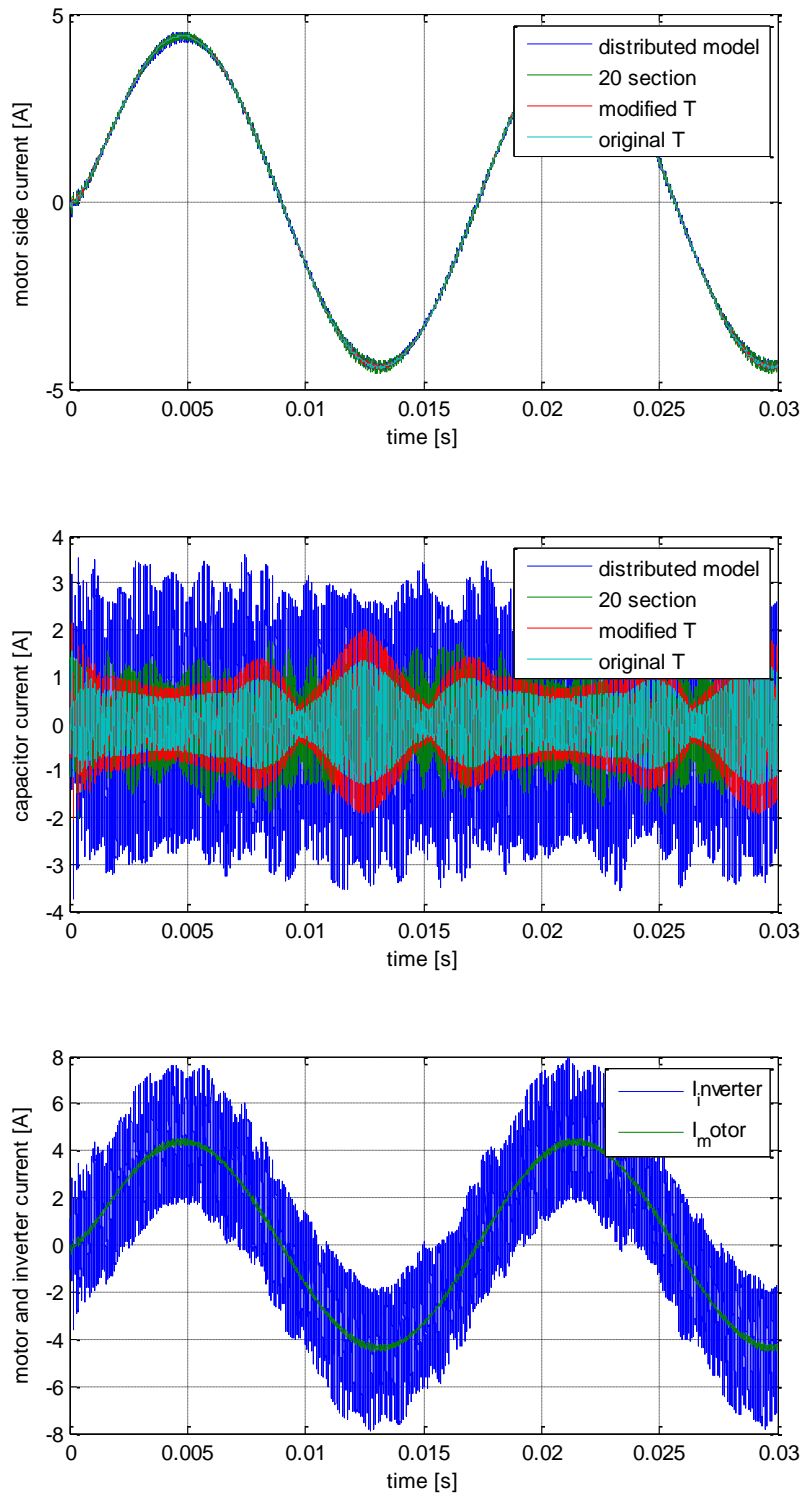
Figure 58 : Simulation results for all models.
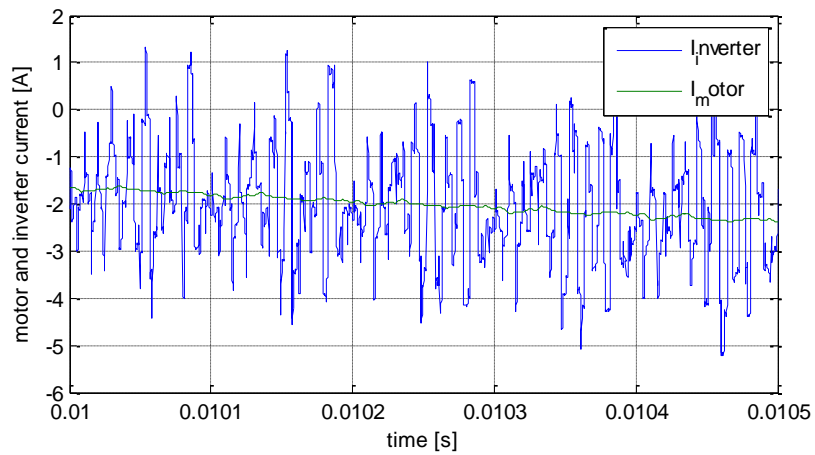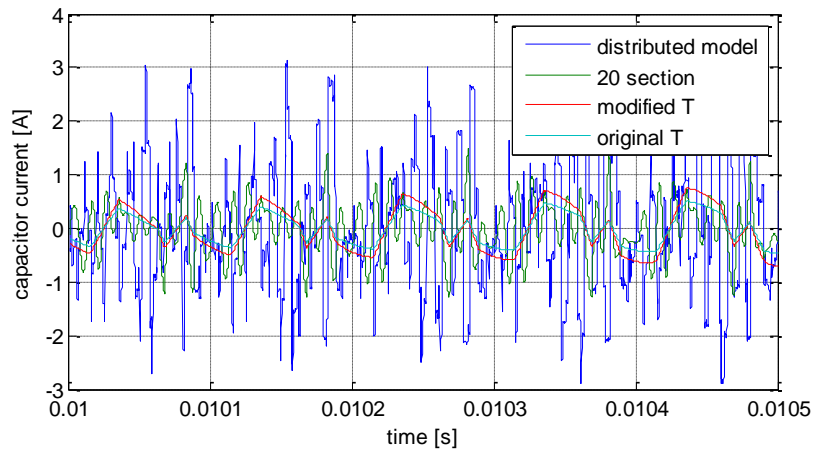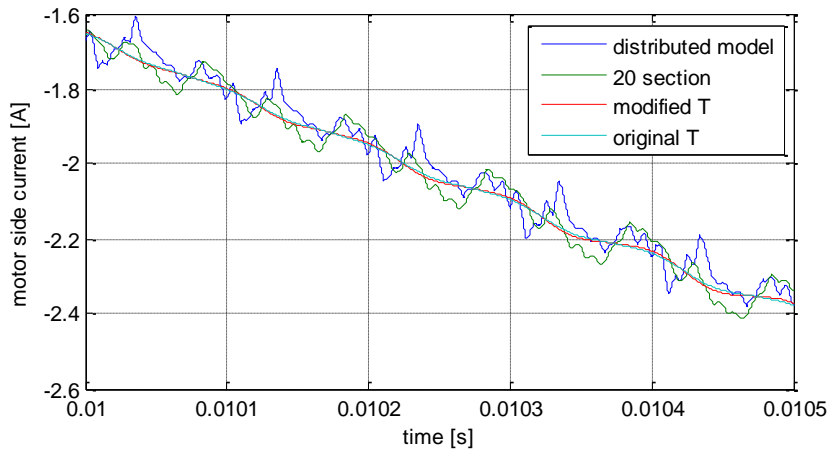
Figure 59 : Simulation results for all models.

5.3   Sensorless control with long cable (AC system)

5.3.1   System state space model

The three phase linear motor is modeled in the two axis stationary reference frame taking into account the motor resistance, inductance and back EMF. The whole system is shown in Figure 60.
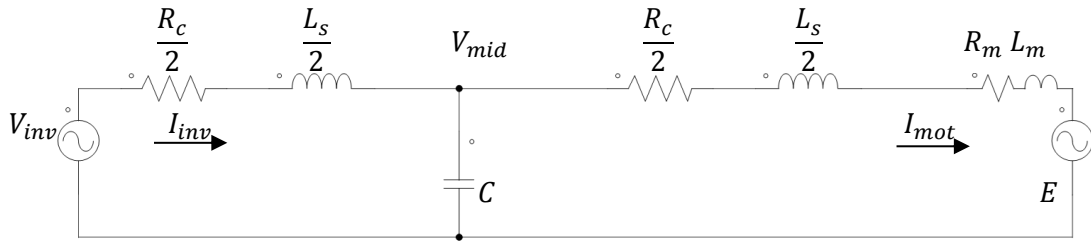
Figure 60 : Motor and cable per phase combined model of the original T model

The system state space model is of the form:

$$\frac{d}{dt}x = A\,x + B_1 u_1 + B_2 u_2$$

(109)

$$y = Cx$$

It could be derived as:

$$\frac{d}{dt}\begin{bmatrix} I_{inv} \\ I_{mot} \\ V_{mid} \end{bmatrix} = \begin{bmatrix} -\frac{R}{L} & 0 & -2/L \\ 0 & -\frac{R_m + \frac{R}{2}}{L_m + \frac{L}{2}} & \frac{1}{L_m + \frac{L}{2}} \\ \frac{1}{C} & -\frac{1}{C} & 0 \end{bmatrix} \begin{bmatrix} I_{inv} \\ I_{mot} \\ V_{mid} \end{bmatrix} + \begin{bmatrix} \frac{2}{L} \\ 0 \\ 0 \end{bmatrix} V_{inv} + \begin{bmatrix} 0 \\ -\frac{1}{L_m + \frac{L}{2}} \\ 0 \end{bmatrix} Emf$$

(110)

101

$$I_{inv} = \begin{bmatrix} 1 & 0 & 0 \end{bmatrix} \begin{bmatrix} I_{inv} \\ I_{mot} \\ V_M \end{bmatrix}$$

This model has one output which is the inverter side current and two outputs which are the inverter voltage and a back-EMF term. The back-EMF term could be modeled as an unknown input/disturbance.

5.3.2   Implementation and experimental results

A Luenberger observer could be used to estimate this input/disturbance by adding a feedback term. In discrete time this could be written as:

$$\hat{x}(k + 1) = A_d \hat{x}(k) + B_d u(k) + L\big(y(k) - C\hat{x}(k)\big)$$

where

$$A_d = e^{AT}$$

$$B_{1d} = A^{-1}(e^{AT} - I_n)B_1$$

$$B_{2d} = A^{-1}(e^{AT} - I_n)B_2$$

The rest of the system was implemented using the same approach used in the first section of this chapter. The error between the measured and estimated inverter current is fed to a PI compensator to estimate the back EMF. This is done in the two axis stationery reference frame. Next a PLL observer is used to estimate the motor position from the back EMFs. The same experimental setup explained in in section 5.1   was used to implement the sensorless algorithm with a T-model of the cable added between the inverter and the motor.

A hardware setup was built to emulate the T model. Wire wound resistors and castor oil capacitors were used to represent the cable resistance and capacitance. Inductors were built using toroid powder core and magnet wire to represent the cable inductance. The inductor was designed using the following equation:

$$L = \frac{\mu N^2 h}{2\pi} ln\left(\frac{b}{a}\right) \tag{111}$$

where b and a are the outer and inner radii of the core respectively and h is the core height. N is the number of turns and μ is the permeability of the core.

Figure 61 shows the experimental results which compare the position and speed obtained from the encoder to those obtained from the sensorless algorithm. Again there is mismatch between the results especially at end of one cycle and begging of another. This mainly because of the low or zero back EMF in that region.
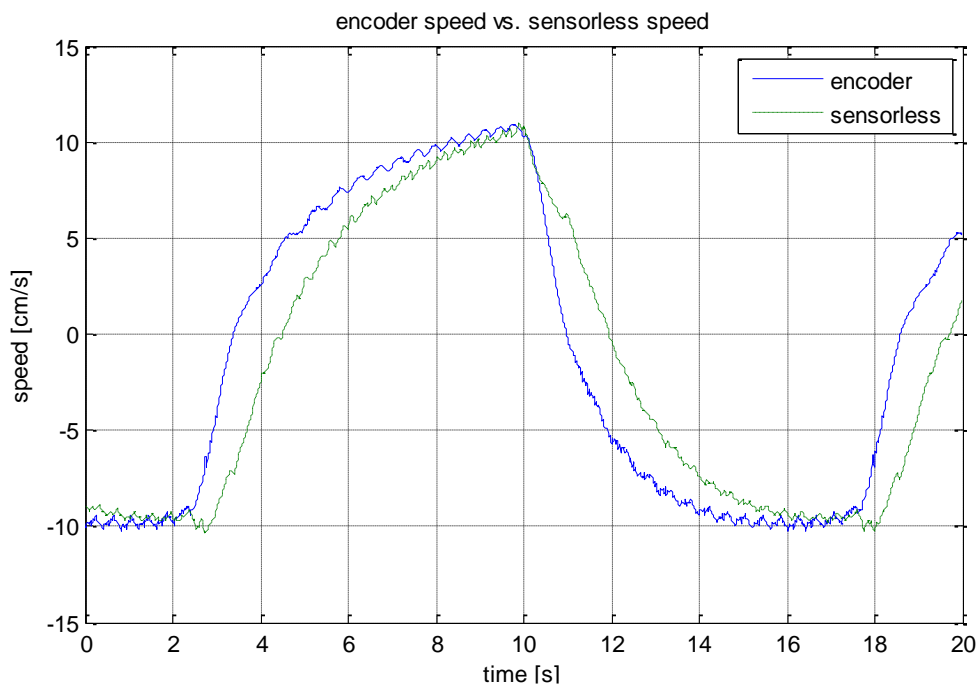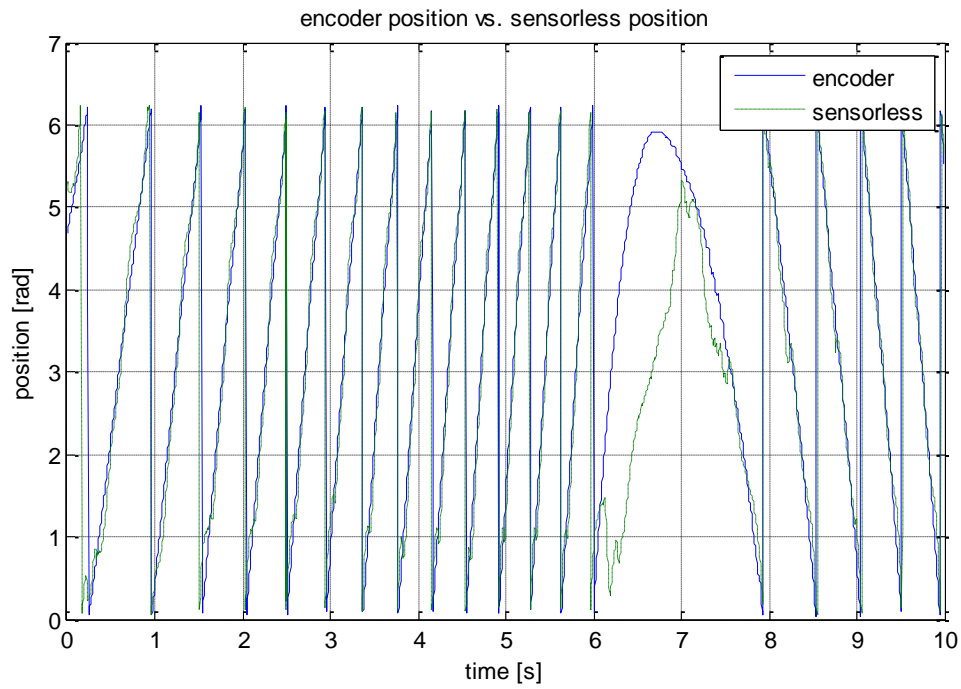
Figure 61 : Experimental results of the linear motor sensorless control with a long cable.

104

CHAPTER VI

PUMP MONITORING SYSTEM

The reciprocating pump is required to run reliably at optimal conditions. Any fault may result in several days of shut down time which is a huge loss in production. Moreover, a pump functioning in under-optimal operating condition is resulting in production loss too. It is important to monitor the pump condition to determine any fault condition. To monitor a pump operation, ideally the following parameters could be measured:

1. Pump suction pressure

2. Pump discharge pressure

3. Fluid flow

4. Pump speed

5. Pump load force

Unfortunately it is not practical to install all these sensors. In most cases, it is not economically justifiable to install any downhole sensor. In real life applications, most sucker rod pumps run with only a flow meter while some include other surface sensors.

6.1   Dynamometer cards

In sucker rod pumping systems, a force and position sensor may be placed on the surface polished rod. The force is measured using a clamp or horseshoe load cell transducer. A string potentiometer transducer or an accelerometer may be used to measure the position. Alternatively, an inclinometer attached to the beam may be employed to

obtain the position information. The force and position sensors are connected to a dynamometer which analyze the data. The dynamometer generates a plot of the load force vs. the position. This plot of load force vs position of the polished rod known as the surface dynamometer card is suited for pump monitoring of shallow wells.

Because of the elastic nature of the sucker rod, the downhole pump force and position are different from the polished rod measurement obtained on the surface. The dynamometer may be used to estimate the pump force and position using the Wave Equation which is a mathematical model that accounts for the elastic nature of the sucker rod. This plot of downhole pump load force vs position is known as downhole dynamometer card. Figure 62 shows an example of a surface and downhole dynamometer cards [38].

Surface Dynamometer Card

LOAD (LBS.)

18,000
14,000
12,000
10,000
8,000
6,000
4,000
2,000
0
-2,000

Surface stroke : 64"

Pump Dynagraph Card

Tubing stretch : 16"

Net stroke : 20"

7400' Well
7/8", 3/4", 5/8" Rod string
11/2" Pump
Unanchored tubing
9 Spm., 64" Surface stroke

Pump displacement : 0.262 x 20 x 9 : 47 b/pd
Production : 34 bopd
Efficiency : 72%

DISPLACEMENT (Ft.)

0   1   2   3   4   5   6   7   8
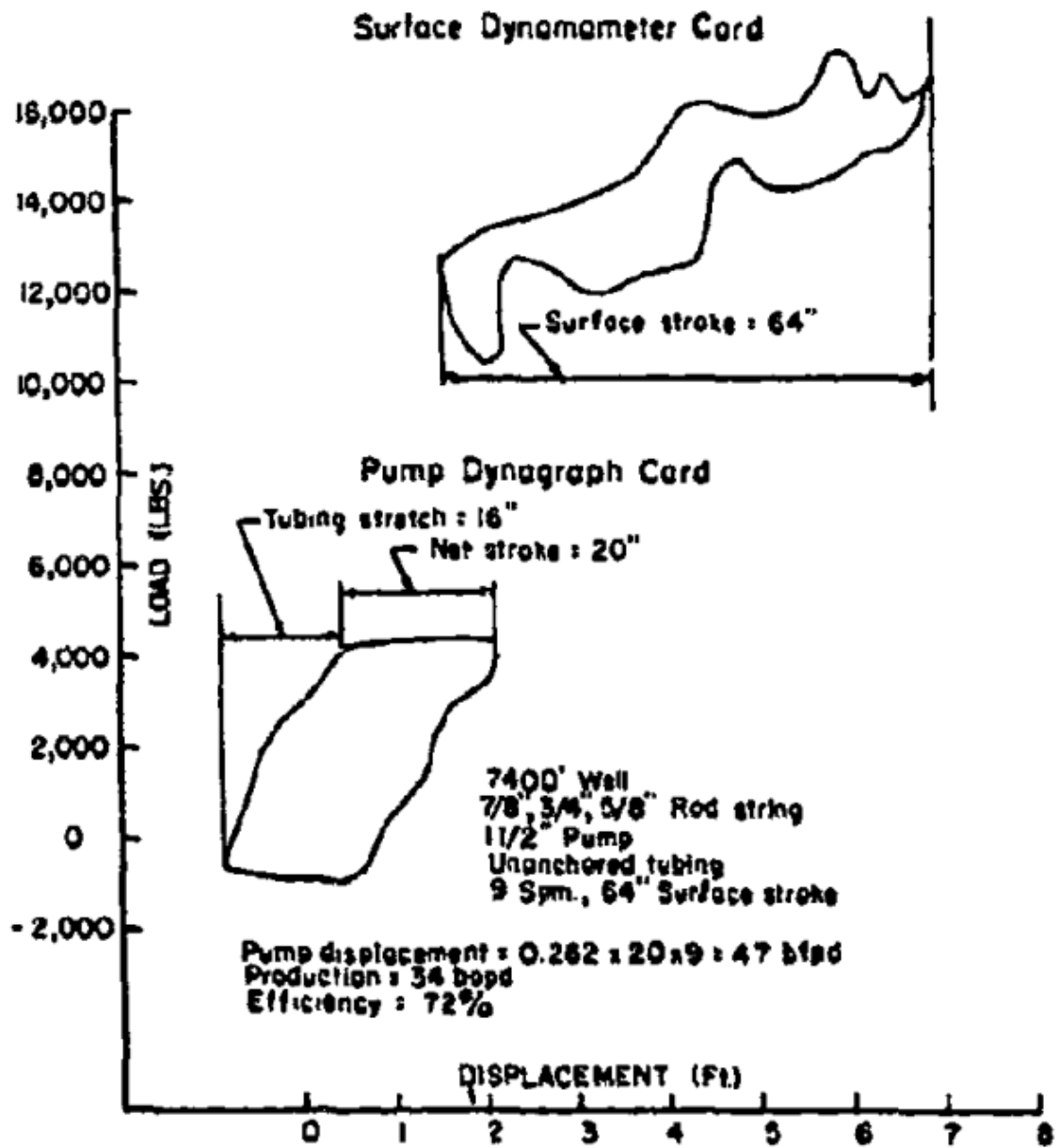
Figure 62 : Surface and downhole dynamometer card [38].

6.2 Interpretation of dynamometer cards

Different pump fault condition will result in different dynamometer cards. Therefore, the downhole force and position dynamometer card could be used as a signature to monitor the pump condition. The normal pump operating condition results in a rectangular card. Figure 63 shows the force and position relation under various fault conditions.
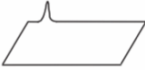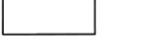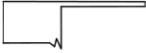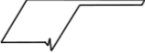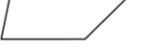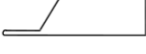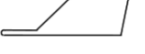
Anchored Tubing	Description	Unanchored Tubing
	Ideal card Pump properly functioning completely filled with liquid.	
	Full pump with unaccounted friction Extra friction along the rod string is not removed by the wave equation used to calculate the pump card.	
	Plunger tagging Plunger hits up or down because of improper spacing of the pump.	
	Tubing anchor slipping Malfunctioning tubing anchor allows tubing to stretch.	
	Bent or sticking barrel Load increases on upstroke, decreases on downstroke in defective section of barrel.	
	Worn or split barrel Rod load decreases in defective section of the barrel.	
	Sticking plunger Load spike shows where plunger stopped; extra load is needed to overcome friction in the pump at this position.	
	Slight fluid pound Fluid level falling to pump intake.	
	Severe fluid pound Barrel incompletely filling with liquid due to limited well inflow.	
	Well pumped off Pump displacement much greater than well inflow. PIP, pump fillage are low.	
	Gas interference Mixture of liquid/gas fills barrel. PIP is high, pump fillage is low. Unstable operation.	
	Gas-locked pump Barrel filled with gas, valves remain closed, no liquid production. Low PIP.	
	Choked pump Intake plugged, barrel incompletely fills during upstroke. PIP is high, pump fillage is low.	
	Leaking TV or pump TV leak or pump slippage causes delay in picking up and premature unloading of fluid load.	
	Badly leaking TV or pump TV or plunger/barrel completely worn out.	
	Leaking SV Premature loading at start of upstroke and delayed unloading at start of downstroke.	
	Badly leaking SV SV completely worn out.	
	Worn-out pump TV & SV valves and barrel/plunger completely worn out.	
	Delayed closing of TV TV ball does not seat as soon as upstroke starts.	
	Hole in barrel or plunger pulling out of barrel Load drops as plunger reaches hole or pulls out.	

Figure 63 : Effects of common pump faults on force and position [16].

109

6.3   Linear motor dynamometer cards

In the case where the linear motor is connected directly to the pump downhole, the load force could be estimated from the motor current and speed information. The equation of motion for the pump could be written as:

$$m\frac{d^2}{dt^2}x + b\frac{d}{dt}x = F_{em} - F_{load} \tag{112}$$

where m is the mass of the moving parts of the motor and pump and b is the damping coefficient. F_{em} is the electromagnetic force applied by the motor and F_{load} is the load force caused by the weight of the lifted fluid. Equation (112) could be rewritten as:

$$m\frac{d}{dt}v + bv = F_{em} - F_{load} \tag{113}$$

where v is the velocity. In the s-domain it could be represented as:

$$v = \frac{1}{m\,s + b}\,(F_{em} - F_{load}) \tag{114}$$

Equation (114) represent a first order system with two inputs which are the forces F_{em} and F_{load} and one output which is the linear speed v. The output and one of the input are known.

Here it is assumed that m and b are known and v could be measured or estimated from the sensorless algorithm. The electromagnetic force F_{em} could be calculated from the motor current as:

$$F_{em} = \frac{3}{2}\frac{\pi}{\tau_p}(\lambda_{pm}\,i_q + (L_d - L_q)\,i_d\,i_q) \tag{115}$$

110

An observer is used to estimate the other input namely F_{load}. A Luenberger observer is constructed in the same way as the back EMF observer. Figure 64 shows the block diagram of the observer.
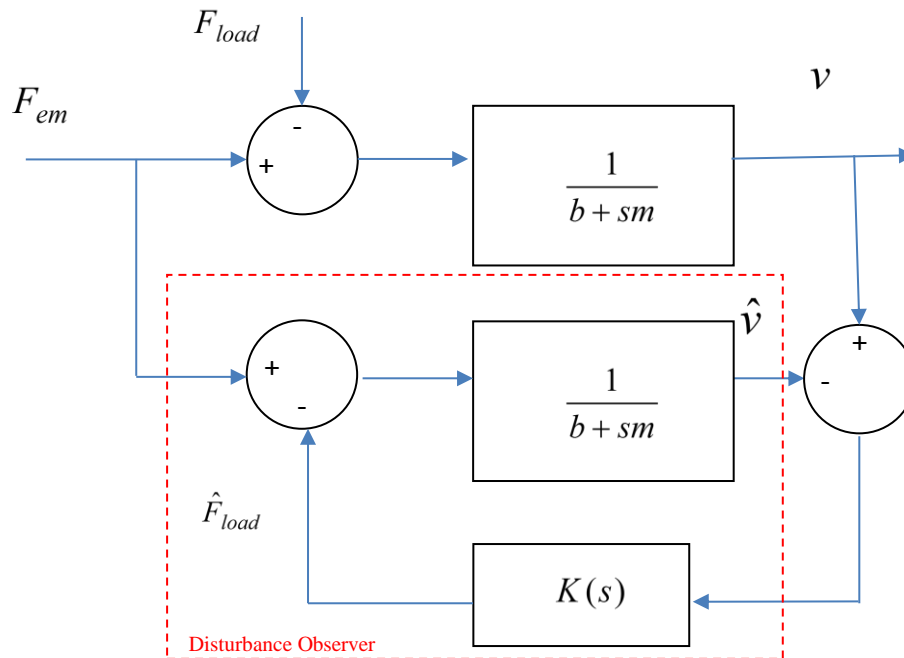
Figure 64 : Block diagram of the load force observer.

First, the speed is estimated from the calculated electromagnetic force and the estimated load force using the first order model. Then, a compensation signal is generated using a PI compensator based on the error between the estimated speed and measured speed. This compensated signal will be the other input to the system.

6.4   Experimental results

Figure 65 compares the load force estimated from this observer to the measured load force measured using a load cell connected to the experimental setup.
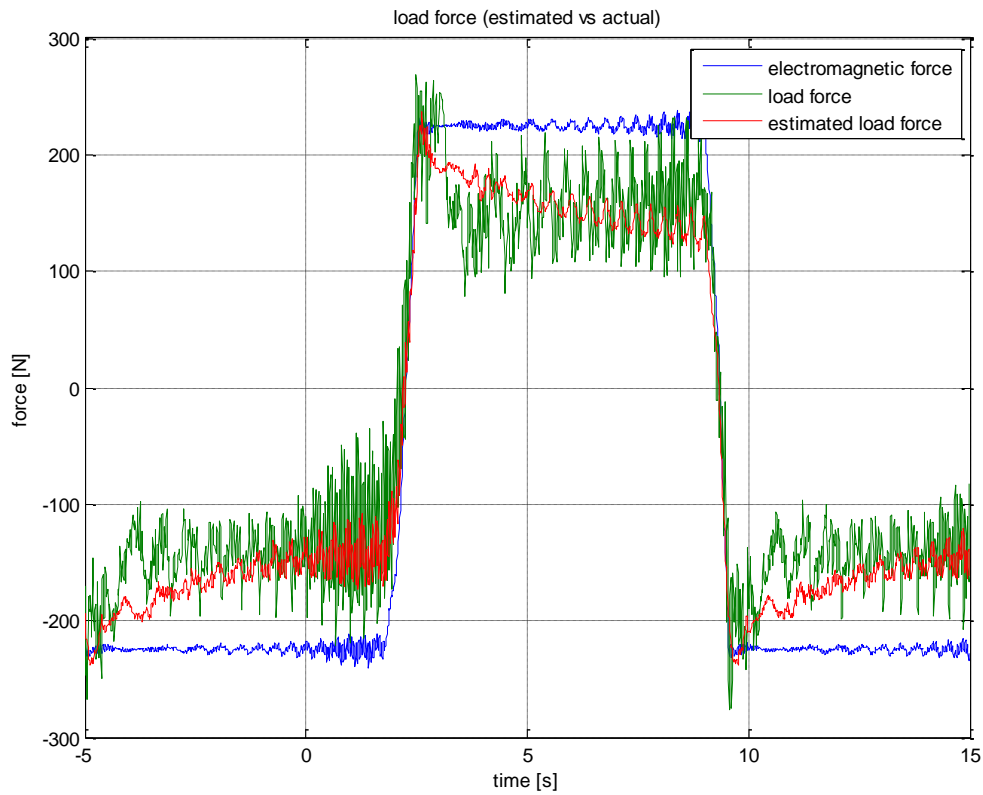
Figure 65 : Measured load force vs. estimated load force.

Figure 66 shows a pump dynamometer card for the experimental setup discussed previously. The load in the experimental setup was obtained using a rotating generator

connected through a magnetic screw as shown previously in Figure 36. Even with the generator controlled in vector control, this system is not a perfect representation of a reciprocating pump mainly because of the viscous friction in the rotating bearing.
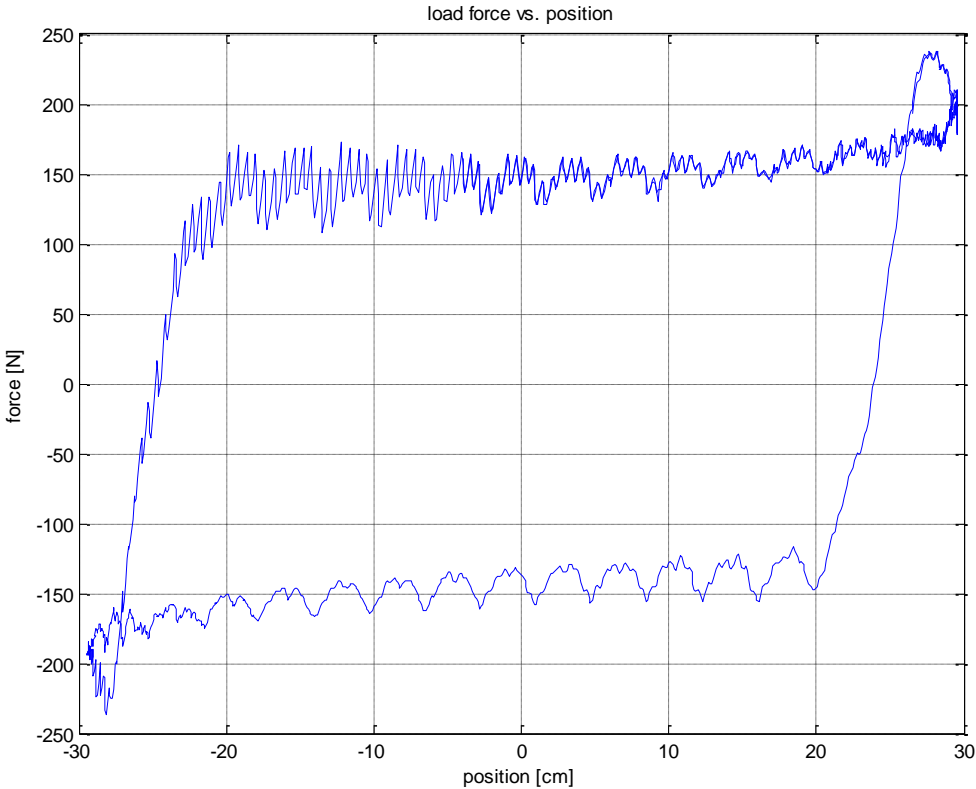
Figure 66 : Pump dynamometer card showing the estimated load force vs. pump position.

Finally, the pump could be monitored by comparing the obtained pump dynamometer card to the ideal card. Any discrepancy could be used to identify the fault conditions as shown in previously in Figure 63.

To test this fault monitoring system, the load was change on the generator to emulate some of the pump fault conditions. Figure 67 shows the dynamometer card for a gas locked pump. Figure 68 show the dynamometer card for a pump with sticking plunger. The case of worn barrel is shown in Figure 69.

These figures shows that the fault monitoring system was able to detect the change in the position and load force relationship. Based on the dynamometer card, any pump fault could be identified.

Figure 67 : Pump dynamometer card for gas locked pump.

Figure 68 : Pump dynamometer card for sticking plunger.
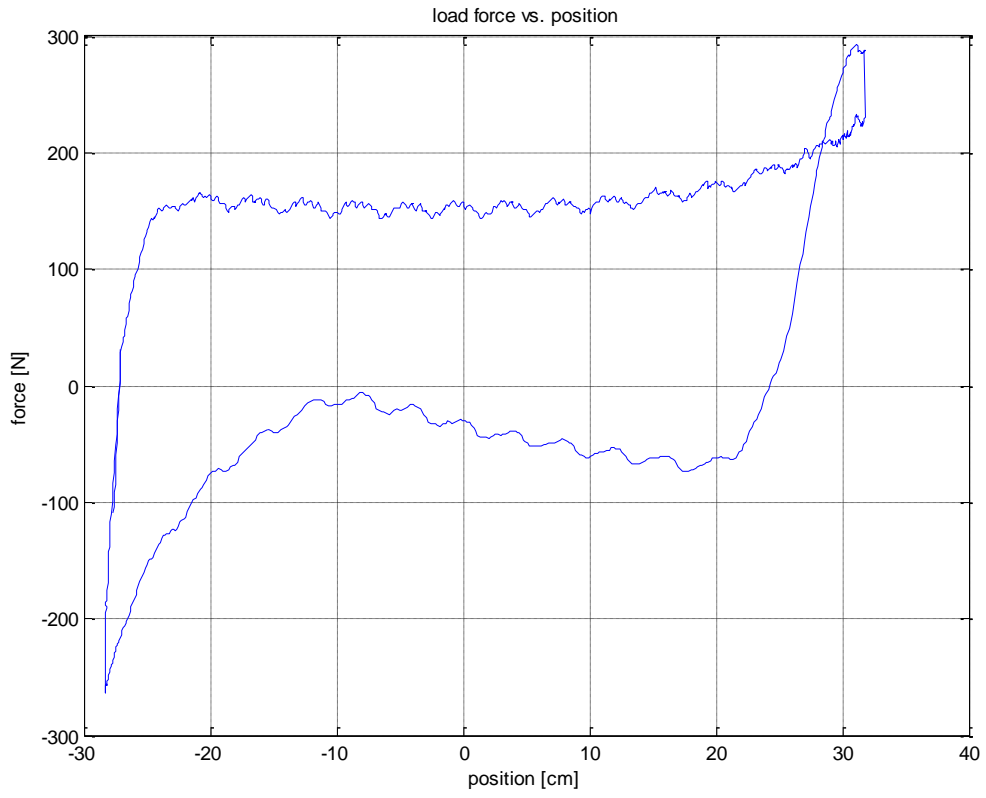
Figure 69 : Pump dynamometer card for worn barrel.

CHAPTER VII

CONCLUSIONS

In this dissertation, the surface unit of the sucker rod pumping system was replaced with a permanent magnet linear motor which drives the reciprocating pump directly. The main advantages of the new system is the higher reliability and the ability to be used in deviated wells.

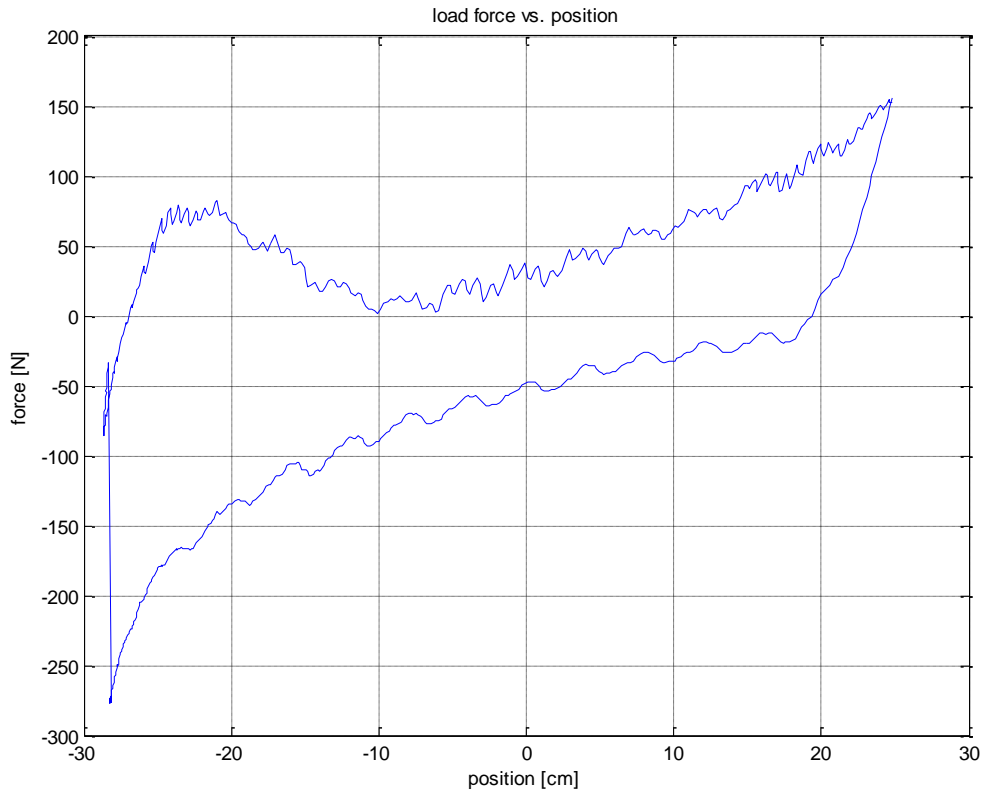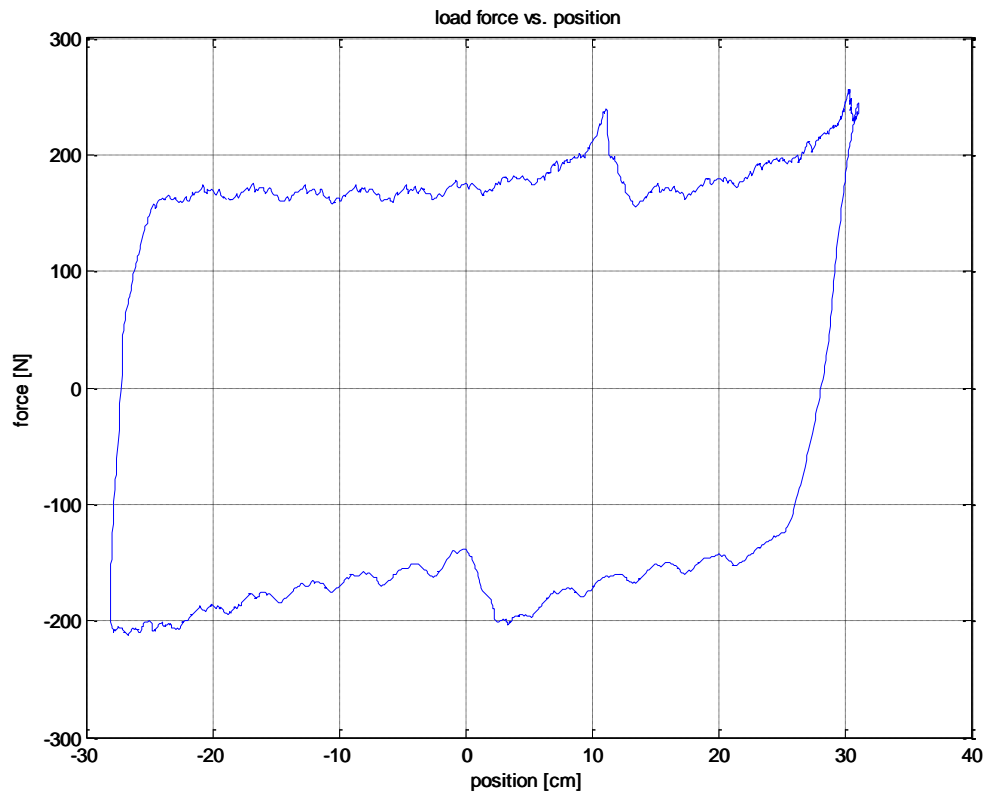Two different systems where proposed. In the AC system, the motor drive is placed on the surface and connected to the motor through a long cable. The motor is placed downhole to drive the reciprocating pump. The DC system replaces the AC cable with DC cable. In this system the inverter is integrated with the motor downhole while the rectifier remains on the surface. A modified integrated motor drive with its speed control algorithm is suggested.

Next, two sensorless algorithm are developed for both the AC and DC systems. The AC system sensorless algorithm utilizes the motor and cable models to estimate the motor position and current.

The DC system results in better efficiency and performance. This is mainly because the DC cable shows only resistance with no skin effect, inductance or capacitance. Moreover, the sensorless algorithm for the DC system was much simpler because of the proximity of the inverter and motor. On the other hand, the DC system require a high temperature inverter such as SiC which is more expensive compared to IGBT.

Finally, a pump monitoring system is developed to detect the common pump faults. The system monitors the load force vs. motor position graph. To obtain the load force, a Luenberger observer was developed. The motor position could be obtained using position sensors or using the sensorless algorithms presented previously. The load force vs. motor position graph could be used to identify various fault signatures.

REFERENCES

[1]   U.S. Energy Information Administration, "Monthly Energy Review". March 2015.

[2]   R. K. O'Neil, "Application and selection of electric submergible pumps," presented at the Rocky Mountain Region Annual Meeting, AIME-SPE, SPE 5907, Casper, WY, May 1975.

[3]   G. Skibinski, S. Breit, "Line and load friendly drive solutions for long length cable applications in electrical submersible pump applications," in Petroleum and Chemical Industry Technical Conference, pp. 269-278, 2004.

[4]   D. N. Alcock, "The Equipment for and Economics of Variable-Flow Well Pumping," IEEE Transactions on Industry Applications, vol. IA-16, no. 1, pp. 144-153, Jan. 1980.

[5]   X. Liang, E. Fleming, "Electrical Submersible Pump Systems: Evaluating Their Power Consumption," IEEE Industry Applications Magazine, vol. 19, no. 6, pp. 46-55, Nov 2013.

[6]   J. F. Gieras, Z.J. Piech and B.Z. Tomczuk, Linear Synchronous Motors: Transportation and Automation Systems. Boca Raton, FL: CRC, 2012.

[7]   I. Boldea, Linear Electric Machines, Drives, and MAGLEVs Handbook. Boca Raton, FL: CRC, 2013.

[8]   H. A. Hussain and H. A. Toliyat, "Field Oriented Control of tubular PM Linear Motor using linear Hall Effect sensors," 2016 International Symposium on Power

Electronics, Electrical Drives, Automation and Motion (SPEEDAM), pp. 1244-1248, 2016. © 2016 IEEE.

[9] A. Mohammadpour, and L. Parsa, "SVM-based direct thrust control of permanent magnet linear synchronous motor with reduced force ripple," Industrial Electronics (ISIE), 2011 IEEE International Symposium on, pp. 756-760, 27-30 June 2011.

[10] M. A. M. Cheema, J. Fletcher, M.F. Rahman, and D. Xiao, "Modified direct thrust control of linear permanent magnet motors with sensorless speed estimation," 38th Annual Conference on IEEE Industrial Electronics Society (IECON 2012), pp. 1908-1914, Oct 2012.

[11] B-G. Gu and K. Nam, "A vector control scheme for a PM linear synchronous motor in extended region," in IEEE Transactions on Industry Applications, vol. 39, no. 5, pp. 1280-1286, Sept.-Oct. 2003.

[12] M.A.M. Cheema, J.E. Fletcher, D. Xiao, and F. Rahman, "Sensorless control of linear permanent magnet synchronous motors using a combined sliding mode adaptive observer," Energy Conversion Congress and Exposition (ECCE), 2014 IEEE, pp. 4491-4498, 14-18 Sept. 2014.

[13] T. J. E. Miller, "Brushless Permanent-Magnet and Reluctance Motor Drives", Oxford Science Publications, 1989.

[14] J. D. Clegg, S. M. Bucaram and N. M. Hein Jr., "Recommendations and Comparisons for Selecting Artificial-Lift Methods." Journal of Petroleum Technology, pp. 1128– 67, Dec 1993.

[15] B. M. Wilamowski and O. Kaynak, "Oil well diagnosis by sensing terminal characteristics of the induction motor," in IEEE Transactions on Industrial Electronics, vol. 47, no. 5, pp. 1100-1107, Oct 2000.

[16] G. Takacs, "Sucker-Rod Pumping Handbook: Production Engineering Fundamentals and Long-Stroke Rod Pumping". Oxford, US: Gulf Professional Publishing, 2015.

[17] F. W. Gipson and H. W. Swaim, "The Beam Pumping Design Chain", 1988 Southwestern Petroleum Short Course, Lubbock, Texas, Apr 1988.

[18] R. H. Gault, "Designing a Sucker-Rod Pumping System for Maximum Efficiency," SPE Production Engineering, pp. 284-90, November 1987.

[19] M. M. Rahman and L. R. Heinze, "Development of ALEOC Beam Pumping Failure Data Base", 2000 Southwestern Petroleum Short Course, Lubbock, Texas, Apr 2000.

[20] C. Kittel, Introduction to Solid State Physics. Hoboken, NJ: Wiley, 2005.

[21] Y. Yang, J. Yang, J. Han, C. Wang, S. Liu and H. Du, "Research and Development of Interstitial Compounds," in IEEE Transactions on Magnetics, vol. 51, no. 11, pp. 1-6, Nov 2015.

[22] F. Caricchi, F. G. Capponi, F. Crescimbini and L. Solero, "Sinusoidal brushless drive with low-cost linear Hall effect position sensors," 2001 IEEE 32nd Annual Power Electronics Specialists Conference, vol. 2, pp. 799-804, 2001.

[23] S-Y Jung, and K. Nam, "PMSM Control Based on Edge-Field Hall Sensor Signals Through ANF-PLL Processing," Industrial Electronics, IEEE Transactions on, vol. 58, no. 11, pp. 5121-5129, Nov 2011.

[24] S. Morimoto, K. Kawamoto, M. Sanada, and Y. Takeda, "Sensorless control strategy for salient-pole PMSM based on extended EMF in rotating reference frame," Industry Applications, IEEE Transactions on , vol. 38, no. 4, pp. 1054-1061, Jul/Aug 2002.

[25] S. Pakdelian, N. W. Frank and H. A. Toliyat, "Magnetic Design Aspects of the Trans-Rotary Magnetic Gear," in IEEE Transactions on Energy Conversion, vol. 30, no. 1, pp. 41-50, Mar 2015.

[26] P. W. Wheeler, J.C. Clare, M. Apap, D. Lampard, S. Pickering, K.J. Bradley, L. Empringham, "An Integrated 30kW Matrix Converter based Induction Motor Drive," in Power Electronics Specialists Conference, pp. 2390-2395, 2005.

[27] S. Pickering, F. Thovex, P. Wheeler, K. Bradley, "Thermal Design of an Integrated Motor Drive," in IEEE Industrial Electronics Conference (IECON), pp. 4794-4799, 2006.

[28] T. R. Brinner, R.H. McCoy, T. Kopecky "Induction Versus Permanent-Magnet Motors for Electric Submersible Pump Field and Laboratory Comparisons," IEEE Transactions on Industry Applications, vol. 50, no. 1, pp. 174-181, Jan 2014.

[29] R. Pragale, D.D. Shipp, "Investigation of premature ESP failures and oil field harmonic analysis," in Petroleum and Chemical Industry Technical Conference, pp. 1-8, 2012.

[30] J. M. Hornberger, E. Cilio, B. McPherson. R.M. Schupbach, A.B. Lostetter "A Fully Integrated 300°C, 4 kW, 3-Phase, SiC Motor Drive Module," in Power Electronics Specialists Conference, pp. 1048-1053, 2007.

[31] T. R. Brinner, "Voltage and Cable Impedance Unbalance in Submergible Oil Well Pumps," in IEEE Transactions on Industry Applications, vol. IA-20, no. 1, pp. 97-104, Jan. 1984.

[32] H. A. Hussain and H. A. Toliyat, "Back-EMF based sensorless vector control of tubular PM linear motors," IEEE International Electric Machines & Drives Conference (IEMDC), pp. 878-883, 2015. © 2015 IEEE.

[33] J. Maes and J. A. Melkebeek, "Speed-sensorless direct torque control of induction motors using an adaptive flux observer," in IEEE Transactions on Industry Applications, vol. 36, no. 3, pp. 778-785, May/Jun 2000.

[34] D. Koenig and S. Mammar, "Design of proportional-integral observer for unknown input descriptor systems," in IEEE Transactions on Automatic Control, vol. 47, no. 12, pp. 2057-2062, Dec 2002.

[35] H. Kim, M. C. Harke and R. D. Lorenz, "Sensorless control of interior permanent-magnet machine drives with zero-phase lag position estimation," in IEEE Transactions on Industry Applications, vol. 39, no. 6, pp. 1726-1733, Nov/Dec 2003.

[36] Y. Inoue, K. Yamada, S. Morimoto and M. Sanada, "Effectiveness of Voltage Error Compensation and Parameter Identification for Model-Based Sensorless Control of IPMSM," in IEEE Transactions on Industry Applications, vol. 45, no. 1, pp. 213-221, Jan/Feb 2009.

[37] J. R. Smith and W. W. Bell, "Selection of transmission circuit models for power-system transient studies," in IEE Proceedings C - Generation, Transmission and Distribution, vol. 131, no. 1, pp. 1-4, Jan 1984.

[38] J. R. Eickmeier, "Diagnostic Analysis of Dynamometer Cards". Journal of Petroleum Technology, vol. 19, no. 01, pp. 97-106, Jan 1967.